The Dissertation Committee for Adrian Kristopher Fontanilla
certifies that this is the approved version of the following dissertation:

Tokamak Disruptions: Investigations of Symptoms and Treatments

Committee:

Boris N. Breizman, Supervisor

Richard D. Hazeltine

Philip J. Morrison

Kenneth W. Gentle

Laxminarayan L. Raja

Tokamak Disruptions: Investigations of Symptoms and Treatments

by

Adrian Kristopher Fontanilla

DISSERTATION
Presented to the Faculty of the Graduate School of
The University of Texas at Austin
in Partial Fulfillment
of the Requirements
for the Degree of

DOCTOR OF PHILOSOPHY

THE UNIVERSITY OF TEXAS AT AUSTIN
August 2019

Dedicated to Taylor and Disco Sally Ride.

Acknowledgments

I would like to acknowledge all the professors of the Institute of Fusion Studies who contributed to my learning, and in particular, Professor Boris N. Breizman. Without his patient and adept tutelage, the means by which I inspect the physical world would remain clumsy.

Tokamak Disruptions: Investigations of Symptoms and Treatments

Publication No. __________________

Adrian Kristopher Fontanilla, Ph.D.
The University of Texas at Austin, 2019

Supervisor: Boris N. Breizman

Plasma disruptions are a catastrophic loss of confinement that ultimately concludes with the release of the thermal and magnetic energy stored in the vessel containing the plasma. The threat of disruptions therefore factor into the development of fusion-grade tokamak reactors such as ITER. This work discusses the deleterious effects of disruption, particularly runaway electrons. Tokamaks are especially susceptible to runaway electrons because of their highly inductive nature. The lifetime of seed runaways are calculated and the likelihood for them to exponentiate is discussed. Strategies for alleviating the danger posed by disruptions are considered. The basic strategy, assuming a disruption is imminent, is to preemptively cool the plasma. ITER currently plans on deploying impurity pellets to safely radiate away the energy, so investigations of pellet heating and ablation are conducted.

Table of Contents

List of Figures

Chapter 1

Introduction

1.1 Fusion

Almost as soon as scientists ascertained the feasibility of the huge energies possible with fission, i.e. the splitting of heavy atoms, they were pondering whether or not fusion of light atoms could be achieved, as well. History (Trinity, First Lightning) has record of the pace at which we, as a species, were able to harness nuclear energies for destructive purposes. The grand ambition of producing fusion for sustained energy which would power our cities, however, remains elusive.

Despite the challenges, there are a number of reasons why we should continue the pursuit. Our main source of producing electricity comes from the burning of fossil-fuels, but estimates by[1] indicate that the global supply will be expended at a time scale on the order of one-hundred years. On the other hand, the principal reactions for controlled nuclear fusion are

$$D + D \rightarrow {}^{3}He + n + 3.2\,MeV \tag{1.1}$$

$$D + D \rightarrow T + p + 4.0\,MeV \tag{1.2}$$

$$D + T \rightarrow {}^{4}He + n + 17.6\,MeV \tag{1.3}$$

which includes deuterium (D) that can be mined from ocean water. Moreover, nuclear reactions produce about a million times more energy than a typical chemical reaction which releases energies on the order of $1\,eV$. The most pressing issue, however, may be the impact that the burning of fossil-fuels has taken on the planet, i.e. climate change. In comparison with fossil-fuels, fusion energy will have a very low carbon footprint.

1.2 Tokamak

The nuclear reactions listed above have very low cross-sections, in general, and the gases must be heated to about $10\,keV$ in order to produce a notable yield. Steady-state fusion is achieved in stars by the compression of stellar gas by intense gravitational forces; this compression both heats and confines the gas. Fusion is done differently on earth, but we have yet to achieve the steady-state required for commercial power. The primary effort to achieve practical controlled-fusion terrestrially is the tokamak and is the point-of-interest for this work. Tokamaks employ coils (see Fig. 1.1) to magnetically confine the plasma inside a torus and heats the plasma via external sources (e.g. radio-frequency heating, neutral-beam injection). The guiding principle of the tokamak confinement strategy is to wind the particle trajectories about the toroidal field using poloidal fields. This circumvents the issue of particle drift to the vessel wall caused by gradients in the toroidal field. The poloidal field is generated by the transformer coil in the center of the torus and a toroidal (ring) current in the plasma. A consequence of this design is that fusion-grade tokamaks, which carry currents on the order of $10^6\,A$, are hugely inductive. This makes the tokamak especially susceptible to runaway electrons.

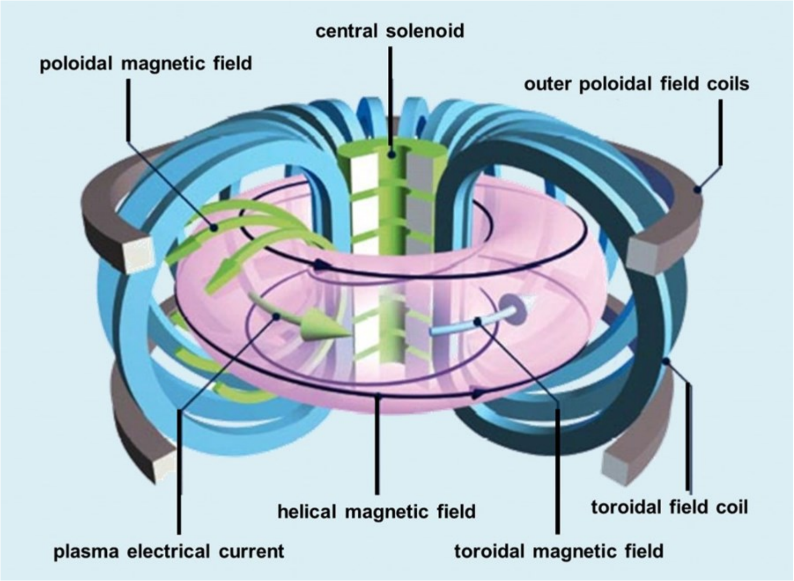

Figure 1.1: Schematic of tokamak. *Source*: EFDA-JET (now EUROfusion).

The next-generation tokamak is ITER which is, at the time of writing, currently undergoing construction in the south of France. It will be a culmination of engineering and physics developed over the last sixty years. Even so, it is still a proof-of-concept of whether or not a net gain of energy can be achieved from the tokamak design. ITER will burn plasma at a scale far beyond that realized at any of our current machines. For that reason, it is difficult to extrapolate empirical data to anticipate performance at ITER. Moreover, as in the case of disruptions, it is dangerous to design an experiment to probe destructive scenarios. Therefore, many predictions must be obtained from theoretical and computational research.

1.3 Scope

This work contains descriptions of a fusion plasma that are relevant to the problem of disruption, which is described in the next chapter. In particular, we discuss runaway electrons, which are a symptom of disruption, and pellet ablation, which is related to the treatment of disruption. Common to each of these aspects is a time scale which is faster than the relaxation time of the background plasma. Hence, there is a population of plasma particles which are non-thermal, i.e. they cannot be described by a Maxwellian distribution nor can their motion be described by (Euler) fluid equations. In the case of runaways, the fast time scale is due to a large inductive electric field, and in the case of pellet ablation, the collision frequency between cold bound electrons in the ablation cloud and the hot background electrons is the fast time scale due to the impurity density being much greater than the background density.

1.3.1 Kinetic equation

To that end, the theoretical tool-of-choice to describe non-thermal particles is the kinetic equation[2], which describes transport of particles through six-dimensional phase space. It is a nonlinear integro-differential equation, and the unknown function in the equation is a probability density function, $f(\vec{x}, \vec{p})$, which describes the likelihood that a particle is in a volume element of size $\mathrm{d}^3x\,\mathrm{d}^3p$ centered on position $\vec{x}$ and momentum $\vec{p}$. The general form of the equation,

$$\frac{\partial f}{\partial t} + \frac{\partial}{\partial z_i} \cdot \dot{z}_i \, f = \hat{\mathcal{C}} \tag{1.4}$$

where $z_i = \vec{x}$ for $i = 1, 2, 3$ and $z_i = \vec{p}$ for $i = 4, 5, 6$. Thus, $\dot{\vec{x}}$ is velocity and dictates how position changes as a function of time, while $\dot{\vec{p}}$ is force, i.e. time-derivative of momentum. Eq. (1.4) has a left-hand-side (LHS) that is conservative, i.e. it is conserves the number of particles in the entire volume of integration. The right-hand-side (RHS) contains the collision operator, $\hat{\mathcal{C}}$, which represents how collisions between particles change their position and momentum. The collision operator can have a Fokker-Planck form – meaning that changes in position and momentum are infinitesimal, e.g. small-angle collisions – or the changes can be discrete as in the case of knock-on[3] collisions. As will be seen, the collision operator does not necessarily conserve particle number.

Chapter 2

Disruption

2.1 Concern

There are many challenges to maintaining fusion in tokamaks, but this work limits the scope to disruption. A disruption is a catastrophic loss of plasma confinement that ultimately concludes with the release of the thermal and magnetic energy stored in the device. Since tokamaks are envisaged for producing electricity, the obvious concern regarding disruptions is to the duty-cycle of commercial power plants but even more concerning is the potential of physical damage to the machine as a result of the energy release. Thermal energy is directly transferred to the walls when plasma control is lost and also through radiation of high-Z impurities which have contaminated the plasma.

Both instances contribute to the deterioration of the metal walls, but a debilitating possibility is presented by **runaway electrons** since they can burn holes in the machine. An inherent feature of the tokamak design is the large current that runs through the center of the torus, and this feature makes the tokamak very inductive. Under nominal conditions, the current is superconducting and carried by bulk electrons, but when the temperature drops (such as during disruption) the plasma becomes resistive, and the current dissipates. There is sufficient magnetic energy stored in the device to maintain the current during disruption, but there is a chance that the current carriers are primarily (if not entirely) relativistic electrons. For sufficiently fast electrons, the friction force decreases (as opposed to increases per our normal experience with drag forces) with the momentum of the electron, and hence, the induced electric field preferentially accelerates the fastest electrons. This can lead to the runaway regime where electrons are accelerated indefinitely to velocities approaching the speed of light. The number of runaway electrons can exponentiate as a result of knock-on collisions in a process known as avalanche[3].

Additional concerns are vertical displacement events and mechanical loads caused by the interaction between the magnetic field and currents (e.g. halo, eddy) induced in the structure caused by the displacement of the plasma. We spend very little discussion on these aspects, except on how it guides the strategies developed for dealing with disruptions.

2.2 Thermal and Current Quench

Disruptions are composed of two phases: a fast thermal quench and a relatively slower current quench. Causes of the rapid cooling that occurs during thermal quench varies. A survey of over two thousand disruptions occurring over a decade at JET is conducted in [4], and the statistics reveal two majority causes for rapid cooling: strong radiative losses due to impurity influx and global MHD events that stochasticize magnetic field lines which can lead to enhanced heat transport. These two causes are not necessarily mutually exclusive. The current decreases since the conductivity[5],

$$\sigma = \frac{T^{3/2}}{\pi\, Ze^2 \sqrt{m} \ln \Lambda} \tag{2.1}$$

also decreases with temperature, though the current dissipates at a slower inductive time scale. That is, an electric field is produced which resists the change in current. It is during this phase that it is possible to accelerate a significant population of electrons to relativistic energies.

2.3 Strategy

Experiments have been performed to understand the deleterious effects of disruption. It is difficult to extrapolate these results to a machine as large as ITER because of the difference in scale with even the largest current-generation tokamak, which is JET. Even so, it is clear that disruptions pose a significant danger, especially with regards to runaway electrons since ITER's larger current and longer discharge times make it susceptible to runaway avalanche. A scheme must be devised to deal with this danger, and there are two platforms to consider: avoidance versus mitigation. Boozer [6] likens these two aspects to proper steering versus airbags of a car. Ideally, tokamaks would be engineered to completely avoid disruption thus alleviating the need to devise mitigation strategies. However, accidents happen even to the most capable drivers, so the ITER mission must plan for the worst. One challenge in the metaphor of

[6] is that, in the case of disruption, the airbags need to be deployed preemptively. To that end, the ability to reliably predict disruptions is imperative. More recent techniques involve machine-learning[7] to predict disruptions. If a disruption is deemed imminent, the general strategy is to preemptively cool the plasma; that is, engineer a disruption which does not pose a significant danger.

2.3.1 Cooling methods

Proposed methods of cooling include: cross-surface transport, magnetic surface breakup, and radiation. The cooling must occur sufficiently quickly to avoid the danger of halo currents, but not too quickly as to generate runaways. The author of [8] estimates the former two methods to be too slow. On the other hand, radiative cooling (which is achieved by injecting high-Z impurities into healthy plasma) can, in principle, meet the temporal constraints. Two methods have been explored for injecting impurities into the plasma: massive gas injection, which puffs gas at high pressure; pellet injection fires cryogenic material at high velocity. Pellets are favorable to massive gas injection due to deeper penetration of the impurity material into the plasma and the ability to adjust the cooling properties. This is accomplished via mixing fractions of the impurity and shattering the pellet into multiple pieces inside the injection tube[9]. The former strategy aims to reduce the risk of runaway production, while the latter aims to increase the spatial distribution of the impurity and thereby reduce radiative heat loading. At the time of this writing, shattered pellet injection is the proposed method of cooling for disruption mitigation at ITER[10].

Chapter 3

Runaway Electrons

Runaway electrons are encountered in atmosphere where they may trigger breakdown leading to lightning[11], magnetic reconnection events during solar flares[12], and in energetic electron beams. This work, however, will focus on their impact to tokamak plasmas where runaways can be ubiquitous during the current quench phase of a disruption. The existence of highly energetic particles in thunderclouds was proposed by Wilson in 1925[13]. Wilson observed ionization tracks inside a cloud chamber (which he invented and ultimately received the Nobel Prize for) and noted that tracks were straighter for electrons accelerated by large electric fields. This ultimately lead to the insight that particles can enter a energy regime where collisions are less frequent. These particles came to be known as **runaways** since they can be accelerated continuously and do not seem to approach a terminal velocity.

The friction force experienced by electrons in a plasma due to collisions with bulk electrons is depicted in Fig. 3.1. For electron velocities small compared to the thermal velocity, $v_{th} = \sqrt{2T/m}$ where T is the temperature of the bulk plasma and m is the electron mass, the friction increases linearly with velocity. Collisions, however, become less frequent as velocities exceed the thermal velocity. For supra-thermal electrons, the friction force is[14]

$$\left|\frac{\mathrm{d}p}{\mathrm{d}t}\right| = \frac{\gamma+1}{\gamma} \times mv\nu(v) = \frac{\gamma+1}{\gamma} \times \frac{4\pi e^4\, n \ln\Lambda}{mv^2} \tag{3.1}$$

The Lorentz factor is $\gamma = 1/\sqrt{1-(v/c)^2}$, and the collision frequency between fast electrons with velocity v and a background with electron density n is

$$\nu(v) = \frac{4\pi e^4\, n \ln\Lambda}{m^2 v^3} \tag{3.2}$$

The Coulomb logarithm is defined as $\ln\Lambda = \ln(b_{max}/b_{min})$, i.e. the logarithm of the ratio of the maximum and minimum impact parameters characterizing the collisional process. Examples of these logarithms are collected in Sec.IIIB of [15] and are particularly useful because the expressions are relativistic.

Eq. 3.2 indicates that the friction force asymptotes when the electrons become ultra-relativistic, i.e. $v \to c$. The minimum electric field required to accelerate ultra-relativistic electrons is called the Connor-Hastie field[17] and is given by

$$E_C = \frac{4\pi e^3\, n \ln\Lambda}{mc^2} \tag{3.3}$$

When the field exceeds E_C, there exists a critical particle velocity v_{crit} beyond which particles with $v \geq v_{crit}$ runaway. Because these velocities approach the speed of light, it is apropos to express the criticality in terms of momentum as opposed to velocity, e.g.

$$p_{crit} = \frac{mc}{\sqrt{E/E_C - 1}} \tag{3.4}$$

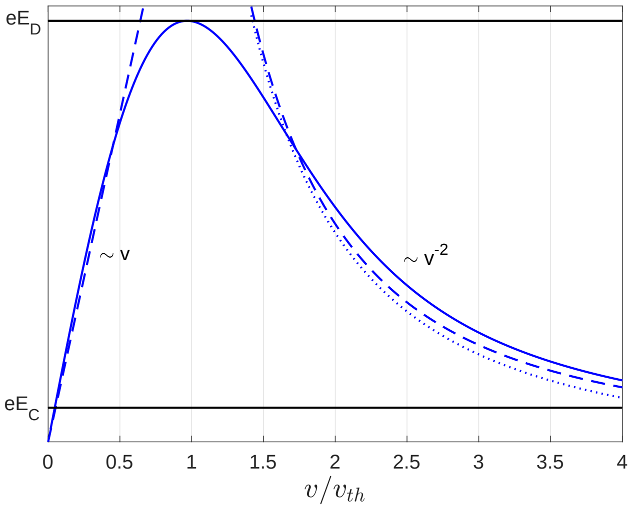

Figure 3.1: Collisional drag forces. The blue solid and dashed lines are obtained from [16] while the blue dotted line is obtained from [14]. The Connor-Hastie and Dreicer limits are indicated. The Dreicer limit corresponds to when the friction force is greatest, i.e. when $v = v_{th}$.

On the other hand, the minimum electric field required to accelerate the entire population of electrons into the runaway regime is the Dreicer field[18],

$$E_D = \frac{4\pi e^3 \, n \ln \Lambda}{T} \implies \frac{E_C}{E_D} = \frac{T}{mc^2} \tag{3.5}$$

For fusion-grade plasmas, $E_C/E_D \ll 1$.

3.1 Synchrotron Radiation

So far, it would seem that runaways accelerate indefinitely, but the speed of light is a universal limit, and no mention has been given to what ultimately slows the runaways down. Charged particles that are accelerating emit radiation. Owing to the large magnetic fields in tokamaks (and hence, fast gyro-motion), runaways will primarily lose energy via synchrotron radiation. (In zero magnetic field, bremsstrahlung would otherwise be the slowing-down force.) For early works on synchrotron radiation, see [19, 20]. Synchrotron radiation (called cyclotron for non-relativistic particles) occurs when a charged particle has some component of its momentum perpendicular to the magnetic field. That said, the radiation is emitted predominantly in the direction of the particle motion, i.e. typically along the magnetic field lines, and there is a radiation-reaction force that reduces the parallel momentum. Synchrotron radiation tends to reduce the pitch-angle, as well, but elastic scattering ensures the pitch-angle does not remain zero for longer than one collision time. In fact, part of the mitigation strategy for runaways involves injecting impurities in the plasma to enhance pitch-angle scattering, and consequently, synchrotron radiation. In addition, synchrotron radiation provides a diagnostic for the energy of the runaways[21].

The frequency of the synchrotron radiation emitted by the runaways is a multiple of the gryo-frequency, $\omega_c \equiv eB/mc$. The single-particle synchrotron power spectra is[22]

$$P(\lambda) = \frac{4\pi}{\sqrt{3}} \frac{e^2 c}{\lambda^3 \gamma^2} \int_{\lambda_c/\lambda}^{\infty} K_{5/3}(l)\, \mathrm{d}l \tag{3.6}$$

where λ is the wavelength of emission, $K_\nu(x)$ is the modified Bessel function of the second kind, and $\lambda_c \equiv (4\pi/3)c/\gamma^2\omega_c$. The emission spans from microwaves to hard x-rays, depending on the gyro-frequency; for tokamaks, the spectrum is peaked in the near-infrared (micrometer) range, though visible light has been observed, as well, for highly energetic runaway beams. Eq. (3.6) describes the spectra in a straight magnetic field; for a toroidal field, see [23].

3.2 Primary/Seed Runaways in Tokamak

Runaways can be generated during the start-up phase of the tokamak since a strong electric field is required to ionize the gas, but the current associated with them remains relatively small by time the plasma becomes superconducting. The electric field associated with the superconducting current is less than the Connor-Hastie field, and so these initial runaways eventually slow down.

Outside of the start-up phase, the electric field typically remains small compared to E_D. That said, runaways can still be generated even at fields $E \ll E_D$ due to diffusive transport in momentum-space. This production mechanism (eventually coined Dreicer mechanism) was first estimated in [18]. Dreicer argued that electrons with $p > p_{crit}$ become runaways within roughly one collision time, and thus, the growth rate of the runaway density goes roughly as

$$\frac{\mathrm{d}n_r}{\mathrm{d}t} \sim n \times \frac{eE_D}{\sqrt{mT}} \exp\left(-\frac{E_D}{2E}\right) \tag{3.7}$$

More refined calculations have since been developed (e.g. [17, 24–26]). Nonetheless Eq. (3.7) contains important features of the diffusive growth rate, such as the exponentially small dependence on E_D/E and not E_C/E. Hence, for small fields compared to E_D, runaway production is meager.

If the bulk plasma is cooled at a rate much faster than the collisional time scale, the bulk electrons may divide into cold and hot populations. Because collisions are less frequent for the hotter population, they do not thermalize with the cold electrons during rapid cooling and become prone to running away. This is the so-called **hot-tail** mechanism described in [27]. This situation arises, for example, when impurity material is injected into healthy plasma in the disruption mitigation scenario[10].

3.3 Secondary runaway electrons

The production mechanisms outlined above pertain to primary or seed runaway electrons. Primary electrons produced by Dreicer acceleration are relatively benign in fusion-grade tokamaks such as ITER[28, 29]. The real concern is that they serve as seed particles for **runaway avalanche**. Dreicer production is associated with diffusive transport of bulk electrons into the runaway regime via small-angle collisions, which are associated with infinitesimal changes in energy. Avalanche production involves large-angle or knock-on collisions and discrete changes in energy. An incident relativistic electron can transfer a significant amount of its initial kinetic energy in a knock-on collision to boost a thermal electron to relativistic energies. If, in addition, the final energy of the incident electron is relativistic[1], then this process concludes with a net gain of one runaway electron. Each of these runaways are accelerated and can undergo another knock-on collision. The avalanche mechanism is so-called because it results in an exponentiation of the seed runaways. This is reflected in the avalanche growth rate first calculated by Rosenbluth and Putvinski[3] for a cylindrical plasma with an effective ion charge Z_{eff},

$$\frac{\mathrm{d}n_r}{\mathrm{d}t} \sim n_r \times \frac{eE_C}{mc} \cdot \frac{E/E_C - 1}{\ln\Lambda}\left[1 - \frac{1}{E/E_C} + \frac{4(Z_{eff}+1)^2}{3(Z_{eff}+5)/\pi[(E/E_C)^2+3]}\right] \tag{3.8}$$

since it is proportional to n_r [and not n as in Eq. (3.7) for Dreicer production]. The avalanche growth rate has a nearly linear dependence on E, whereas Eq. (3.7) is exponential in E. This means that avalanche is the prevalent mechanism in weaker electric fields[2], while Dreicer is prevalent in strong fields. Knock-on collisions are expected to be the main mechanism for runaway electron production in ITER but occur at a much slower rate (by a factor of the Coulomb logarithm) compared to small-angle collisions.

3.3.1 Avalanche rate in strong electric field

In the limit of $E \gg E_C$, the avalanche growth rate approximates to

$$\frac{\mathrm{d}n_r}{\mathrm{d}t} \approx n_r \times \frac{eE}{mc} \cdot \frac{1}{\ln\Lambda\sqrt{Z_{eff}+5}} \tag{3.9}$$

We can estimate the amount of current carried by the runaways as they multiply when the inductive field is large. The growth of the current carried by

---

[1] The incident electron must have initial momentum $p \geq p_{crit}$.

[2] Although, there must be a population of seed runaways to begin with.

the runaways immediately follows from Eq. (3.9), viz.

$$\frac{1}{I_r}\frac{\mathrm{d}I_r}{\mathrm{d}t} = -\frac{\ell_i}{\ln\Lambda\sqrt{Z_{eff}+5}}\frac{\mathrm{d}I}{\mathrm{d}t} \tag{3.10}$$

where $\ell_i = \mathcal{O}(1)$ is a shape factor which characterizes the inductance of the toroidal current, and I is the toroidal current. (See also [30].) The inductive field is related to the change in total current as

$$E = -\frac{\ell_i}{c^2}\frac{\mathrm{d}I}{\mathrm{d}t} \tag{3.11}$$

and to the Ohmic current by

$$E = \frac{\eta}{S}(I - I_r) \tag{3.12}$$

where η is the bulk plasma resistivity and S is the plasma cross-section. Eq. (3.10)-(3.12) comprises a close set of equations which is easily integrated (assuming that the internal inductance remains constant). The evolution of the total and runaway current is shown in Fig. 3.2 for multiple values of fixed ℓ_i. The figure shows the tendency of the total current to eventually be carried entirely by the runaways at a time scale comparable to the Ohmic decay time, $(\ell_i/c^2)\,S/\eta$. Furthermore, the total current equilibrates to a value given by[30]

$$\log\left(\frac{I_r(\infty)}{I_r(0)}\right) = \frac{\ell_i}{\ln\Lambda\sqrt{Z_{eff}+5}}\frac{I(0)-I(\infty)}{I_A} \tag{3.13}$$

where $I(0)$ and $I(\infty)$ are the initial and final values of the total current (and likewise for I_r), and $I_A \equiv mc^3/e$ is the Alfvén current.

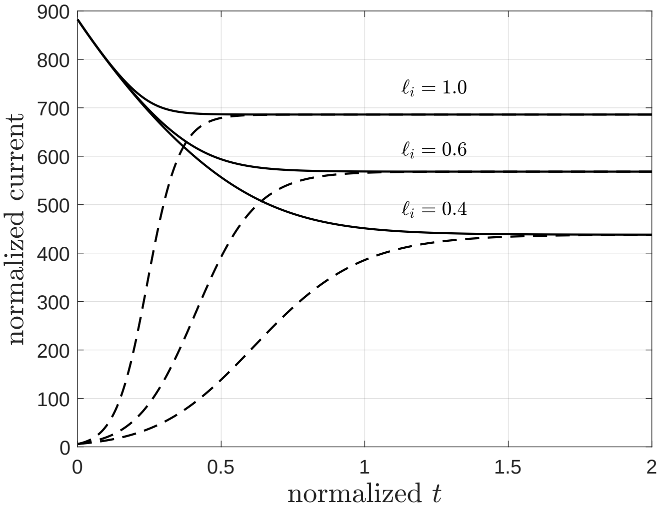

Figure 3.2: Runaway current. Time is normalized to units of $(\ell_i/c^2)\,S/\eta$, while current is normalized to the Alfvén current, I_A.

3.4 Marginal stability

In the previous section, the fast avalanche process that occurs as a result of the large thermal-quench-induced electric field was discussed. It was seen that a significant fraction of the current is quickly saturated by runaways. The runaway current thereafter dissipates concurrently with the stored magnetic energy but the rate at which it does so is relatively slower than the thermal quench. The dissipation follows the self-sustained marginal criticality scenario[31] whereby the inductive electric field straddles a threshold value that ensures a balance between avalanche multiplication and a diffusive leak of the existing runaways into the bulk. An estimate for the current decay was given by Breizman[31] as

$$\tau_d \sim \frac{I}{c^2 \, E_0} \tag{3.14}$$

where E_0 is the threshold field. The ratio of the current decay time to the avalanche growth rate,

$$\tau_{av} \sim \frac{mc \, \ln \Lambda}{eE} \tag{3.15}$$

is large for $E = 2E_0$, i.e. $\tau_d/\tau_{av} \sim eI/mc^3 \ln \Lambda$, which means that runaways will have ample opportunity to multiply. And in fact, experimental evidence[32] suggests that the avalanche threshold field exceeds E_C. If $E < E_C$, the runaway current is not sustained because small-angle collisions would cause the runaways to slow down on a time-scale faster than the lifetime of the runaway current.

3.5 Kinetic equation describing seed runaways

Small-angle collision rates differ by their knock-on counterpart by the Coulomb logarithm which is $\sim 10-20$ for fusion-grade plasmas. The disparity between knock-on versus small-angle collisions (at modest values of the electric field) precipitates a separation of timescale that enables considering the pre-existing runaway (seed) evolution apart from that of the multiplying runaway population. That is, we first ignore knock-on collisions and determine how the seed runaways equilibrate in phase-space. Then we use the resulting distribution function of seed runaways to predict whether or not they ultimately decay or multiply.

To that end, we solve the relativistic kinetic equation describing the seed runaways. We consider runaways in a uniform fully ionized plasma and uniform magnetic field in order to circumvent discussion of secondary geometric effects. Thus, the kinetic equation describing the evolution of the runaway momentum p and pitch-angle θ with respect to the field B is[15]

$$\begin{aligned}\frac{\partial f}{\partial t} + \frac{1}{p^2}\frac{\partial}{\partial p}p^2\left[|eE|\cos\theta - \frac{mc}{\tau_c}\left(1+\frac{m^2c^2}{p^2}\right) - \frac{1}{mc\,\tau_{rad}}p\sqrt{p^2+m^2c^2}\sin^2\theta\right]f \\ = \frac{1}{p\sin\theta}\frac{\partial}{\partial\theta}\sin\theta\left[|eE|\sin\theta\, f + \frac{Z_{eff}+1}{2\tau_c}\frac{m^2c^2\sqrt{p^2+m^2c^2}}{p^2}\frac{\partial f}{\partial\theta} + \frac{mc}{\tau_{rad}}\frac{p\sin\theta\cos\theta}{\sqrt{p^2+m^2c^2}}f\right]\end{aligned} \tag{3.16}$$

which includes acceleration by the electric field E, inelastic collisions with bulk electrons, elastic collisions with bulk electrons and ions, and synchrotron radiation. The collisional and radiative timescales are

$$\tau_c = \frac{m^2c^3}{4\pi e^4 n\ln\Lambda} = \frac{mc}{eE_C} \tag{3.17}$$

$$\tau_{rad} = \frac{3m^3c^5}{2e^4B^2} \tag{3.18}$$

respectively. It is convenient to assume a dimensionless form of Eq. (3.16), and we do so using the following normalizations:

$$t \to \frac{t}{\tau_c}, \quad p \to \frac{p}{mc}, \quad E \to \frac{E}{E_C} \tag{3.19}$$

which results in

$$\begin{aligned}\frac{\partial f}{\partial t} &+ \frac{1}{p^2}\frac{\partial}{\partial p}p^2\left[E\cos\theta - \frac{p^2+1}{p^2} - \frac{1}{\bar{\tau}}p\sqrt{p^2+1}\sin^2\theta\right]f \\ &= \frac{1}{p\sin\theta}\frac{\partial}{\partial\theta}\sin\theta\left[E\sin\theta\, f + \frac{Z_{eff}+1}{2}\frac{p^2+1}{p^2}\frac{\partial f}{\partial\theta} + \frac{1}{\bar{\tau}}\frac{p\sin\theta\cos\theta}{\sqrt{p^2+1}}f\right]\end{aligned} \tag{3.20}$$

The form of Eq. (3.20) implies that the field accelerates pre-existing runaways and does not generate new ones via the Dreicer mechanism. The linear form of the collision operator is a consequence of the runaways being a minority in the plasma. The collision operator describes only small-angle collisions between fast electrons and the thermal electrons and ions. Synchrotron radiation shrinks the pitch-angle, but this is of secondary importance to the radiation-reaction force, and therefore, we will neglect it. This is a reasonable accommodation since $\bar{\tau} \sim 100$ for ITER. As already mentioned, the separation in timescale allows us to omit the avalanche source. Since there is no source of new runaways, any change in the particle number is due to a flux through the momentum space domain.

3.5.1 Threshold field for sustainment

It is apparent that no runaways can be sustained for an electric field less than the Connor-Hastie field, i.e. $E < 1$, since electrons will immediately slow down into the thermal bulk. Conversely, even at fields $E \gg 1$, synchrotron radiation precludes ultra-relativistic electrons from completely running away. The balance of acceleration by the electric field against the drag forces suggests that the existence of stagnation points in phase-space whose locations depend on E. Clearly, the existence of such points requires that E must exceed some threshold value that counters the transport of fast electrons to the thermal bulk. Aleynikov and Breizman[33] reduced Eq. (3.20) to one-dimensional transport along p in the limit that pitch-angle shrinking caused by the electric field is balanced by pitch-angle scattering. The flow velocity associated with the transport is

$$\begin{aligned} U(p) \equiv & -\left[\frac{1}{A(p)} - \frac{1}{\tanh[A(p)]}\right] E - \frac{p^2+1}{p^2} \\ & + \frac{Z_{eff}+1}{\bar{\tau}\, E} \frac{p^2+1}{p^2} \left[\frac{1}{A(p)} - \frac{1}{\tanh[A(p)]}\right] \end{aligned} \tag{3.21}$$

where

$$A(p) \equiv \frac{2E}{Z+1} \frac{p^2}{\sqrt{p^2+1}} \tag{3.22}$$

and is plotted in Fig. 3.4. The flow velocity is negative throughout if E is less than some threshold value, E_0. Correspondingly, all the runaways eventually return to the bulk. For $E > E_0$, fast electrons with $p > p_{min}$ tend to accumulate at p_{max} (corresponding to a long-lived runaway population), and those with $p < p_{min}$ return to the bulk. Thus, p_{max} is a stable point and p_{min} is an unstable point. The situation when p_{min} and p_{max} are co-located corresponds to the *threshold field for sustainment* of fast electrons. An approximate expression for the threshold field is[33]

$$E_0 = 1 + \frac{\alpha}{(\frac{1}{8} + \alpha^2)^{1/6}} \tag{3.23}$$

where

$$\alpha \equiv \frac{Z_{eff}+1}{\sqrt{\bar{\tau}}} \tag{3.24}$$

and plotted in Fig. 3.23. The threshold field increases with α corresponding to larger Z_{eff} and/or smaller $\bar{\tau}$, both of which corresponds to faster collision rates. Hence, the role of collisions are critical to the lifetime of runaway electrons.

A meaningful examination of the seed runaways must be conducted in the regime in which the lifetime of the seed runaways is longer than the thermal quench time but shorter than the current quench time. The first of constraint ensures that the seed can be amplified during thermal quench, while the second implies that the avalanche-produced runaways balance the losses of the pre-existing ones in a self-sustained marginal stability scenario.

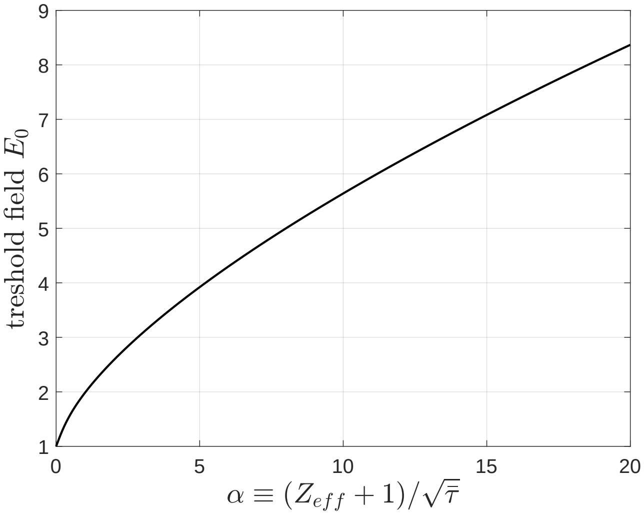

Figure 3.3: Threshold field versus $\alpha \equiv (Z_{eff}+1)/\sqrt{\bar{\tau}}$.

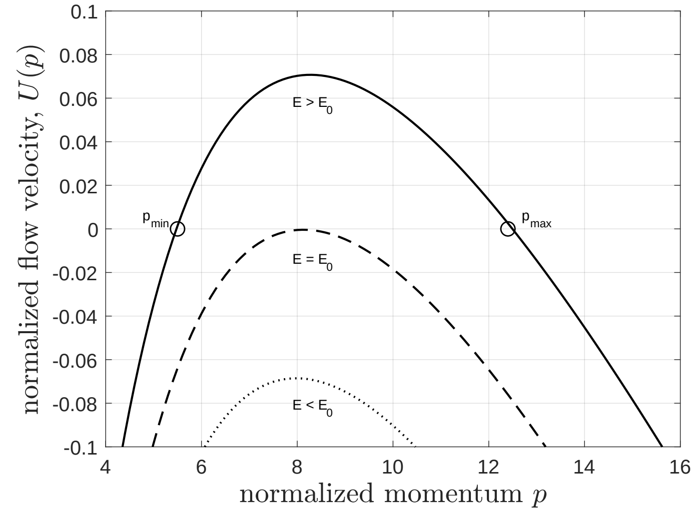

Figure 3.4: Stagnation in sustainment threshold regime.

3.5.2 Structure of seed runaways

In the one-dimensional kinetic theory of [33], particles with $p < p_{min}$ slow into the bulk, while those with $p > p_{min}$ eventually accumulate at p_{max}. This would correspond to a delta-distribution of seed runaways with infinite lifetime ripe for multiplication. Peaking of the distribution is also observed in [34]. However, as demonstrated in [35], the lifetime of the runaways is finite. Referring back to Fig. 3.4, the main body of runaways accumulated at p_{max} is actually Gaussian[35]; thus, a non-zero number of runaways in the wing of the distribution extending towards lower momentum will have $p < p_{min}$ and slow down into the bulk. Two-dimensional kinetic analysis is emphasized in[35] in determining the shape of the runaway *attractor* (see Fig. 3.5), and similarly in

[36] – though the feature is referred to as a ”vortex” therein. The main body of the attractor is located at relativistic values of momentum and collimated at small pitch-angles. In the ultra-relativistic tail, the distribution function goes as[37]

$$\log F \sim -2p - p^2\theta^2 \tag{3.25}$$

where $F = p^2 f$. This expression exhibits exponential decay with pitch-angle, but its applicability fails when $p^2\theta^2 \geq p$. At larges values of $p^2\theta^2 \geq p$, the distribution function goes as[35]

$$\log F \sim -p^3\theta^4 \tag{3.26}$$

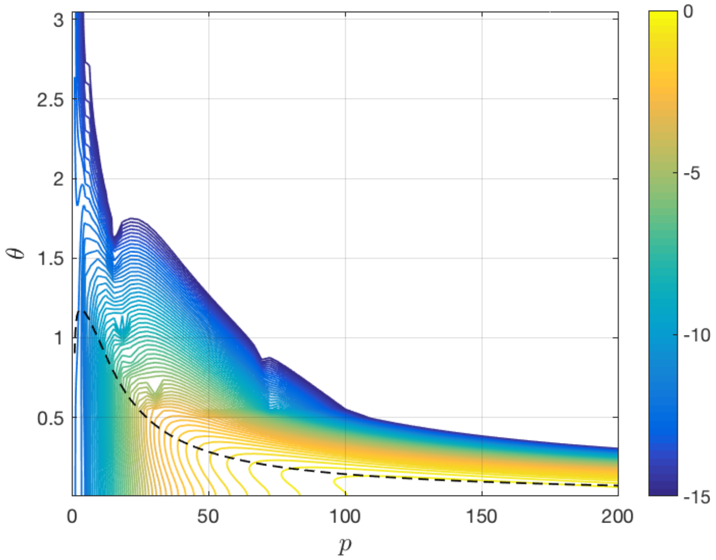

Figure 3.5: The distribution function $\log_{10}(f)$ of seed runaways near attractor; $E = 3.1$, $\bar{\tau} = 100$, $Z_{eff} = 5$.

3.5.3 Lifetime of seed runaways

Although the majority of seed electrons eventually accumulate in the vicinity of the attractor (e.g. near p_{max} in the one-dimensional theory), the distribution far from the attractor extending towards the thermal bulk ultimately determines the lifetime of the seed runaways. In the two-dimensional analysis, p_{min} corresponds to a separatrix in momentum-space (plotted, for example, in Fig. 3.6). Convective flows tends to steer runaways towards the attractor, but elastic scattering enables diffusive transport across the separatrix. Particles scattering across this semi-permeable barrier enter a slowing-down region and inevitably return to the thermal bulk. Increasing the electric field minimizes the slowing-down region while also increasing the separation between p_{min} and p_{max}[35]. The lifetime τ_ℓ of seed runaways as a function of E for several values of α (see Fig. 3.7) was calculated in [35] by evolving Eq. (3.20) numerically. The results show that the lifetime increases exponentially with electric field. This motivated re-casting Eq. (3.20) in the form of an eigenvalue relation by letting $\partial f/\partial t \to -f/\tau_\ell$. Semi-analytic results for τ_ℓ were also found in [35] when $\alpha \ll 1$ (see Fig. 3.8). This case corresponds to when the threshold field barely exceeds the Connor-Hastie value.

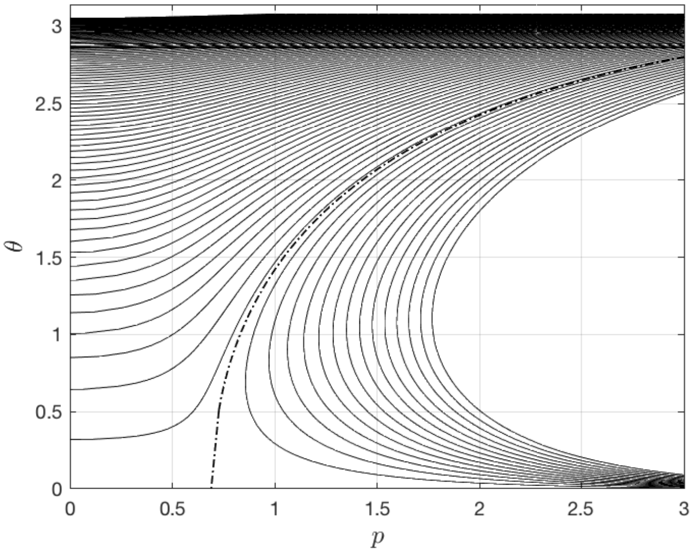

Figure 3.6: Convective trajectories in the slowing-down region of momentum-space depict a separatrix (sketched as a dash-dotted line). On one side of the separatrix, particles inevitably return to the bulk, while on the other, particles gain momentum; $E = 3.1$, $\bar{\tau} = 100$, $Z_{eff} = 5$.

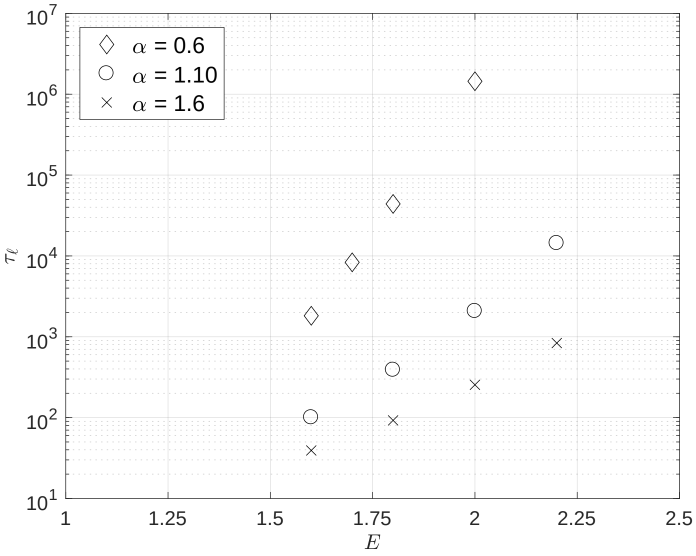

Figure 3.7: Lifetime of the runaway seed (log scale) versus electric field for various values of the parameter $\alpha \equiv (Z_{eff} + 1)/\sqrt{\bar{\tau}}$. Time is normalized to collisional time scale, τ_c.

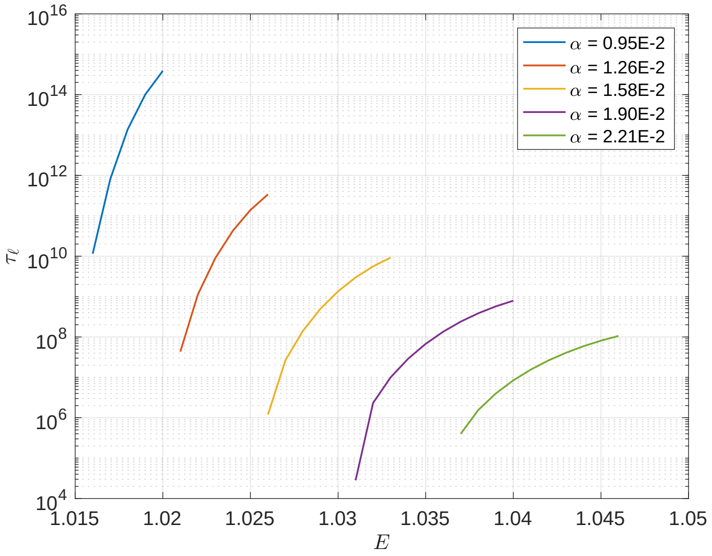

Figure 3.8: Lifetime of the runaway seed (log scale) versus electric field in the limit that $\alpha \ll 1$. The deviation from exponential behavior with E indicates applicability limit.

Chapter 4

Pellet Ablation

Spitzer and Tonks[38] initially intuited that frozen pellets of deuterium and tritium could be used to refuel fusion reactors. The thought was that the self-shielding mechanism of the cloud created by the sublimation of the frozen material would prolong the pellet lifetime and allow the pellet to travel all the way to the plasma core. Since then pellets have been imagined for other uses such as diagnostics[39], plasma control[40], and plasma shutdown in killer pellet strategies[41]. The killer pellet strategy, however, is too drastic for ITER because the fast shutdown makes the machine susceptible to runaway electrons. That being said, there is optimism that pellets can be engineered to safely terminate a fusion plasma in order to avoid damage caused by disruption. For example, mixtures of deuterium and neon are being tested[9] to straddle the time constraints imposed by thermal and current quench. Furthermore, the shattered pellet injection strategy[42] was imagined as a way to avoid localization of the impurity material and minimize radiative heat loads on the walls. As of this moment, shattered pellet injection is the envisaged strategy[10] for mitigating disruptions in ITER.

The rest of this chapter is devoted to the description of pellet heating and ablation in fusion-grade plasma.

4.1 Physical description of pellet ablation

Almost immediately after a cryogenic pellet is immersed in plasma, ambient electrons[1] heat the pellet surface and atoms are sublimated from the surface. The sublimated atoms form a gas *shield* which surrounds the pellet and absorbs the incoming heat flux. The strength of the shielding is primarily a function of the line-integrated density (or optical thickness), $\int N \,\mathrm{d}\ell$, where $\mathrm{d}\ell$ is the infinitesimal path length taken by the incident electrons. However, this shielding diminishes as the cloud is heated[2] and expands which reduces $\int N \,\mathrm{d}\ell$ and allows electrons to penetrate to the surface once again and rejuvenate the gas shield. Thus, pellet ablation is considered a self-regulatory process in the sense that the shield maintains enough transparency to enable rejuvenation. Additional shielding mechanisms exist, i.e. magnetic shielding due to expulsion of the field lines from the cloud interior and electostatic shielding. The electrostatic shielding which takes the form of a sheath at the interface of the cloud and background plasma is a result of the charge imbalance as plasma electrons penetrate the gas shield. However, we do not consider these addi-

---

[1] Ion heating is considered secondary.

[2] Additionally, the heating causes the gas shield to become a plasma shield. However, ionization primarily occurs in the periphery of the shield where $\int N \,\mathrm{d}\ell$ is smallest. The strongest shielding occurs near the surface where the cloud is neutral, and hence we forgo discussion of the plasma shield.

tional shielding mechanisms. Electrostatic shielding, in the context of high-Z impurity pellets, is considered weak as discussed further below[3].

The amount of material heated by the fast electrons at the surface of the pellet depends on the penetration depth of the electrons. This depth depends on whether or not the pellet is of high-Z material. For low-Z pellets, the penetration depth is roughly the stopping length associated with the slowing-down force. The background plasma has density n_∞ and temperature T_∞. Thus, incident electrons with thermal velocity $v_{th} = \sqrt{2T_\infty/m}$ have a mean collision frequency[16] of

$$\bar{\nu} = \frac{4\pi Z e^4 \, N \ln \Lambda_{in}}{m^2 v_{th}^3} \tag{4.1}$$

in a material with atomic density N. The mean stopping length is

$$\lambda = \frac{v_{th}}{\bar{\nu}} = \frac{T_\infty^2}{\pi Z N e^4 \ln \Lambda_{in}} \tag{4.2}$$

The inelastic Coulomb logarithm, $\ln \Lambda_{in}$, contains the ratio of the minimum and maximum impact parameters for collisions between the hot plasma electrons and the bound electrons of the pellet material. The minimum impact parameter is the deBroglie wavelength, $\hbar/mv$, while the maximum impact parameter is $v \times \hbar/2I$ since the ionizing collision should occur on a timescale shorter than the bound electron orbital period, $\hbar/2I$, where I is the mean

---

[3] Magnetic shielding is not significant for current-generation experiments but that may change for ITER.

excitation potential of the bound electrons. Consequently, $\ln \Lambda_{in} = \ln(E/I)$. A comprehensive discussion of the Coulomb logarithm (including relativistic scenarios) can be found in [15].

The path traveled by electrons through high-Z material is different. In this case, incident electrons perform a random walk through the material due to the prevalence of elastic scattering. In this case, the penetration depth is the net displacement achieved during the slowing-down time, $\bar{\nu}^{-1}$, i.e. $\lambda_Z \sim \sqrt{D\,\bar{\nu}^{-1}} = \sqrt{(\lambda/Z)\,v_{th}\bar{\nu}^{-1}}$, where $D \sim (\lambda/Z)v_{th}$ is the diffusion coefficient, and (λ/Z) is the mean-free-path associated with 90-degree scattering. Consequently, the penetration depth through high-Z material is

$$\lambda_Z \sim \lambda/\sqrt{Z} = \frac{T_\infty^2}{2\pi Z^{3/2} e^4\, N \ln \Lambda_{in}} \tag{4.3}$$

For keV ambient electrons, the surface layer thickness of an ablating solid-state pellet of density $10^{21}\,cm^{-3}$ is on the order of $10^{-1}/Z^{3/2}\,cm$, and so for $Z \gg 1$, the surface layer is much thinner than the radius of a typical pellet which is $R_p \sim 0.1 - 1\,cm$. This layer forms a cold cloud of neutral atoms surrounding the pellet which throttles the heat flux reaching the surface. This cloud heats up, expands, and it becomes semi-transparent when the layer thickness is comparable to the pellet radius. Hot electrons can then reach the pellet surface and heat the next layer, which leads to continuous ablation. At around ten times R_p the shielding becomes negligible, and the ambient electron distribution function remains unperturbed by the impurity cloud at this distance.

The additional shielding mechanism due to an electrostatic sheath at the interface between the cloud and the ambient plasma maintains ambipolarity, but its role is of secondary importance in the high-Z limit. This is because the net particle flux (but not the heat flux) is relatively small due to backscatter in the high-Z case.

The description of pellet ablation in a tokamak should generally take into account the role of the magnetic field. For a magnetic field strength of $10\,kG$, the magnetic pressure is typically much smaller than the gas pressure within the narrow layer at the pellet surface. Also, the gas is essentially neutral in this area, and therefore, its expansion should not be affected by the magnetic field unlike at further distances where the gas is ionized. What is affected by the magnetic field is the motion of hot electrons in the ablation cloud, which varies between longitudinal (along the field lines) or radial with respect to the pellet center. The direction depends on the ratio of the electron gyro-frequency to the elastic collision frequency inside the cloud. The gyro-frequency is $\omega_c = eB/mc$. The elastic collision frequency[43] is

$$\nu_s(v) = Z\nu(v) \times \frac{\ln \Lambda_{el}}{\ln \Lambda_{in}} \tag{4.4}$$

where $\nu(v)$ is nearly the same as Eq. (3.2) and $\ln \Lambda_{el}$ is the elastic scattering logarithm. It is equal to

$$\ln \Lambda_{el} \approx \ln \left(\frac{0.591}{b\, Z^{1/3}} \frac{a_0}{\hbar/mv} \right), \tag{4.5}$$

where a_0 is the Bohr radius and $b \approx 0.5 - 0.6$ but depends on the atomic species[44]. Taking reactor-grade parameters, as an example, the gyro-frequency is $\omega_c \approx 2 \times 10^{11}\, s^{-1}$ for a $10\, kG$ field. The elastic collision frequency of $2\, keV$ electrons is comparable to this in cloud densities of $N \approx 10^{19}\, cm^{-3}$, which suggests that we must be cognizant of the magnetic field's impact on pellet heating.

4.1.1 Scaling laws

The most relevant conclusion from an analysis involving pellets is the ablation rate. A convenient scaling law for the ablation rate is derived as a function of plasma and pellet parameters. The ambient plasma electrons of density n_∞ have a mean-free-path of $\lambda_\infty = T_\infty^2/\pi e^4\, n_\infty \ln \Lambda_{in}$. For typical plasma parameters, the mean-free-path is much longer than the scale of the machine[4], and therefore, they travel freely until they encounter the impurity pellet which has density $N \gg n_\infty$. The mean-free-path of the streaming electrons drastically reduces to Eq. (4.2) upon incidence. Plasma electrons carry an initial energy density of $n_\infty m v_{th}^2$, but as they stream through the cold impurities, energy is lost mostly due to collisions with bound electrons. The power density transferred to the cold pellet material is estimated by

$$Q \sim n_\infty m v_{th}^2 \times \bar{\nu} = \frac{2^{3/2}\pi e^4}{m^{1/2}} \frac{Z N n_\infty \ln \Lambda_{in}}{T_\infty^{1/2}} \tag{4.6}$$

---

[4] E.g. in ITER, $\lambda \approx 20\, km$.

where in what follows, the similarity symbol indicates that the relation holds within an un-determined constant of order unity. Eventually, atoms are ablated from the surface of the pellet which expands with a velocity that is roughly sonic. When the flow velocity becomes sonic, i.e. $\gamma T_*/M = V_*^2$, the ablation cloud has been heated to

$$T_* \sim A_* \times (R_*/V_*) \Longrightarrow V_*^3 \sim \frac{\gamma R_* A_*}{M} \sim 2^{3/2}\pi\,\gamma \frac{e^4}{m^{1/2}M} \times R_* \times \frac{Z n_\infty \ln \Lambda_{in}}{T_\infty^{1/2}} \tag{4.7}$$

where γ is the specific heat ratio, M is the atomic mass of the ablated particles, R_* is the sonic radius, and $A_* = Q_*/N$ is the heating rate per atom at the sonic radius. (We use starred notations to indicate sonic quantities.) We have taken Q_* to be equal to Eq. (4.6) to within a factor of unity. The cloud velocity at the pellet surface, i.e. the pellet regression speed, is obtained by the relation, $\dot{R}_p/\lambda_p = V_*/R_*$, where R_p is the pellet radius. Thus,

$$\dot{R}_p \sim \frac{1}{\pi^{2/3}(e^4)^{2/3}} \left(\frac{\gamma}{m^{1/2}M}\right)^{1/3} \times R_*^{-2/3} N_p^{-1} \times \frac{n_\infty^{1/3} T_\infty^{11/6}}{(Z \ln \Lambda_{in})^{2/3}} \tag{4.8}$$

The expression for the ablation rate G, which is the mass of impurity ablated per unit time, is obtained via the steady-state continuity equation (see, for example, [45]):

$$G = 4\pi M R_p^2 N_p \dot{R}_p \sim \frac{4\pi M}{(\pi e^4)^{2/3}} \left(\frac{\gamma}{m^{1/2}M}\right)^{1/3} \times R_p^{4/3} \times \frac{n_\infty^{1/3} T_\infty^{11/6}}{(Z \ln \Lambda_{in})^{2/3}} \tag{4.9}$$

since $R_* \sim R_p$. Eq. (4.9) is consistent with [46] but also contains a factor of $Z^{-2/3}$ which generalizes the power-law for all atoms beyond hydrogen. More rigorous calculations in [47] determine the coefficient to the scaling law of

Eq. (4.9) for the case of neon.

4.2 Kinetic equation describing plasma electrons streaming through ablation cloud

The scaling law derived in the previous section assumed that electrons could be described by a single thermal velocity. Some of the earliest work, e.g. [48], made the assumption of a mono-energetic population of incident electrons. However, it soon became clear that this would underestimate the ablation rate since electrons in the high-energy tail of the Maxwellian experience fewer collisions in the ablation cloud, and therefore, are most responsible for heating the pellet surface. Models were further improved by recognizing that the distribution of electrons do not remain thermal within the ablation cloud. The cloud contains electrons that are much colder and denser than the ambient background plasma. Hot electrons (which are initially thermal) entering the cloud from the background collide with the cold electrons in the cloud. The electron-electron collisional time scales are much shorter for the cold-cold collisions than for the hot-cold collisions. Because of that, the cold electrons can be viewed as thermalized, but the hot electron distribution function in the cloud can deviate from Maxwellian significantly. Thus, the streaming electrons requires a kinetic description as they slow down and scatter in the ablation cloud. Pre-existing kinetic models (e.g. [46, 49, 50]) are discussed in [47], but the key deviation from the prior works and the one discussed below is this: the gyro-frequency can be comparable to the elastic collision frequency for high-Z scenarios, and thus, both dynamics are retained in the kinetic equation.

For fast electrons, i.e. those with energy greater than 100 eV, the stopping power is $P_s = 4\pi Z e^4 N \ln \Lambda_{in}/mv$[51]. Therefore, the energy deposited per unit volume per unit time by the background plasma in this case is

$$Q = n_\infty \int P_s f \,\mathrm{d}^3 v = \frac{8\pi^2 \times Z N n_\infty e^4 \ln \Lambda_{in}}{m} \int f \,\mathrm{d}v^2 \tag{4.10}$$

where f is the distribution function of the hot electrons within the cloud which is normalized such that $n_\infty \int f \,\mathrm{d}^3 v = 1$. The problem of cloud heating thus reduces to calculating the integral $\int f \,\mathrm{d}v^2$. Eq. (4.10) is consistent with the estimate Eq. (4.6) since $\int f \,\mathrm{d}v^2 \sim \sqrt{m/T_\infty}$.

The kinetic equation for the hot electron distribution function within a neutral cloud of high-Z impurities includes the streaming term and the effects of slowing down due to inelastic collisions with cold electrons, as well as elastic scattering due to collisions with atomic nuclei of density N. Although the ambient plasma cools down, the reservoir of hot electrons is much larger than the number of electrons inside the cloud. As a result, the ambient cooling rate is much slower than the collisional time scales within the cloud, and we therefore, treat the distribution function within the cloud as quasi-stationary. The kinetic equation for the hot electron distribution function is

$$\frac{\partial}{\partial \vec{r}} \cdot \vec{v} f - \frac{1}{v^2}\frac{\partial}{\partial v} v^2 \nu(v) v f + \omega_c \frac{\partial f}{\partial \psi} = \frac{\nu_s(v)}{2\sin\theta}\frac{\partial}{\partial \theta}\sin\theta \frac{\partial f}{\partial \theta} + \frac{\nu_s(v)}{2\sin^2\theta}\frac{\partial^2 f}{\partial \psi^2} \tag{4.11}$$

where θ and ψ are the polar and azimuthal angles in velocity-space, respectively. The incident plasma electrons are considered much hotter than the cloud electrons.

In what follows, we use cylindrical geometry (ρ, φ, z) in coordinate-space, and θ measures from the z-axis. In the limit of large Z, the right-hand-side (RHS) of Eq. (4.11) dominates, and hence, the distribution function is isotropic in velocity-space to lowest order. To that effect, we let $f = F(\vec{r}, v) + \mathcal{O}(Z^{-1})$, where the correction is the anisotropic part of the distribution function. Let $\langle g\rangle \equiv (1/4\pi)\int_0^{2\pi}\int_0^{\pi} g \sin\theta \,\mathrm{d}\theta\,\mathrm{d}\psi$ represent the angular average in velocity-space, and apply it to Eq. (4.11). Terms involving angular derivatives in velocity-space are annihilated, and we are left with a statement that the slowing-down term is balanced by the angular average of the streaming terms, i.e.

$$\begin{aligned}\frac{\partial}{\partial z} v\langle\cos\theta\, f\rangle + \frac{1}{\rho}\frac{\partial}{\partial\rho}\rho\left[v\cos\varphi\langle\sin\theta\cos\psi\, f\rangle + v\sin\varphi\langle\sin\theta\sin\psi\, f\rangle\right]\ldots \\ + \frac{1}{\rho}\frac{\partial}{\partial\varphi}\left[v\sin\varphi\langle\sin\theta\cos\psi\, f\rangle - v\cos\varphi\langle\sin\theta\sin\psi\, f\rangle\right] - \frac{1}{v^2}\frac{\partial}{\partial v}v^3\nu\,\langle f\rangle = 0\end{aligned} \tag{4.12}$$

The moments, e.g. $v\langle\cos\theta\, f\rangle$, are calculated in [47]. The final equation describing the incident electron distribution in the cloud is

$$-\frac{1}{3}\frac{\partial}{\partial z}\frac{1}{\nu_s}v^2\frac{\partial F}{\partial z} - \frac{1}{3}\frac{1}{\rho}\frac{\partial}{\partial\rho}\rho\,\frac{\nu_s}{\omega_c^2+\nu_s^2}v^2\frac{\partial F}{\partial\rho} - \frac{1}{v^2}\frac{\partial}{\partial v}v^3\nu\, F = 0 \tag{4.13}$$

when axial symmetry is considered. The relative strength of the magnetic field determines whether Eq. (4.13) describes diffusion longitudinally (i.e. along z)

or radially (i.e. along $r = \sqrt{z^2 + \rho^2}$).

4.2.1 Heating rate density

An expression for the heating rate density is a matter of solving Eq. (4.13) for the distribution function and using it to integrate Eq. (4.10). In fact, this is what is done in [47] in the limits $\omega_c \gg \nu_s$ (i.e. strong magnetic field limit) and $\omega_c \ll \nu_s$ (i.e. strong scattering limit).

For $\omega_c \gg \nu_s$ and coincidentally $\omega_c \ll \nu_s$ very close to the pellet surface, the mathematical structure of the diffusion is identical. Despite these mathematical similarities, the physical picture is quite different. In the strong field limit, the hot electrons follow the field lines closely en-route to the pellet surface; that is, the gyro-radius is small compared to the pellet radius. Electrons on different field lines encounter different cloud thicknesses and hence heat the pellet surface asymmetrically. As a result, a two-dimensional description of the ablation cloud is required to resolve the flow. In the strong scattering limit, a slab of impurity pellet is continuously heated due to the geometry being approximately one-dimensional near the pellet surface. The normalized heat density for these cases is

$$\int f \,\mathrm{d}v^2 = -\frac{\Gamma(1/4)}{2^{1/4}\pi}\frac{\partial}{\partial\xi}\frac{1}{\xi^{1/2}}\int_0^\infty \mathrm{d}\tau\,\sqrt{\frac{\xi^2}{8\tau}}\exp\!\left(-\frac{\xi^2}{8\tau}\right)K_{1/4}\left(\frac{\xi^2}{8\tau}\right)f_i(\tau) \quad (4.14)$$

where Γ is the Gamma function, $K_\mu(x)$ is the modified Bessel function of the second kind, and

$$\xi \equiv \frac{8\pi Z e^4}{m^2 v_{th}^4} \times (3Z \ln \Lambda_{in} \ln \Lambda_{el})^{1/2} \int_z^\infty N(z')\,\mathrm{d}z' \tag{4.15}$$

is the line-integrated density[5] which is essentially normalized by the collisional cross-section which goes as $(e^2/mv_{th}^2)^2$, and f_i is the distribution function at the plasma-cloud interface[6] expressed in terms of the variable $\tau = (1/8)(v/v_{th})^8$.

For $\omega_c \ll \nu_s$ and far from the pellet surface, we use an approximate expression for the density of a spherically-expanding cloud in order to obtain a solution to Eq. (4.13). Ultimately, the normalized heat density in this case is

$$\int f\,\mathrm{d}v^2 = 2\,\mathrm{Re}\left\{2^{1/2} e^{-15\pi i/16} \int_0^\infty \mathrm{d}z\, z^2 (\xi z^2)^{5/4} H_{5/4}^{(2)}(e^{7\pi i/4}\xi z^2) \int_0^\infty \mathrm{d}\tau\, e^{iz^4\tau} f_i(\tau)\right\} \tag{4.16}$$

where $H^{(2)}(x)$ is the Hankel function of the second kind. The power density in the one-dimensional (strong magnetic field/slab limit) and three-dimensional (spherical) cases are plotted in Fig. 4.1 in the case that f_i is Maxwellian.

4.2.2 Ablation rate for spherically-symmetric expansion

The ablation rate is calculated below in the case that the electron heating is spherically-symmetric. The steady-state fluid equations [53] describing

---

[5] For $\omega_c \ll \nu_s$, the diffusion occurs radially, and hence $z' \to r'$ in the integration.

[6] This is not necessarily Maxwellian. For instance, if the plasma is rapidly cooled, the background distribution may deviate from Maxwellian[52].

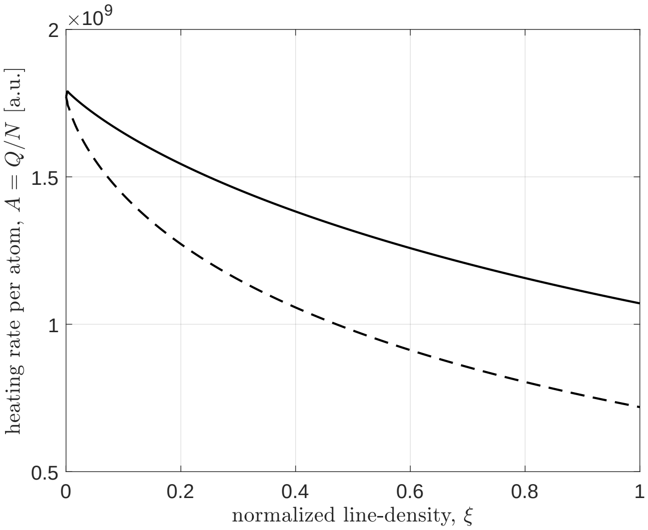

Figure 4.1: Heating rate per atom as a function of normalized line-density where the strong magnetic field/slab model using Eq. (4.14) is shown as a dashed black line, and the spherical model using Eq. (4.16) is shown in solid. Since the shape of the curves are universal, the plot is a comparison of $\int f \, \mathrm{d}v^2$ in the two models.

the radial profile of the ablation cloud are

$$G = 4\pi M R^2 N V = \text{constant} \tag{4.17}$$

$$MNV \frac{\mathrm{d}V}{\mathrm{d}R} + \frac{\mathrm{d}}{\mathrm{d}R} NT = 0 \tag{4.18}$$

$$\frac{G}{4\pi R^2} \frac{\mathrm{d}}{\mathrm{d}R} \left(\frac{\gamma T/M}{\gamma - 1} + \frac{V^2}{2} \right) = NA, \tag{4.19}$$

where N, V, and T are the density, velocity, and temperature, respectively. We make the change of variables to $W = V^2$ and Mach number, $\mu \equiv \gamma T/MV^2$, to obtain

$$N = \frac{G/M}{4\pi R^2 \sqrt{W}} \tag{4.20}$$

$$(\mu^2 - 1)\frac{\mathrm{d}W}{\mathrm{d}R} = \frac{4W}{R}\left[1 - \frac{(\gamma - 1)R\mu^2\, A}{2MW^{3/2}}\right] \tag{4.21}$$

$$(\mu^2 - 1)\frac{\mathrm{d}\mu}{\mathrm{d}R} = \frac{\mu(\gamma\mu^2 + 1)}{R}\left[1 - \frac{(\gamma - 1)R\mu^2\, A}{2MW^{3/2}}\right] - \frac{\mu(\mu^2 - 1)}{R} \tag{4.22}$$

Apparently, W and μ suffer the same type of singularity when the Mach number is equal to unity. However, the profiles must remain continuous throughout the sonic transition. To avoid the singularity, we require that

$$W_* = \left(\frac{\gamma - 1}{2}\frac{R_* A_*}{M}\right)^{2/3} \tag{4.23}$$

Note that this result is consistent with the sonic scaling of Eq. (4.7). The derivatives at $R = R_*$ are evaluated by applying l'Hospital's rule to Eq. (4.21)-(4.22), viz.

$$W'_* = \frac{2W_*}{R_*}\frac{3 - \gamma}{1 + \gamma}\left[1 + \sqrt{1 + \frac{2(1 + \gamma)}{(3 - \gamma)^2}\left(1 - \frac{R_* A'_*}{A_*}\right)}\right] \tag{4.24}$$

$$\mu'_* = \frac{1 - \gamma}{2R_*}\left[1 + \sqrt{1 - \frac{2(1 + \gamma)}{(1 - \gamma)^2}\left(\frac{\gamma - 5}{\gamma + 1} + \frac{R_* A'_*}{A_*}\right)}\right] \tag{4.25}$$

where primes denote differentiation with respect to R, and starred quantities denote values at the sonic point. The ODEs are integrated from the sonic point via shooting procedure in [47] and the ablation rate for neon obtained from those numerical solutions is shown in Fig. 4.2.

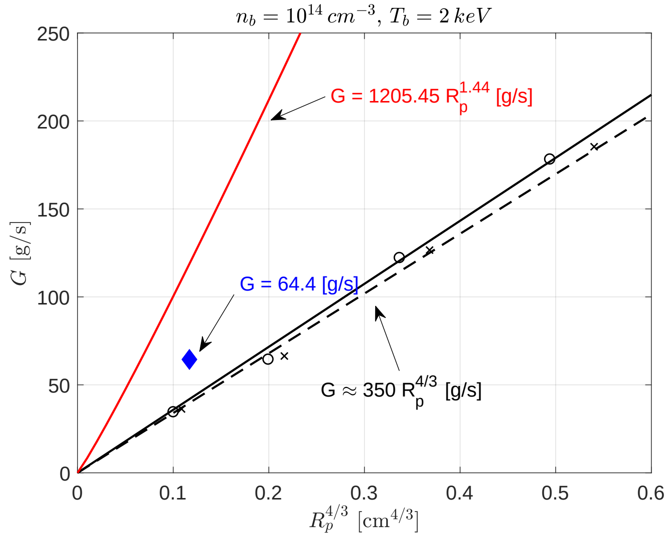

Figure 4.2: Ablation rate (neon) versus pellet radius to the four-thirds power calculated from steady-state fluid equations using Eq. (4.14) for the heating rate (x's and dashed) and Eq. (4.16) for the heating rate (o's and solid). Independent analysis from R. Samulyak and P.B. Parks (private communication) yields $G = 64.4\,g/s$ for a $2\,mm$ neon pellet and is indicated by the ◇ marker. The ablation rate calculated from the model of [50] is shown in the solid red. The background plasma density and temperature are $n_\infty = 10^{14}\,cm^{-3}$ and $T_\infty = 2\,keV$, respectively.

4.3 Expansion of the impurity wake

The previous section considered a pellet at rest, but in reality, the pellet is moving[7]. If the pellet is traveling faster than the expansion velocity of the ablation cloud, then the pellet will exit the cloud and leave behind a wake. This will be the case in a tokamak since the cloud will eventually become ionized and $\vec{J} \times \vec{B}$ forces constrain the motion of the cloud across the toroidal

---

[7] Injection speeds are on the order of $200\,m/s$.

field lines and the pellet velocity is more or less transverse to this field direction.

The wake expansion will be governed by the following ideal gas fluid equations[61] for density, momentum, and energy, respectively:

$$\frac{\partial N}{\partial t} + \boldsymbol{\nabla} \cdot N\vec{V} = 0 \tag{4.26}$$

$$\frac{\partial}{\partial t} MN\vec{V} + \boldsymbol{\nabla} \cdot MN\vec{V}\vec{V} + \boldsymbol{\nabla} p = 0 \tag{4.27}$$

$$\frac{\partial}{\partial t} MN\left(\frac{1}{2}V^2 + \epsilon\right) + \boldsymbol{\nabla} \cdot \left[MN\vec{V}\left(\frac{1}{2}V^2 + h\right)\right] = Q \tag{4.28}$$

where $p = NT$, $h = \epsilon + p/\rho$ is the enthalpy (where $\rho = MN$ is the mass density), ϵ is the internal energy, and Q is the power density injected into the gas. The enthalpy is obtained by recalling the adiabatic relation, $p/\rho^\gamma = const.$ and for an isentropic system, $\mathrm{d}h = \mathrm{d}p/\rho$. Then

$$h = \int \frac{\mathrm{d}p}{\rho} = \int \frac{\mathrm{d}p}{Cp^{1/\gamma}} = \frac{1}{Cp^{1-\gamma/\gamma}} \times \frac{\gamma}{\gamma - 1} = \frac{\gamma}{\gamma - 1}\frac{p}{\rho} = \frac{\gamma T/M}{\gamma - 1} \tag{4.29}$$

The internal energy quickly follows from this result and is that $\epsilon = T/M(\gamma - 1)$.

The fluid equations have been written in conservative form, but combining Eq. (4.26) and Eq. (4.27) yields

$$\frac{\partial \vec{V}}{\partial t} + (\vec{v} \cdot \boldsymbol{\nabla})\vec{v} + \boldsymbol{\nabla}\frac{T}{M} + \frac{T}{M}\boldsymbol{\nabla} \log n = 0 \tag{4.30}$$

Similarly, the energy equation can be combined with the former two equations by first expanding it like so:

$$Q = MN\vec{V} \cdot \frac{\partial \vec{V}}{\partial t} + \frac{1}{2} MV^2 \frac{\partial N}{\partial t} + MN \frac{\partial}{\partial t} \frac{T/M}{\gamma - 1} + \frac{T/M}{\gamma - 1} \frac{\partial MN}{\partial t}$$
$$+ \frac{1}{2} V^2 \boldsymbol{\nabla} \boldsymbol{\cdot} MN\vec{V} + MN\vec{V} \cdot (\vec{V} \cdot \boldsymbol{\nabla})\vec{V} + \frac{\gamma T/M}{\gamma - 1} \boldsymbol{\nabla} \boldsymbol{\cdot} MN\vec{V} + MN\vec{V} \cdot \boldsymbol{\nabla} \frac{\gamma T/M}{\gamma - 1} \tag{4.31}$$

Two of terms above are identically expressed as the following (by adding and subtracting like-terms):

$$\frac{\gamma T/M}{\gamma - 1} \boldsymbol{\nabla} \boldsymbol{\cdot} MN\vec{V} = \frac{T}{M} \left[MN \boldsymbol{\nabla} \boldsymbol{\cdot} \vec{V} + (\vec{V} \cdot \boldsymbol{\nabla}) MN \right] + \frac{T/M}{\gamma - 1} \boldsymbol{\nabla} \boldsymbol{\cdot} MN\vec{V} \tag{4.32}$$

$$MN\vec{V} \cdot \boldsymbol{\nabla} \frac{\gamma T/M}{\gamma - 1} = MN(\vec{V} \cdot \boldsymbol{\nabla}) \frac{T}{M} + MN(\vec{V} \cdot \boldsymbol{\nabla}) \frac{T/M}{\gamma - 1} \tag{4.33}$$

Cancelations leave the following for the energy equation:

$$MN \frac{\partial}{\partial t} \frac{T/M}{\gamma - 1} + NT \boldsymbol{\nabla} \boldsymbol{\cdot} \vec{V} + MN(\vec{V} \cdot \boldsymbol{\nabla}) \frac{T/M}{\gamma - 1} = Q \tag{4.34}$$

Gathering the equations we obtain

$$\frac{\partial N}{\partial t} + \boldsymbol{\nabla} \boldsymbol{\cdot} N\vec{V} = 0 \tag{4.35}$$

$$M \frac{\partial \vec{V}}{\partial t} + M(\vec{V} \cdot \boldsymbol{\nabla})\vec{V} + \boldsymbol{\nabla} T + T \boldsymbol{\nabla} \log n = 0 \tag{4.36}$$

$$\frac{N}{\gamma - 1} \frac{\partial T}{\partial t} + NT \boldsymbol{\nabla} \boldsymbol{\cdot} \vec{V} + \frac{N}{\gamma - 1} (\vec{V} \cdot \boldsymbol{\nabla}) T = Q \tag{4.37}$$

When the heating rate density has the form, $Q = NA$, the energy equation is independent of the cloud density, viz.

$$\frac{1}{\gamma - 1} \frac{\partial T}{\partial t} + T \boldsymbol{\nabla} \boldsymbol{\cdot} \vec{V} + \frac{1}{\gamma - 1} (\vec{V} \cdot \boldsymbol{\nabla}) T = A \tag{4.38}$$

where A is the heating rate per cloud particle which, in this scenario, is provided by the background plasma.

It is convenient to use the following normalizations:

$$t \to t\nu_*,\ r \to \frac{r}{V_*/\nu_*},\ N \to \frac{N}{N_*},\ V \to \frac{V}{\sqrt{\gamma T_*/M}} = \frac{V}{V_*},\ T \to \frac{T}{T_*},\ A \to \frac{A}{\nu_* T_\infty} \tag{4.39}$$

where N_* is a characteristic wake density, T_* is the characteristic temperature, $V_* = \sqrt{\gamma T/M}$ is the associated sound speed, $\nu_* \equiv 4\pi e^4\, N_* \ln\Lambda/m^2 v_{th}^3$ is the characteristic collision frequency with incident electrons of thermal speed, $v_{th} = \sqrt{2T_\infty/m}$, where T_∞ is the background temperature. Hence, the characteristic heating rate is $A_* = \nu_* T_\infty$. The fluid equations then become

$$\frac{\partial N}{\partial t} + \boldsymbol{\nabla}\cdot N\vec{V} = 0 \tag{4.40}$$

$$\frac{\partial \vec{V}}{\partial t} + (\vec{V}\cdot\boldsymbol{\nabla})\vec{V} + \boldsymbol{\nabla} T + T\boldsymbol{\nabla}\log N = 0 \tag{4.41}$$

$$\frac{1}{\gamma-1}\frac{\partial T}{\partial t} + T(\boldsymbol{\nabla}\cdot\vec{V}) + \frac{1}{\gamma-1}(\vec{V}\cdot\boldsymbol{\nabla})T = \frac{T_\infty}{T_*}A \tag{4.42}$$

4.3.1 Self-similar solution of ideal gas equations

We consider one-dimensional expansion; in this case, the expansion is along the field lines and motion across the field is constrained by magnetic pressure. Furthermore, the temperature of the wake is constant, i.e. $\boldsymbol{\nabla} T = 0$, due to the background plasma acting as an infinite reservoir and the assumption of high thermal conductivity.

The solution of the gas equations have the following form:

$$N(r,t) = k(t)^{\delta/2}\exp\bigl[-k(t)r^2\bigr], \quad V(r,t) = \omega(t)r, \quad T(r,t) = T(t) \tag{4.43}$$

where $k(t)$, $\omega(t)$, and $T(t)$ are un-determined functions of time, and $\delta = 1, 2, 3$ characterizes the dimensionality of the fluid expansion. Let $y \equiv \log N$, then

$$\frac{\partial y}{\partial t} = \frac{\delta}{2}\frac{\dot{k}}{k} - \dot{k}r^2 \tag{4.44}$$

$$\frac{\partial y}{\partial r} = -2kr \tag{4.45}$$

and $\boldsymbol{\nabla}\cdot\vec{v} = \delta\,\omega$. The fluid equations then reduces to the following ODEs

$$\delta\dot{k} - 2k\dot{k}r^2 - 4k^2\omega r^2 + 2\delta k\omega = (\dot{k} + 2k\omega)(\delta - 2kr^2) = 0 \Longrightarrow \dot{k} + 2k\,\omega = 0 \tag{4.46}$$

$$\dot{\omega} + \omega^2 - 2k\,T = 0 \tag{4.47}$$

$$\frac{1}{\gamma - 1}\dot{T} + \delta\omega\,T = \frac{T_\infty}{T_*}A \tag{4.48}$$

where $\dot{k} = \mathrm{d}k\,/\,\mathrm{d}t$, for example. In Eq. (4.46), the right parentheses cannot be equal to zero (except for the case that the argument of the exponent in the density profile is constant in time), which means that the left parentheses must vanish.

The function ω was so-named because it has units of frequency, i.e. $\omega \sim 1/t$. Let the power source $A = \textit{constant}$. Dimensional inspection of Eq. (4.48) reveals that the other variables must be $k \sim t^{-3}$ and $T \sim t$. The constants of proportionality are determined by plugging these scalings into the equations Eq. (4.46)-(4.48). The final result is

$$k(t) = \frac{3}{4}\frac{4+3\delta(\gamma-1)}{2(T_\infty/T_*)A\,t^3} \tag{4.49}$$

$$\omega(t) = \frac{3}{2t} \tag{4.50}$$

$$T(t) = \frac{(\gamma-1)(T_\infty/T_*)A\,t}{1+(3/2)\delta(\gamma-1)} \tag{4.51}$$

This simple model was implemented in [60] as a density perturbation to study the impact of pellet injection on global Alfvén eigenmodes (see Fig. 4.3).

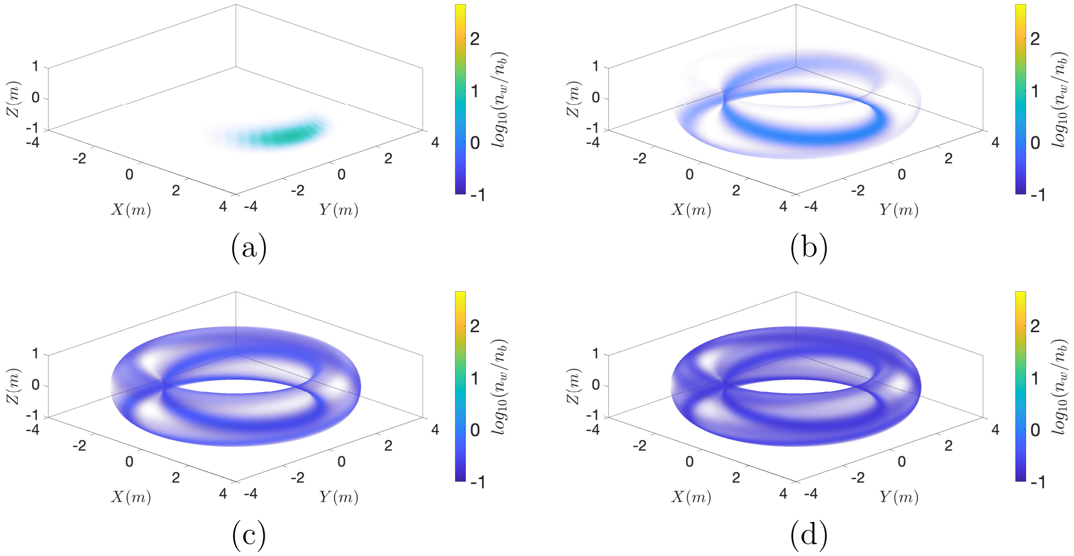

(a)

(b)

(c)

(d)

Figure 4.3: Toroidal expansion of pellet wake: (a) $t = 0.66\,ms$, (b) $t = 5.30\,ms$, (c) $t = 14.58\,ms$, and (d) $t = 25.85\,ms$. Color shows $\log_{10}(N/n_\infty)$, where N is the wake density and $n_\infty = 10^{13}\,cm^{-3}$ is the background equilibrium density; the background temperatures is $T_\infty = 1\,keV$.

Appendices

Appendix A

Included Paper A: Lifetime and universal distribution of runaway electrons

Reproduced from Physics of Plasmas **24** 112509 (2007), with the permission of AIP Publishing

PHYSICS OF PLASMAS **24**, 112509 (2017)

Lifetime and universal distribution of seed runaway electrons

Adrian K. Fontanilla[a] and Boris N. Breizman[b]
Institute for Fusion Studies, University of Texas at Austin, Austin, Texas 78712, USA

(Received 28 August 2017; accepted 18 October 2017; published online 21 November 2017)

The lifetime of pre-existing runaway electrons determines how likely the runaways will undergo avalanche multiplication. We estimate the lifetime of runaway electrons via kinetic analysis. We show that the rate of runaway decay depends on the combination of parameters $\alpha \equiv (Z+1)/\sqrt{\bar{\tau}_{rad}}$ (where $\bar{\tau}_{rad}$ is the synchrotron timescale normalized to the collisional timescale and Z is the ion charge) compared to the electric field. We identify two cases where the decay rate is slow enough to enable a quasi-steady shape of the runaway distribution function. This distribution and its lifetime represent the eigenfunction and the lowest eigenvalue of the kinetic equation. In one case, $\alpha \ll 1$: the field required to sustain the pre-existing runaways is barely larger than the Connor-Hastie critical value. In the same manner as by Aleynikov and Breizman [Phys. Rev. Lett. **114**, 155001 (2015)], we solve the kinetic equation perturbatively but extend the work to demonstrate that the lifetime grows exponentially with the field at a rate that depends on α. In the second case, $\alpha \gg 1$: the sustainment field is much greater than the Connor-Hastie value, and the largeness of the field in this case enables us to universalize the kinetic equation via the re-scaling procedure. *Published by AIP Publishing.* https://doi.org/10.1063/1.5001931

I. INTRODUCTION

In a plasma, runaway occurs when the electric field is strong enough to allow electrons to overcome collisional drag. Electrons that are cooler than the plasma temperature, T_e, experience a drag that increases with momentum, and an electric field exceeding the Dreicer[2] level, $E_D \equiv 4\pi\epsilon_0^2 n_e e^3 \Lambda / T_e$ (where n_e is the electron density, e is the fundamental charge, and Λ is the Coulomb logarithm), is needed to allow all electrons to run away. But when electrons are suprathermal, collisionality with the background plasma decreases (and eventually asymptotes) with particle momentum so that it becomes easier and easier to accelerate electrons. Sufficiently fast electrons—those with energies on the order of their rest mass energy, m_0c^2—experience a nearly constant drag and can be accelerated continuously in an electric field exceeding the Connor-Hastie[3] critical value, $E_C \equiv n_e e^3 \Lambda / 4\pi\epsilon_0^2 m_0 c^2$.

Runaway electrons can become destructive to a tokamak, where energies of a few tens of MeV can be realized, and thereafter be deposited onto the walls of the device. The runaways generated during plasma disruptions[4] pose a serious-enough threat to tokamaks. Of particular concern is an avalanche-type[5] multiplication of the runaway population via knock-on collisions.[6] Machines as large as ITER are especially susceptible to avalanche due to the large currents and long discharge times. Knock-on collisions are expected to be the main mechanism for runaway electron production in ITER but occur at a much slower rate (by a factor of the Coulomb logarithm) compared to small-angle collisions. This disparity between knock-on versus small-angle collisions precipitates a separation of the timescale, which raises the question of how pre-existing runaways equilibrate in phase-space. This sets the stage for the follow-up question of how equilibrated runaways multiply via the avalanche mechanism although we do not address that question in the present paper.

The disruption events typically involve a fast thermal quench and a relatively slow current quench. The latter is likely to be governed by a marginal stability scenario[7] in which the inductive field remains close to the runaway avalanche threshold. This electric field provides a balance between the multiplication of the runaways via knock-on collisions and the diffusive leak of the existing runaway population into the cold core. We explore the regime in which the lifetime of the seed electrons is longer than the thermal quench time but shorter than the current quench time. The first of these two constraints ensures that the seed can be amplified significantly during the thermal quench. The second constraint implies that the avalanche-produced runaways balance the losses of the existing ones in a self-sustained marginal stability scenario of the runaway current decay. For the case of ITER, the timescales for thermal and current quench are envisaged to be on the order of 1 ms and 100 ms, respectively.

A complete theory should determine the threshold field as a function of plasma parameters, thereby determining the rate of magnetic energy dissipation during current quench. Our paper, however, has a more limited goal: to find the lifetime and the spectrum of the existing runaways as a function of the inductive field. This lifetime, or equivalently the decay rate, should then be compared against the runaway multiplication rate in a subsequent work, as demonstrated schematically in Fig. 1. As seen in the figure, the decay rate falls off with the electric field, while the multiplication rate increases with the field. The electric fields considered in our paper should correspond to seed lifetimes which are exponentially long to allow knock-on collisions to be competitive. The intersection in Fig. 1 suggests that this field exceeds the Connor-Hastie value.

---

[a] afontanilla@utexas.edu
[b] breizman@mail.utexas.edu

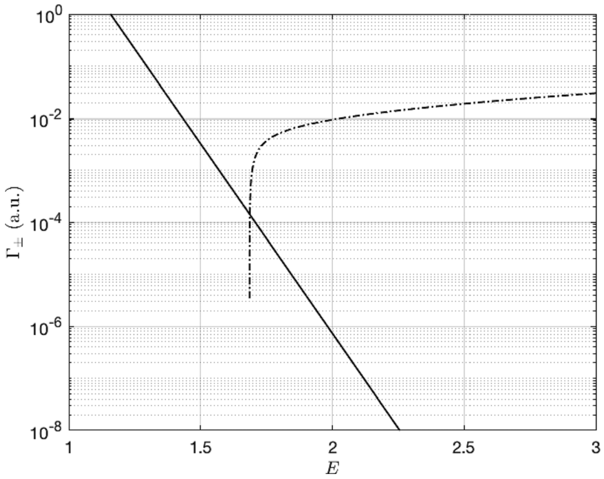

FIG. 1. Schematic plot of the seed runaway decay rate Γ_- (solid) and the knock-on multiplication rate Γ_+ (dash-dotted) versus electric field (normalized to E_C). The intersection of the two curves represents the runaway avalanche threshold.

The relativistic electrons cannot gain momentum indefinitely in this field. Owing to the large magnetic field present in tokamaks, synchrotron drag limits the momentum gain. Martín-Solís *et al.*[8] studied runaways governed by an accelerating electric field, collisional friction, and synchrotron radiative losses using single-particle trajectories and showed that a set of trajectories converged to a stable focus in momentum space. A subsequent kinetic analysis by Aleynikov and Breizman[1] also demonstrated a trend for fast electrons to peak in momentum space. Guo *et al.*[9] emphasized a 2-d treatment and described a vortex structure in momentum space. The cited findings are thematically consistent: their results collectively suggest that there is an accumulation point, or shall we say *attractor*, to which the runaways gather. The location of the attractor in momentum space is determined by the balance of the electric field with collisional and radiative drag. Meanwhile, the angular spread of the attractor is determined by the electric field's ability to collimate the runaways against scattering via collisions of the fast electrons with slow ions and slow electrons.

Although a majority of electrons are concentrated in the vicinity of the attractor (which comprises the main body of the distribution), some electrons populate the wings of the distribution. A description of the wing—particularly the wing that extends towards the thermal bulk—is crucial for determining the lifetime since the electrons in the wing are able to diffuse into a slowing down region of momentum space dominated by collisional friction. The leakage of fast electrons into the slowing down region is promoted by elastic scattering. We will show how the resulting lifetime of the attractor depends on parameters characterizing the elastic scattering, drag, and the electric field strength.

In what follows, re-scaling will be employed to simplify the kinetic equation and identify the dominant dynamical terms. For instance, when the kinetic equation is re-scaled to energies relevant to the attractor, the slowing down effects that lead to runaway decay are de-emphasized. This suggests that fast electrons in the vicinity of the attractor are long-lived. An inspection of the kinetic equation reveals that exponentially long lifetimes can be achieved even at field strengths very close to the Connor-Hastie critical value. In this special case, a one-dimensional description á la[1] enables us to calculate the lifetime as a function of the attractor position and width. When we examine the case of large electric fields compared to E_C, the attractor attains a universal quality in the sense that the re-scaled kinetic equation contains no physical parameters. A strong convective flow around the attractor tends to keep runaways away from the slowing down region in the large field case. Yet, a small number of runaways will invariably bleed into the slowing down region, and thus, the attractor lifetime will be finite.

The rest of this paper is organized as follows: in Sec. II, we introduce the kinetic equation that includes a relativistic collision operator, and in Sec. III, we solve the kinetic equation close to the thermal boundary of momentum space to show why no attractor can be eternal. Next, we survey lifetimes for various parameters using a numerical approach in Sec. IV. The numerical results are supported by analytical findings in Secs. V A and V B that use perturbative methods to calculate the lifetime, and Sec. V C that uses a WKB approximation to calculate the wings of the runaway distribution function.

II. KINETIC EQUATION FOR RUNAWAY ELECTRONS

Our starting point is the kinetic equation for relativistic electrons in a straight and homogeneous magnetic field; the equation includes collisional and radiative drag counter to a constant electric field

$$\frac{\partial F}{\partial s}+\frac{\partial}{\partial p}\left[\left(E\cos\theta-\frac{1+p^2}{p^2}-\frac{1}{\bar{\tau}_{rad}}p\sqrt{1+p^2}\sin^2\theta\right)F\right]
=\frac{1}{p\sin\theta}\frac{\partial}{\partial\theta}\left[\sin\theta\left(E\sin\theta F+\frac{1}{\bar{\tau}_{rad}}\frac{p\sin\theta\cos\theta}{\sqrt{1+p^2}}F+\frac{Z+1}{2}\frac{\sqrt{1+p^2}}{p}\frac{1}{p}\frac{\partial F}{\partial\theta}\right)\right]. \quad (1)$$

This paper utilizes the same notations as Ref. 1. Then, the distribution function is normalized according to $\int F\,\sin\theta\,dp d\theta=1$, where p is the relativistic momentum (normalized to units of m_0c) and θ is the pitch angle relative to the magnetic field axis. The time, s, is normalized to units of the collisional timescale, $\tau\equiv(n_e e^4\Lambda/4\pi\epsilon_0^2 m_0^2 c^3)^{-1}$, and $\bar{\tau}_{rad}\equiv\tau_s/\tau$ is the ratio of the synchrotron timescale, $\tau_s\equiv(e^4B^2/6\pi\epsilon_0 m_0^3c^3)^{-1}$, to the collisional timescale. Typically, $\bar{\tau}_{rad}\sim 100$ for ITER-like parameters. Because of this, we henceforward ignore the shrinking of the pitch angle caused by synchrotron radiation, i.e., the second term on the third line of Eq. (1). The electric field, E, is normalized to units of E_C. The ion charge is Z. The form of Eq. (1) implies that the field accelerates pre-existing runaways and does not generate new ones via the Dreicer mechanism. The linear form of the collision operator is a consequence of the runaways being a minority in the plasma. The collision operator describes only small-angle collisions between fast electrons and cold electrons and ions. The disparity between knock-on collisions and small-angle collisions (which is roughly in the amount of Coulomb logarithm) allows us to omit the avalanche source from Eq. (1). Since there is no source term, any change in the particle number is due to a flux through the boundaries of the momentum space domain.

We will hereafter re-cast Eq. (1) in the form of an eigenvalue equation, that is, letting $\partial F/\partial s \rightarrow -\Gamma_\ell F$. This is appropriate when we examine the long-term evolution of runaway electrons. The long-term profile of F is the eigenfunction, and the corresponding eigenvalue is the runaway electron decay rate (or inverse lifetime). Under certain conditions—and we will show this—Γ_ℓ can be very nearly zero, which enables F to be approximated by a stationary solution.

III. ARGUMENT FOR THE FINITE LIFETIME

In this section, we demonstrate that the rate of runaway decay, Γ_ℓ, must be nonzero. Particle trajectories (in the absence of diffusion) are obtained from Eq. (1) and plotted in Fig. 2. Depicted in the figure is an apparent separatrix and is consistent with the findings of Ref. 9. In this section, we focus on the low-momentum side of the separatrix where particles lose momentum and eventually thermalize due to the dominance of collisional drag and scattering there. The distribution function is, to lowest-order, isotropic in this region, i.e., $\partial F^{(0)}/\partial\theta = 0$. Because synchrotron radiation is ignorable at low momentum, the electric field is the only force that depends on the pitch angle and therefore accounts for any distortion in isotropy. By balancing the electric field term against the scattering term in Eq. (1), the anisotropic correction to the distribution function at low momentum is found to be

$$F^{(1)} = -\frac{E}{Z+1} p^3 \frac{\partial F^{(0)}}{\partial p} \cos\theta. \tag{2}$$

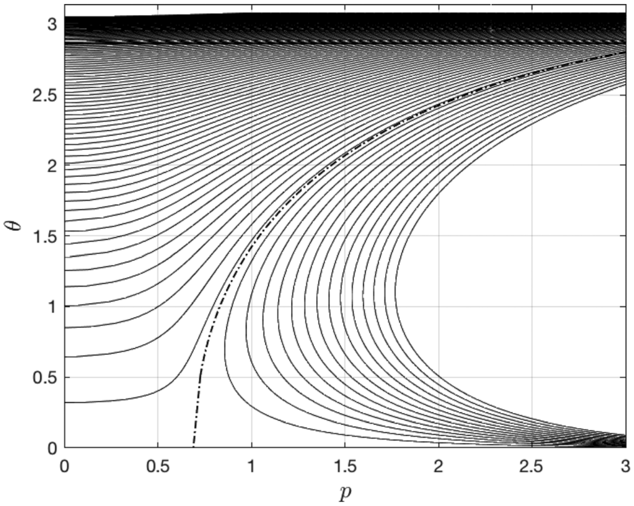

FIG. 2. Convective trajectories in the slowing down region of momentum space depict a separatrix (sketched as a dash-dotted line); on one side of the separatrix, particles inevitably return to the bulk, while on the other, particles gain momentum. For the trajectories shown, $E = 3.1$, $\bar{\tau}_{rad} = 100$, and $Z = 5$.

We essentially reproduce calculations used in Ref. 5 but for the case of a straight magnetic field. We integrate in the pitch angle to annihilate the RHS of Eq. (1) and get

$$\frac{\partial F^{(0)}}{\partial s} - \frac{\partial}{\partial p}\left[\frac{1}{p^2}F^{(0)} + \frac{E^2}{3(Z+1)}p^3\frac{\partial F^{(0)}}{\partial p}\right] = 0. \tag{3}$$

The first term in the equation describes the slowing down due to friction, while the second term describes momentum spreading due to heating by the electric field. We determine if a dynamical balance of these two effects prevents the electrons from thermalizing. To do so, we solve for the zero-flux condition of Eq. (3). The zero-flux solution

$$F^{(0)} = \exp\left[\frac{3(Z+1)}{4E^2}\frac{1}{p^4}\right], \tag{4}$$

requires a divergent number of runaways to be gathered near $p = 0$, which would prevent them from accumulating at large momentum. We must therefore reject the zero-flux boundary condition in favor of an open boundary. From this, we conclude that the number of fast electrons is decreasing. Moreover, there is a mechanism that allows the fast electrons to cross the separatrix into the slowing down region. In what follows, we seek to determine the rate of decay while also characterizing the path of those slowing electrons through momentum space.

IV. NUMERICAL STUDIES

Given that fast electrons are afforded a finite lifetime, we now survey the conditions that would allow the runaway population to survive long enough to be amenable to avalanche multiplication. We solve Eq. (1) for various combinations of the parameters E, $\bar{\tau}_{rad}$, and Z assuming an initial population of runaways via finite volume methods. The momentum p extends from a very small value near zero to a sufficiently large value; very small means we have accounted for the slowing down region, while sufficiently large means that no electrons pass through the boundary that extends towards infinity. However, particles are allowed to pass through the boundary near $p = 0$; in this way, the change in the particle number truly corresponds to the decay rate owed to re-thermalization of fast electrons. The distribution function is seen to relax to a universal shape whose amplitude decreases with time. This observation enables us to later treat Eq. (1) as an eigenvalue problem when we solve it analytically.

The results of the survey are shown in Fig. 3; they indicate that the lifetime, τ_ℓ, grows exponentially with the electric field. The rate of exponential increase in the lifetime is shown to depend on Z and $\bar{\tau}_{rad}$ in the following combination:

$$\alpha \equiv \frac{Z+1}{\sqrt{\bar{\tau}_{rad}}}. \tag{5}$$

Particles last longer for smaller values of α, e.g., the lifetime (measured in units of τ) is $\mathcal{O}(10^6)$ for $E = 2$ and $\alpha = 0.3$, while it is more than three orders of magnitude smaller for the same electric field but $\alpha = 0.8$. An example of the long-

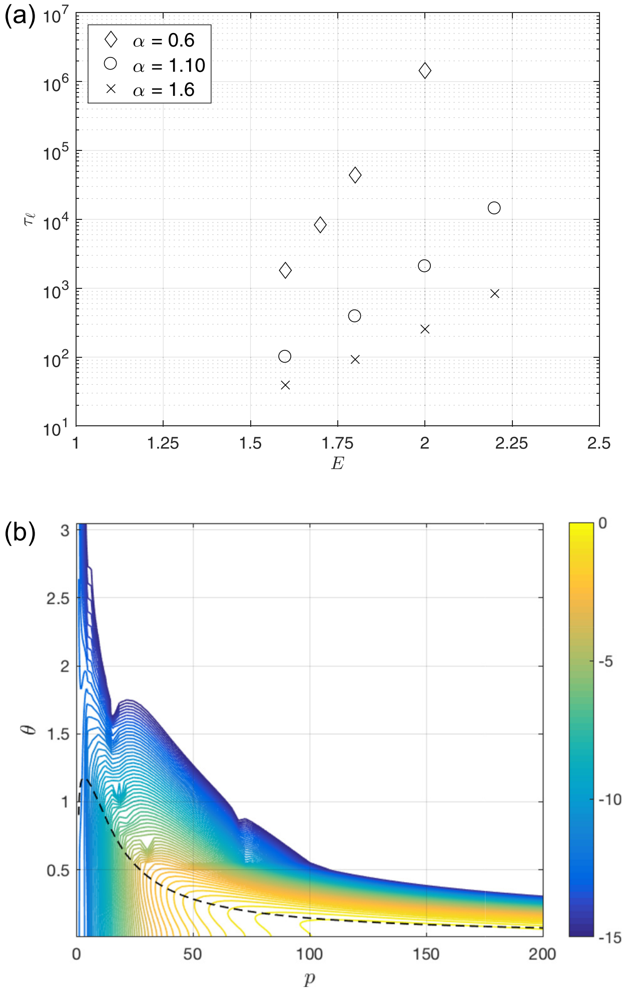

FIG. 3. (a) Lifetime of the runaway seed (log scale) versus electric field, as inferred from numerical solutions of Eq. (1) for various values of the parameter $\alpha \equiv (Z+1)/\sqrt{\bar{\tau}_{rad}}$. Time units are normalized to the Coulomb scattering time, τ. (b) The distribution function, $\log_{10}[(1/p^2)F]$, for $E = 3.1$, $\bar{\tau}_{rad} = 100$, and $Z = 5$.

term distribution function is shown in Fig. 3(b); the main body of the distribution is indicated by the yellow contours, while the low-momentum wing is mostly blue. In accordance with Sec. III, isotropy is enhanced further into the wing.

V. DESCRIPTION OF THE ATTRACTOR

The attractor is a structure in phase-space formed as a result of the dynamical balance between the electric and drag forces and also between pitch angle shrinking and pitch angle scattering. To characterize the attractor, we re-scale Eq. (1) by

$$p = \frac{(E-1)E\sqrt{\bar{\tau}_{rad}}}{\alpha}P, \quad \theta^2 = \frac{\alpha^2}{(E-1)E^2}\Theta^2,$$
$$s = \frac{(E-1)\sqrt{\bar{\tau}_{rad}}}{\alpha}S. \tag{6}$$

For the remainder of this paper, we use capitalized notations to represent scaled quantities. Since we are generally concerned with large values of $\bar{\tau}_{rad}$, the scaling of p reflects the fact that the dynamical balance is only achievable at ultra-relativistic energies. This allows us to neglect terms $\mathcal{O}(p^{-2})$ compared to unity in Eq. (1). As a result of this simplification and re-scaling, we get

$$\frac{\partial F}{\partial S} + \frac{1}{E}\frac{\partial}{\partial P}\left[E\cos\left(\frac{\alpha}{\sqrt{E-1}E}\Theta\right) - 1 - \frac{(E-1)^2E^2}{\alpha^2}P^2\sin^2\left(\frac{\alpha}{\sqrt{E-1}E}\Theta\right)\right]F$$
$$= \frac{1}{P\sin\left(\frac{\alpha}{\sqrt{E-1}E}\Theta\right)\frac{\alpha}{\sqrt{E-1}E}}\frac{\partial}{\partial\Theta}\sin\left(\frac{\alpha}{\sqrt{E-1}E}\Theta\right)$$
$$\times\left[\sin\left(\frac{\alpha}{\sqrt{E-1}E}\Theta\right)F + \frac{\alpha}{\sqrt{E-1}E}\frac{1}{2P}\frac{\partial F}{\partial\Theta}\right]. \tag{7}$$

The equation is herein reduced to a form that depends only on the parameters E and α. Our goal is to explore how the relation between these parameters affects the attractor lifetime. We will thereby extend the analysis presented in Ref. 1. We recall that Ref. 1 specifies the so-called *threshold field for sustainment* (of fast electrons) as

$$E_0 \approx 1 + \frac{\alpha}{\left(\frac{1}{8}+\alpha^2\right)^{1/6}}. \tag{8}$$

This is the minimum field (which exceeds the Connor-Hastie critical value) that must be applied to ensure a long-lived population of fast electrons. This demonstrates the contention between α and E with regard to the longevity of the runaways observed in Sec. IV. In the limiting cases of very small and very large scattering parameters, the threshold field approximates to

$$E_0 \approx \begin{cases} 1 + 2^{1/2}\alpha, & \alpha \ll 1 \\ \alpha^{2/3}, & \alpha \gg 1 \end{cases}. \tag{9}$$

We constrain the scope of this paper to these two cases. In the case of $\alpha \ll 1$, an electric field very close to the Connor-Hastie value, i.e., $E - 1 = \mathcal{O}(\alpha)$, is sufficient to sustain the fast electrons; in the case of $\alpha \gg 1$, $E \gg 1$ is necessary for sustainment. Thus, the case of the small scattering parameter implies that the pitch angle of long-lived runaways scales as $\theta^2 \sim \alpha$, while the large scattering parameter case implies that $\theta^2 \sim \alpha^2/E^3$, and in both cases, the runaways in the vicinity of the attractor occupy a narrow region in momentum space. This enables us to apply the small-angle approximation to Eq. (7), viz.,

$$\frac{\partial F}{\partial S} + \frac{E-1}{E}\frac{\partial}{\partial P}\left[\left(1 - \frac{\alpha^2}{(E-1)^2E^2}\Theta^2 - P^2\Theta^2\right)F\right]$$
$$= \frac{1}{P\Theta}\frac{\partial}{\partial\Theta}\left[\Theta\left(\Theta F + \frac{1}{2P}\frac{\partial F}{\partial\Theta}\right)\right]. \tag{10}$$

The term associated with the deceleration of large pitch angle runaways, i.e., the quadratic term in the cosine expansion, $E\cos\theta = E[1-(1/2)\theta^2+\cdots]$, is small near the attractor as evidenced by the appearance of the combination of parameters, $\alpha^2/(E-1)^2E^2$. Although the deceleration term is small, we keep it because it (along with the pitch angle scattering term) is essential for deducing the lifetime of the attractor when $E-1=\mathcal{O}(\alpha)$. But when $E\gg 1$, we neglect this term and treat the attractor as infinitely long-lived.

We examine the cases of $\alpha\ll 1$ and $\alpha\gg 1$ in their own respective sections below. The former of these cases benefits from being a continuation in some ways of the kinetic theory developed in Ref. 1; the latter benefits from the feature of the kinetic equation being entirely parameter-less.

A. Quasi-stationary distribution for $\alpha\ll 1$

In the limit $\alpha\ll 1$, we can restrict our considerations to $E-1=\mathcal{O}(\alpha)$ which allows us to treat the LHS of Eq. (10) perturbatively. This is the strategy employed in Ref. 1 to describe the attractor, but we expand upon it so that we may properly calculate the lifetime. Using the variable $\eta\equiv P\Theta^2$, rather than Θ, Eq. (10) is written as

$$\frac{P}{2}\left\{\frac{\partial F}{\partial S}+\frac{E-1}{E}\left[\frac{\partial}{\partial P}+\frac{\eta}{P}\frac{\partial}{\partial\eta}\right]\left[1-\left(\frac{\mathcal{E}^2}{4P}+P\right)\eta\right]F\right\}$$
$$=\frac{\partial}{\partial\eta}\left[\eta\left(F+\frac{\partial F}{\partial\eta}\right)\right]. \tag{11}$$

We have written the deceleration by the electric field in terms of the threshold field by means of $\mathcal{E}\equiv(E_0-1)/(E-1)$. The smallness of the deceleration term in the vicinity of the attractor is duly noted when we consider fields $E\gtrsim E_0$. The LHS, which we designate as $\mathcal{Q}$, is small as long as $E-1=\mathcal{O}(\alpha)$ and the decay rate is slow. Therefore, the pitch angle distribution equilibrates on a much faster timescale than the momentum distribution. Neglecting the LHS, the distribution function to the lowest order is

$$F^{(0)}=\Phi(P,S)e^{-\eta}, \tag{12}$$

where Φ is an arbitrary function of P and S when $\mathcal{Q}$ is formally zero but is fully determined when $\mathcal{Q}$ is finite. We thus make $\mathcal{Q}$ finite by including it as an inhomogeneous term in Eq. (11). Next, we integrate twice in η to find

$$F=e^{-\eta}\left[\Phi(P,S)+\int_0^{\eta}\frac{e^{\eta'}\,d\eta'}{\eta'}\int_0^{\eta'}\mathcal{Q}\,d\eta''\right]. \tag{13}$$

The second term in the square brackets represents a small correction to Eq. (12), and thus, the pitch angle dependence of F is mostly isolated to the exponential term. The equation that determines Φ is found by integrating Eq. (11) over the η-variable. This annihilates the RHS and yields

$$\frac{\partial}{\partial S}\int_0^{\infty}d\eta\,F+\frac{E-1}{E}P\frac{\partial}{\partial P}\frac{1}{P}\left\{\left[1-\left(\frac{\mathcal{E}^2}{4P}+P\right)\right]\int_0^{\infty}d\eta\,F\right.$$
$$\left.-\left(\frac{\mathcal{E}^2}{4P}+P\right)\times\int_0^{\infty}d\eta\,(\eta-1)F\right\}=0. \tag{14}$$

The lowest-order term of Eq. (13) is sufficient to calculate the zeroth-order moment, $\int_0^{\infty}F\,d\eta$, appearing above. This is because the coefficient in front of that moment is small in the vicinity of the attractor. The balance of the electric field and drag forces implies that $1-\mathcal{E}^2/4P+P\approx 0$. Thus, we approximate the zeroth-order moment by $\int_0^{\infty}F\,d\eta\approx\Phi$ in the first line of Eq. (14) since the correction is doubly small. Identical terms are added and subtracted to cause the first-order moment $\int(\eta-1)F\,d\eta$ to appear in the second line of Eq. (14). In this case, the correction in Eq. (13) is necessary to evaluate the moment since $\int_0^{\infty}(\eta-1)e^{-\eta}\,d\eta=0$. Using Eq. (13) to evaluate the first-order moment by repeated use of integration-by-parts yields

$$\int_0^{\infty}(\eta-1)F\,d\eta=-\int_0^{\infty}\eta\,\mathcal{Q}\,d\eta$$
$$\approx-\frac{E-1}{2E}P^3\frac{\partial}{\partial P}\frac{1}{P^2}\left\{\left[1-2\left(\frac{\mathcal{E}^2}{4P}+P\right)\right]\Phi\right\}. \tag{15}$$

The first-order moment Eq. (15) consists of terms proportional to Φ and terms proportional to $\partial\Phi/\partial p$. The former are ignored since they represent a small correction to the first line of Eq. (14), but the latter are retained since they prevent the distribution from the shrinking to infinitesimal width. This term extends the work presented in Ref. 1 and makes it possible to calculate the width and the lifetime of the attractor. When we insert the diffusive contribution of the first-order moment into Eq. (14), we obtain

$$\frac{E}{E-1}\frac{\partial\Phi}{\partial S}+P\frac{\partial}{\partial P}\frac{1}{P}\left\{1-\left(\frac{\mathcal{E}^2}{4P}+P\right)\right\}\Phi$$
$$=P\frac{\partial}{\partial P}\left\{\frac{E-1}{2E}\left(\frac{\mathcal{E}^2}{4P}+P\right)\times\left[2\left(\frac{\mathcal{E}^2}{4P}+P\right)-1\right]\frac{\partial\Phi}{\partial P}\right\}. \tag{16}$$

Recalling that, in the vicinity of the attractor, $\mathcal{E}^2/4P+P\approx 1$, the diffusion coefficient in Eq. (16) remains positive and $\mathcal{O}(\alpha)$ throughout the domain of the momentum space as long as the electric field is not too far above threshold. We elaborate on what is meant by "too far" later in Sec. V B. The second term on the first line of Eq. (16) describes the convective flow into the attractor. The zeroes of the convective flow profile are

$$P_{max,min}=\frac{1}{2}\left\{1\pm\sqrt{1-\mathcal{E}^2}\right\}. \tag{17}$$

These notations are analogous to those used in Ref. 1. Hence, the pair of zeroes corresponds to equilibrium points in momentum space with P_{max} being stable and P_{min} unstable. Fast electrons with initial momentum $P>P_{min}$ tend to accumulate at P_{max}; conversely, electrons with initial momentum $P<P_{min}$ inevitably return to the thermal bulk. We thus identify P_{max} as the attractor in this description, while P_{min} marks the transition into the slowing down region of momentum space. Consequently, the appropriate boundary condition for Eq. (16) is $\Phi(P=P_{min},S)=0$. The separation between the equilibrium points is

$$P_s \equiv P_{max} - P_{min} = \sqrt{1-\mathcal{E}^2}. \tag{18}$$

A population of fast electrons described by Eq. (16) is long-lived if the separation P_s is large compared to the width of the main body of the distribution. In order to find the width of the main body centered at P_{max}, we solve Eq. (16) in the vicinity of P_{max} with the new variable $\delta P \equiv P - P_{max}$ thus being small. The reduced equation

$$\frac{E}{E-1}\frac{\partial \Phi}{\partial S} + \frac{\partial}{\partial \delta P}\left[-\frac{4P_s}{(1+P_s)^2}\delta P\,\Phi\right] = \frac{\partial}{\partial \delta P}\left[\frac{E-1}{2E}\frac{\partial \Phi}{\partial \delta P}\right], \tag{19}$$

describes a distribution function that relaxes to a gaussian

$$\Phi^{(0)}(P) = \exp\left[-\frac{1}{2}\left(\frac{P-P_{max}}{\Delta}\right)^2\right], \tag{20}$$

with width

$$\Delta^2 = \frac{E-1}{8E}\frac{(1+P_s)^2}{P_s}. \tag{21}$$

The superscript on $\Phi^{(0)}$ denotes that the gaussian description corresponds to the eigenvalue $\Gamma_\ell = 0$. The gaussian has a small but finite number of particles at P_{min} because it is a zero-flux solution. In Sec. V B, we append the gaussian description in order to enforce the vanishing boundary condition at P_{min}, which will yield a small nonzero value of Γ_ℓ.

B. Attractor lifetime for $\alpha \ll 1$

Treating the temporal term in Eq. (19) as a perturbation, we let $\partial\Phi/\partial S \to -\Gamma_\ell \Phi^{(0)}$ with $\Gamma_\ell \neq 0$. When the upper limit of integration is chosen to be at infinity (where the flux is zero), the solution of the eigenequation yields the second term as below

$$\Phi(P) = \Phi^{(0)}\left[1 - 2\Gamma_\ell\left(\frac{E}{E-1}\right)^2 \int_P^\infty \frac{\mathrm{d}P'}{\Phi^{(0)}}\int_{P'}^\infty \Phi^{(0)}\,\mathrm{d}P''\right], \tag{22}$$

which is the nonzero-flux correction. The decay rate, Γ_ℓ, is determined by applying a vanishing boundary condition at $P = P_{min}$

$$0 = 1 - 2\Gamma_\ell\left(\frac{E}{E-1}\right)^2 \int_{P_{min}}^\infty \mathrm{d}P''\,\Phi^{(0)} \int_{P_{min}}^{P''} \frac{\mathrm{d}P'}{\Phi^{(0)}}. \tag{23}$$

Note that the order of integration is switched in Eq. (23). Upon permuting the order, the integrand of the inner integral is dominated by the regions where $\Phi^{(0)}$ nearly vanishes, i.e., near the boundaries. For this reason, we regard the inner integral independent of the variable P'' and treat the nested integrals in Eq. (23) as products of integrals. That being said, we must be careful in our choice of the limit P''. It must be chosen to lie in the region where $(\Phi^{(0)})^{-1}$ is relatively flat, i.e., both far from the boundary and the main body of the attractor, in order to ensure that the inner integral is approximately constant.

Equation (23) is solved for the lifetime

$$\tau_\ell = 2\left(\frac{E}{E-1}\right)^2 \int_{P_{min}}^\infty \Phi^{(0)}\mathrm{d}P' \times \int_{P_{min}}^{P''} \frac{\mathrm{d}P'}{\Phi^{(0)}}. \tag{24}$$

The first integral is proportional to $\mathrm{erfi}[(1/\sqrt{2})(P_s/\Delta)]$, which can make the lifetime exponentially long depending on the ratio of the separation, P_s, to the width of the distribution, Δ. This ratio reflects the competition between the flow of the runaways into the attractor and their diffusion into the slowing down region. What we find from that competition is shown in Fig. 4. The plot shows an initial trend for the lifetime to increase exponentially with the electric field (even at field values very close to the Connor-Hastie value) where the rate of exponential increase depends on α. This is consistent with our numerical simulations (Fig. 3). Physical intuition suggests that the lifetime will increase with the electric field indefinitely, and therefore, the rollover in Fig. 4 is merely an indication of where the presented perturbation technique breaks down. In particular, there appear to be lower and upper bounds to the electric field.

Given Eq. (9), the electric field must at least be as large as the threshold field, E_0 – larger, in fact, when we consider that the separation between P_{min} and P_{max} is given by Eq. (18). When $E = E_0 \iff \mathcal{E} = 0$, the separation between the equilibrium points is zero and no accumulation of fast electrons is possible. Furthermore, the main body of the distribution should be located sufficiently far from P_{min} to ensure that the accumulation of fast electrons at P_{max} is more likely to occur than their depletion at P_{min}. We state this criterion succinctly as $\Delta^2/P_s^2 \ll 1$. We approximate Δ and P_s by their values when $E \simeq E_0 \simeq 1$

$$\Delta \approx \sqrt{\frac{E_0-1}{2}\frac{1}{P_s}}, \quad P_s \approx \sqrt{2\frac{E-E_0}{E_0-1}}, \tag{25}$$

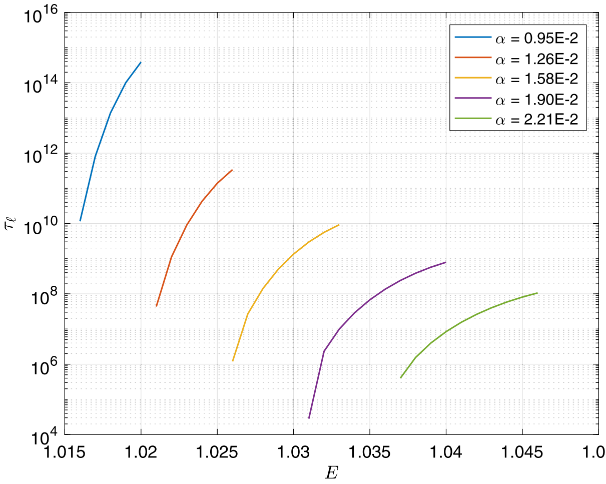

FIG. 4. Lifetime of the runaway seed (log scale) versus electric field, as determined by Eq. (24) for various values of α. The rollover on each curve indicates that the electric field is approaching the applicability limit of Eq. (24). The units of time are normalized to τ.

and insert them into the aforementioned criterion. When we use Eq. (9) to approximate the difference $E_0 - 1$, the criterion yields the following lower bound on the electric field:

$$E - E_0 \gg 2^{-5/6}\alpha^{5/3}. \tag{26}$$

The upper bound is determined by validating one key assumption of the procedure: the LHS of Eq. (11) is perturbatively small throughout the entire domain of momentum space, i.e., $\mathcal{Q} \ll F\,\forall P$. In order to determine where our assumption fails, we evaluate $\mathcal{Q}$ at its largest. The gaussian approximation Eq. (20) suggests that this term will be largest in the wings of the distribution where the P-derivative of F is steepest. Where $\mathcal{Q}$ is largest, we estimate it as

$$\mathcal{Q} \approx \left[1 - \left(\frac{\mathcal{E}^2}{4P} + P\right)\eta\right] P\frac{\partial F}{\partial p}. \tag{27}$$

An estimate for the term $P\,\partial F/\partial P$ comes from balancing the fluxes in Eq. (16). The magnitude for the perturbative term is approximately

$$\mathcal{Q} \approx \left[1 - \left(\frac{\mathcal{E}^2}{4P} + P\right)\eta\right] \frac{1 - \left(\mathcal{E}^2/4P + P\right)}{\left(\frac{\mathcal{E}^2}{4P} + P\right)\left[2\left(\frac{\mathcal{E}^2}{4P} + P\right) - 1\right]} F^{(0)}. \tag{28}$$

We see that for large enough fields, i.e., $E - E_0 \geq E_0 - 1 = \sqrt{2}\alpha$, the denominator of $\mathcal{Q}$ will contain zeroes at $P = (1/4)\left(1 \pm \sqrt{1 - 4\mathcal{E}^2}\right) \leq 1/2$, making the perturbative term singular. Thus, the electric field cannot be too far above threshold. The window of applicability for the analysis in the case of $\alpha \ll 1$ is in the close vicinity of the threshold field (and by extension, the Connor-Hastie field), viz.,

$$2^{-5/6}\alpha^{5/3} \ll E - E_0 < 2^{1/2}\alpha. \tag{29}$$

C. Wing of the attractor for $\alpha \gg 1$

In the limit $\alpha \gg 1$, a large electric field (much greater than unity) must be applied to confine the fast electrons to the attractor described by Eq. (10). In this limiting case, all physical parameters vanish from Eq. (10), viz.,

$$\frac{\partial F}{\partial S} + \frac{\partial}{\partial P}\left[\left(1 - P^2\Theta^2\right)F\right] = \frac{1}{P\Theta}\frac{\partial}{\partial\Theta}\left[\Theta\left(\Theta F + \frac{1}{2P}\frac{\partial F}{\partial\Theta}\right)\right], \tag{30}$$

and all quantities are generally $\mathcal{O}(1)$, including the decay rate. For an $\mathcal{O}(1)$ decay rate, the scaling for the time variable Eq. (6) yields a lifetime that grows linearly with the electric field. In contrast to this initial thought, the lowest eigenvalue of Eq. (30) is, in fact, zero, and as a result, the lifetime rather increases exponentially with the electric field. Consequently, we pursue a time-independent solution of Eq. (30), which explains how the longevity of the attractor goes hand-in-hand with a steep decay in the particle number at small values of P in momentum space.

There is an intermediate region of momentum space between the slowing down region and the attractor where the pitch angle diffusion is small. Particles in this region will not stray far from the convective trajectories, and so, we render those trajectories in Fig. 5. Using the change-of-variables P and $Q \equiv 1/P^2\Theta^2$, Eq. (10) transforms to

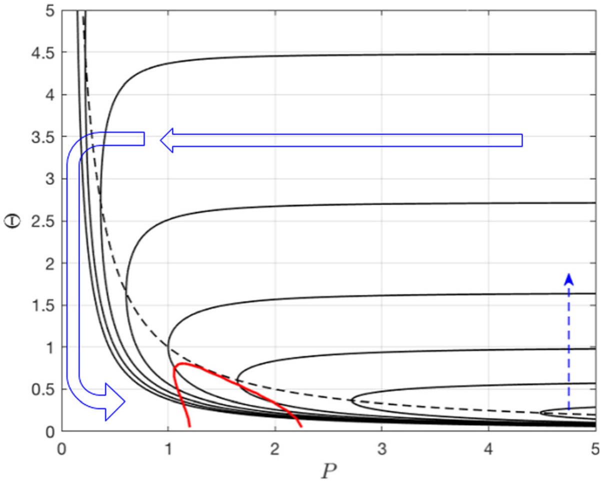

FIG. 5. Convective trajectories (solid) are characterized by values of $Q - \log Q - \log P^2$ and experience a turning point (dashed) along $Q = 1$. Orbits above the turning point are populated by faster particles (i.e. $P > 1$) that have diffused in the pitch angle (e.g. dashed blue). Particles arrive at the low momentum region via trajectories with a sufficiently large pitch angle. The schematic position of the attractor in phase-space is indicated in red. The blue block arrows sketch a band outside the attractor where diffusion is weak compared to convection.

$$\frac{\partial F}{\partial S} + \frac{Q-1}{Q}\frac{\partial F}{\partial P} + \frac{2}{P}\frac{\partial F}{\partial Q} + \frac{2}{P}\frac{Q-1}{Q}F = 2Q^2\frac{\partial}{\partial Q}Q\frac{\partial F}{\partial Q}. \tag{31}$$

From the characteristic equations, we find that the trajectories are determined by the constant-of-motion

$$Q - \log Q - \log P^2 = constant. \tag{32}$$

The runaways described by Eq. (30) do not sufficiently slow down to thermalize, and instead, each trajectory experiences a turning point along the contour $1 - P^2\Theta^2 = 0$, i.e., $Q = 1$. This contour marks where the electric field balances the drag. The trajectories shown in Fig. 5 do not close at $P \rightarrow \infty$, which would cause any population of particles to accumulate at infinite energies and infinitesimally small pitch angles. However, pitch angle scattering of the fast electrons will ultimately limit the momentum gain since particles that have diffused onto orbits above the turning point in Θ slow down due to the synchrotron radiation there. We thus have the following picture for the circulation of fast particles about the attractor: an accelerating current of particles is maintained by the electric field, and a decelerating current is maintained by synchrotron drag. Pitch angle scattering enables particles to travel from the accelerating current to the decelerating one at $P \gg 1$, while pitch angle shrinking by the electric field enables the opposite transition at smaller P. In this way, the particle orbits are effectively closed and enable a stationary solution of Eq. (30).

Runaways that arrive at the near-thermal region of momentum space originate, remarkably, from the ultra-relativistic region of momentum space (see Fig. 5). An asymptotic expression for the distribution function in the ultra-relativistic tail[10] is given by

$$F = \exp\left(-2P - P^2\Theta^2\right). \tag{33}$$

This expression exhibits the expected exponential decay in the pitch angle, but its applicability fails when $P^2\Theta^2 \gtrsim P$. The way to relax this constraint is to estimate the likelihood to populate the counter-streaming trajectories by comparing the radiation term against the scattering term in Eq. (30), viz.,

$$-\frac{\partial}{\partial P}P^2\theta^2 F \sim \frac{1}{P\Theta}\frac{\partial}{\partial \Theta}\Theta\,\frac{1}{2P}\frac{\partial F}{\partial \Theta}. \tag{34}$$

The equation is reduced to an ordinary differential equation (ODE) by means of the similarity variable $P^4\Theta^4/P$ and re-normalization of F by P^2; the solution to the resulting ODE

$$\lim_{P^2\Theta^2\to\infty} F = \frac{1}{P^2}\int_{\frac{3P^4\Theta^4}{8P}}^{\infty}\frac{e^{-z}}{z}\mathrm{d}z, \tag{35}$$

shows that the asymptotic behavior of the distribution function far from the turning point decays as

$$\lim_{P^2\Theta^2\to\infty} \log F \sim -\frac{P^4\Theta^4}{P}. \tag{36}$$

Thus, trajectories at large values of Θ are much less likely to be populated than that one would expect from Eq. (33).

The constant (32) motivates the change-of-variables, P and $R \equiv Q - \log Q - 1$, which transforms Eq. (31) to

$$\frac{\partial F}{\partial P} + \frac{2}{P}\frac{\partial F}{\partial R} + \frac{2}{P}F = 2Q^2\frac{\partial F}{\partial R} + \frac{2Q^2}{Q-1}\frac{\partial F}{\partial R} + \chi(R)\frac{\partial^2 F}{\partial R^2}, \tag{37}$$

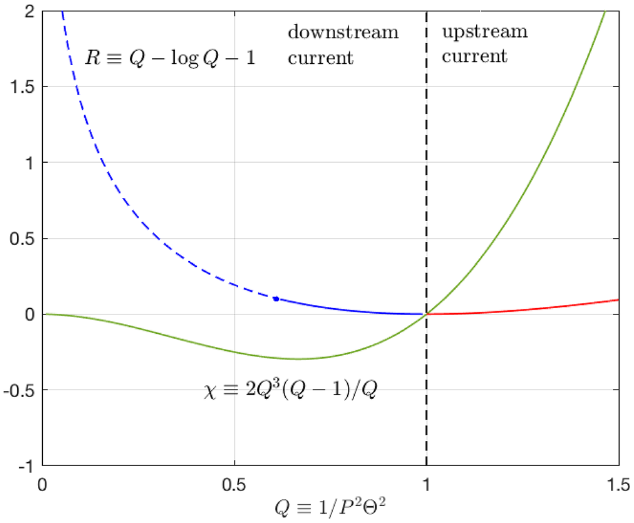

FIG. 6. Plot of the diffusion coefficient, χ (green curve), and the new variable R. The non-monotonicity of R as a function of Q divides the domain into downstream (blue) and upstream (red) sub-domains separated by the turning point (black dashed). The dashed blue region indicates where we use the minus sign in Eq. (39) to describe ρ.

where $\chi \equiv 2Q^3(Q-1)/Q = 2(1-P^2\Theta^2)/P^6\Theta^6$. Referring to Fig. 6, the transformation from Q to R is not one-to-one across the entire domain. To account for this, the domain is divided at the turning point $Q = 1$, and Eq. (37) is solved separately in the domain $Q \leq 1$ and $R \geq 0$, which we refer to as the downstream current, and the domain $Q > 1$ and $R \geq 0$, which is the upstream current. The two solutions should coincide at the turning point.

Our goal is to obtain the $P \ll 1$ wing of the distribution function. The smallness of the highest derivative term in a convective band in momentum space (see Fig. 5) enables us to posit the WKB approximation. We insert a function of the form $F = \exp(\rho/P)$, where $\rho < 0$. This form ensures that the distribution function decays as $P \to 0$. We insert the eikonal form into Eq. (37). In the periphery of the attractor where the WKB method is applicable, the equation (in the spirit of WKB) is reduced to a non-linear ODE, viz.,

$$0 = -\rho + 2\rho' - \chi(R)(\rho')^2, \tag{38}$$

where the primes denote differentiation with respect to R. The diffusion coefficient χ, which is shown in Fig. 6, vanishes at $R = 0$. On the downstream current, χ is non-monotonic and approaches zero far from the turning point, while on the upstream current, it monotonically increases to infinity. Using coefficients from Eq. (38), the quadratic formula yields two first-order ODEs for the function ρ

$$\rho' = \frac{\rho}{1 \mp \sqrt{1-\chi\rho}}. \tag{39}$$

As stated earlier, Eq. (39) is integrated along the upstream and downstream trajectories separately. In order to obtain a solution that is non-singular at the turning point, we use the form of Eq. (39) with the plus sign in the denominator. Each solution is initialized at $R = 0$ with $\rho(R=0) \equiv \rho_i$. The value of ρ_i is a constant of integration to be determined. Because the square root term in Eq. (39) vanishes at $R = 0$, the derivatives match at the turning point and analytical continuity is achieved as we transition from the downstream to upstream current.

As we travel against the downstream current far from the turning point towards large Θ, we encounter the region of momentum space where we expect the distribution function to match Eq. (36). Instead, we find that the asymptotic solution

$$\lim_{R\to\infty}\rho \sim -P\Theta \quad \text{[using the plus sign in Eq. (39)]}, \tag{40}$$

is incompatible with Eq. (36). If, on the other hand, we consider the asymptotic solution obtained from Eq. (39) with the minus sign, i.e.,

$$\lim_{R\to\infty}\rho \sim -P^4\Theta^4 \quad \text{[using the minus sign in Eq. (39)]}, \tag{41}$$

we achieve consistency with Eq. (36). Hence, in order to obtain a global solution, the asymptotic solution of Eq. (39) (with the minus sign) must be matched to the downstream solution of Eq. (39) extending from the turning point (with the plus sign). The matching point R_* (indicated in Fig. 6) should satisfy the following conditions:

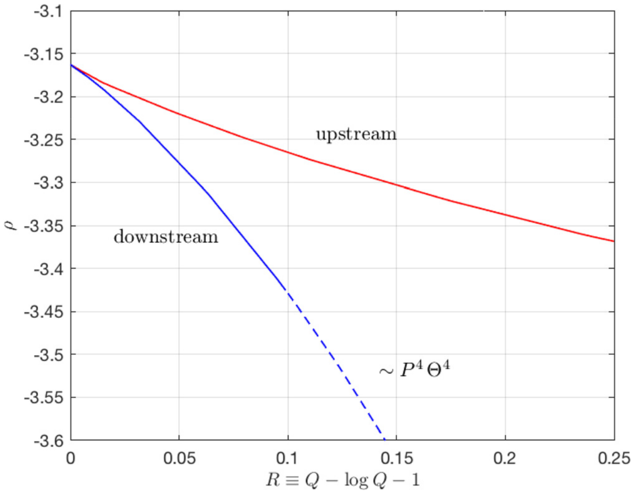

FIG. 7. Numerical solution of the ODEs Eq. (39); the shooting method yields $\rho_i = -3.163$, $R_* = 0.1$, and $\rho_* = -3.429$. The upstream solution is shown in red. The downstream solution is divided into two regions: the solid blue line from $0 < R \leq 0.1$ is described by Eq. (39) with the plus sign, while the dashed blue line $R > 0.1$ is described by Eq. (39) with the minus sign. The large R behavior of the downstream function is consistent with Eq. (36).

$$1 - \chi\rho|_{R=R_*} = 0, \quad \frac{\partial}{\partial R}(1 - \chi\rho)\Big|_{R=R_*} = 0. \tag{42}$$

The first condition ensures matching of ρ', and the second condition (in conjunction with the first) ensures that ρ remains analytic throughout the downstream domain. These two conditions determine the value of ρ_i and R_*.

The resulting solution of Eq. (39) is depicted in Fig. 7. The upstream function is depicted in red, while the downstream function is depicted in blue.

D. Behavior of the distribution function at small *P*

With the global description of ρ in hand, we calculate the distribution function, $F = \exp(\rho/P)$ [see Fig. 8(a)]. In order to validate the WKB approximation, we solve Eq. (30) numerically [see Fig. 8(b)] using a finite-difference solver. Finally, we use the solutions of Eq. (1) from Sec. IV [see Fig. 8(c)] to compare with solutions of Eq. (30). To be clear, Figs. 8(b) and 8(c) depict the long-term behavior of the distribution functions. The turning point is depicted as a black dashed line in each figure, but in the case of Fig. 8(c), the turning point is represented by $E\cos\theta - (1+p^2)/p^2 - 1/\bar{\tau}_{rad}\, p\sqrt{1+p^2}\sin^2\theta = 0$.

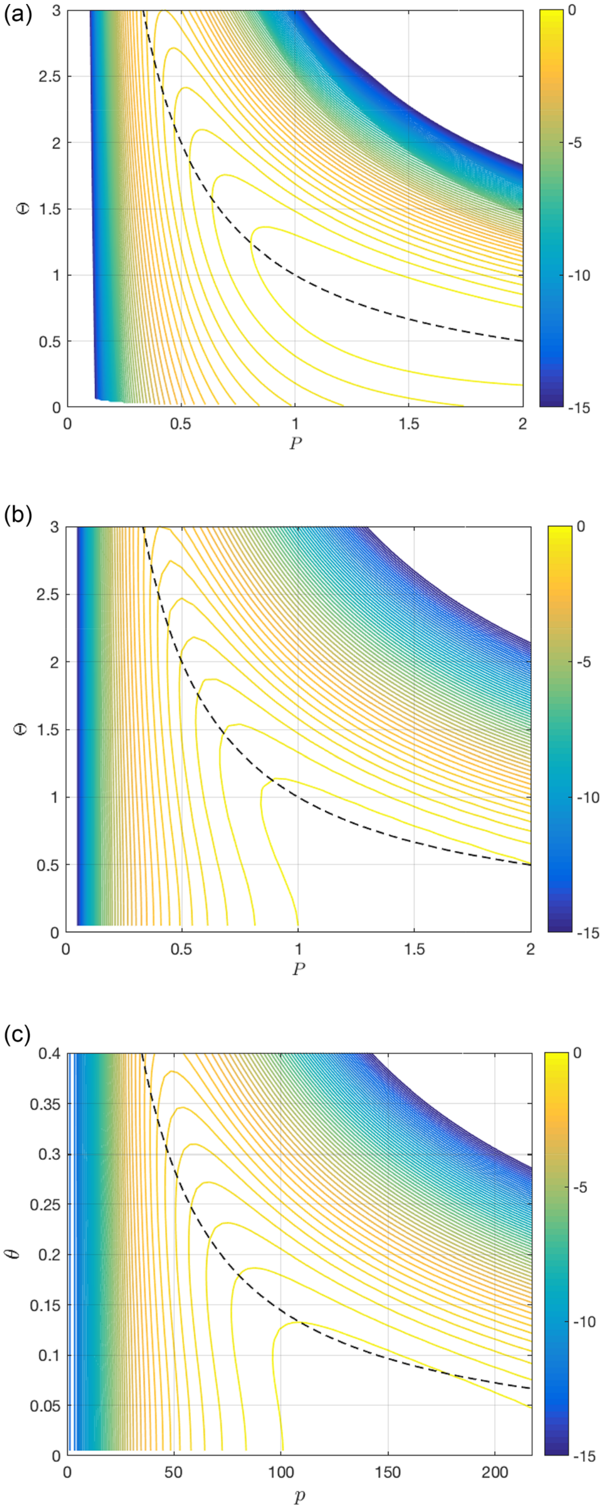

FIG. 8. Contours of the (logarithm of the) quasi-steady distribution function: (a) from solving Eq. (39); (b) numerical solution of Eq. (30); (c) numerical solution of Eq. (1) with $E = 3.1$, $\bar{\tau}_{rad} = 100$, $Z = 5$.

Although the frames of Fig. 8 do not extend far enough to show it, the electrons are limited to finite values of momentum. The distribution function in (a) reflects the trajectories depicted in Fig. 5. By the choice of normalization, $F = \mathcal{O}(1)$. Evident in Figs. 8(a)–8(c) is the peaking of the distribution function near the turning point. As we travel up or down in the pitch angle from the turning point in Fig. 8(a) while keeping P constant, ρ increases in absolute value, and as a result, the particle number decreases. On the other hand, if we travel along the turning point (thereby keeping ρ constant), then the particle number decreases in the direction of decreasing P. To be precise, the population decreases as

$$\log F \sim -\frac{(E-1)E\sqrt{\bar{\tau}_{rad}}}{\alpha}\frac{1}{p}, \tag{43}$$

along the turning point in dimensional units. The WKB approximation only extends as far as $p = \mathcal{O}(1)$ and therefore falls short of the slowing down region. Even so, we can say that the lifetime for $\alpha \gg 1$ will depend exponentially on the electric field due to the scarcity of electrons in the low-momentum tail indicated by Eq. (43). This conclusion draws from a similar line of reasoning that leads to the expression of the lifetime for $\alpha \ll 1$, Eq. (24).

VI. SUMMARY

The lifetime of seed runaways increases exponentially with the electric field, and this has been demonstrated by numerical and analytical treatments of the kinetic equation. The rate of exponential increase is shown to depend on the combination of parameters $\alpha \equiv (Z+1)/\sqrt{\tau_{rad}}$. We have demonstrated (at least schematically) how the lifetime of the seeds can be used to infer the threshold field. We characterize the lifetime in the limiting cases of small and large values α. In the case of $\alpha \ll 1$, an electric field very close to the Connor-Hastie critical value is sufficient to enable long-lived electrons. In the case of $\alpha \gg 1$, an electric field much larger than the Connor-Hastie critical value is necessary. When the electric field is very large, the kinetic equation attains a universal characteristic via re-scaling and formally has a time-independent solution. Subsequently, we apply the WKB method to probe the peripheral structure of the attractor and show that the longevity of the runaways is owed to a steep decay in the population of electrons in the low-momentum region of phase-space.

ACKNOWLEDGMENTS

This work was supported by the U.S. Department of Energy Contract Nos. DEFG02-04ER54742 and DE-SC0016283.

APPENDIX: APPLICABILITY OF WKB APPROXIMATION

Equation (38) is simplified from

$$-\frac{\rho}{P^2}+\frac{2\rho'}{P^2}+\frac{2}{P}=\frac{2\rho'}{P}Q^2+\frac{2\rho'}{P}\frac{Q^2}{Q-1}+\chi\left[\frac{\rho''}{P}+\left(\frac{\rho\prime}{P}\right)^2\right]. \quad \text{(A1)}$$

The first and second terms on the first line along with the final term on the second line are retained in the WKB approximation. We use Eq. (39) to obtain an expression for ρ''

$$\rho'' \approx \frac{\rho}{\left[1\mp\sqrt{1-\chi\rho}\right]^2}, \quad \text{(A2)}$$

and hence, Eq. (A1) can be written strictly in terms of the function ρ. Far from the turning point, Q is much less than unity, and hence, ρ, which scales asymptotically as $1/Q^2$, is much larger than unity there. As can be checked by comparing terms, the omission of the neglected terms is justified when $Q \ll 1$ or when $P \ll 1$. This window of applicability is represented schematically by the convective band peripheral to the attractor shown in Fig. 5.

[1] P. Aleynikov and B. N. Breizman, Phys. Rev. Lett. **114**, 155001 (2015).
[2] H. Dreicer, Phys. Rev. **115**, 238 (1959); **117**, 329 (1960).
[3] J. W. Connor and R. J. Hastie, Nucl. Fusion **15**, 415 (1975).
[4] R. Jaspers, N. J. Cardozo, F. C. Schúller, K. H. Finken, T. Grewe, and G. Mank, Nucl. Fusion **36**, 367 (1996).
[5] M. N. Rosenbluth and S. V. Putvinski, Nucl. Fusion **37**, 1355 (1997).
[6] C. Møller, Ann. Phys. **406**, 531 (1932).
[7] B. N. Breizman, Nucl. Fusion **54**, 072002 (2014).
[8] J. R. Martín-Solís, J. D. Alvarez, and R. Sánchez, Phys. Plasmas **5**, 2370 (1998).
[9] Z. Guo, C. J. McDevitt, and X. Tang, Plasma Phys. Controlled Fusion **59**, 044003 (2017).
[10] F. Andersson, P. Helander, and L. G. Eriksson, Phys. Plasmas **8**, 5221 (2001).

Appendix B

Included Paper B: Heating and Ablation of High-Z Pellets in High Temperature Plasmas

Note: At the time of this writing, Paper B is in the revision process with *Nuclear Fusion*.

Heating and Ablation of High-Z Cryogenic Pellets in High Temperature Plasmas

Adrian K. Fontanilla[*] and Boris N. Breizman[†]
Institute for Fusion Studies,
University of Texas at Austin,
Austin, TX 78712, USA

(Dated: May 23, 2019)

Abstract

A kinetic model is developed to determine the power deposition from energetic electrons into the neutral gas shield of an ablating high-Z pellet. For high-Z, the velocity distribution of the hot electrons is nearly isotropic, and we use this feature to develop solutions to the kinetic equation. In contrast to pre-existing models, we consider the effect of gyro-motion as well as elastic scattering of the hot electrons. Two limits are considered: when the gyro-frequency is much greater than the elastic collision frequency, the hot electrons diffuse longitudinally along the field lines as they slow down; but if the gyro-frequency is much less than the elastic collision frequency, the hot electrons diffuse radially. In both limits, it is possible to express the kinetic equation describing the hot electrons independently of the gas density profile, and therefore, the power deposition model is universal in this respect. The emphasis on elastic scattering yields an ablation rate which scales as $Z^{-7/6}$ which is different than $Z^{-2/3}$ shown in Ref. [1]. It is also shown that the sheath potential required to maintain ambipolarity in the cloud scales as $Z^{-1/3}$. Fluid simulations yield ablation rates that scale with the four-thirds power of the pellet radius in agreement with Ref. [2].

---

[*] afontanilla@utexas.edu

[†] breizman@mail.utexas.edu

I. INTRODUCTION

At the time of this writing, pellets of high-Z material are being investigated as a means of disruption mitigation for ITER. Pellets are seen as favorable to massive gas injection due to deeper penetration of the impurity material into the plasma and the ability to adjust the cooling properties via mixing fractions (Ref. [3]). These two factors, in particular, help to meet the time constraints required for safe thermal and current quench. Thermal quenches that are too fast (as it happens with killer pellet strategies) are susceptible to runaway electron production. On the other hand, current quenches that occur too slowly leave the machine susceptible to halo currents.

One of the guidelines of the mitigation strategy is to dissipate a significant fraction of the plasma thermal energy, while at the same time avoiding hot spots at the walls. A thorough consideration of the pellet strategy requires following the energy transfer from the plasma electrons to the impurity material and finally to the walls via radiation. This paper aims to address the power deposition from the plasma electrons to the pellet when the pellet material is of a high-Z atomic species. The calculated power deposition is then used to determine the pellet ablation rate and describe the out-going flow.

The cloud of ablated material surrounding the pellet contains electrons that are much colder and denser than the ambient background plasma. Hot electrons entering the cloud from the background collide with the cold electrons in the cloud. The electron-electron collisional time scales are much shorter for the cold-cold collisions than for the hot-cold collisions. Because of that, the cold electrons can be viewed as thermalized, whereas the hot electron distribution function in the cloud can deviate from Maxwellian significantly due to collisions with the cold population. This situation requires a kinetic description of the hot electron distribution function as they slow down and scatter in the ablation cloud. Existing kinetic models generally employ a Bethe-Bloch (Ref. [4]) approximation for the slowing-down force, but the handling of elastic scattering varies. Elastic scattering reduces the incident particle flux through the cloud interface via backscatter, and for those electrons that do penetrate, their penetration depth diminishes. In one of the earlier works for carbon pellets, the authors of Ref. [6] uses a loss function to describe inelastic forces but neglect elastic scattering in the kinetic equation, although they argue that elastic scattering reduces the ablation rate by approximately 10 percent. Ref. [1] is similar in their kinetic approach but carries out gas-dynamic simulations systematically to determine ablation rates for a wide range of parameters, including pellet material. The authors then perform a statistical fitting in order to obtain a generalized power-law scaling for the ablation rate. As a result, this scaling law differs from the one of Ref. [5]. Ref. [7] suggests an expression for the heat flux that is obtained by representing the angular distribution with a delta function. Ref. [5] solves the kinetic equation with elastic scattering included but only for the case of hydrogen. In comparison to the prior work, we herein consider the electron distribution function within high-Z material, in which case elastic scattering is a significant factor in the kinetic equation. We further distinguish our work from the existing neutral gas shielding models by recognizing that the elastic scattering and gyro-motion timescales may be comparable. The ratio of the elastic collision frequency to the gyro-frequency determines how the fast electrons travel with respect to the magnetic field lines. The kinetic equation presented in this paper provides a general description of the hot electrons in high-Z material, but we will consider each limit when the gyro-frequency is much larger and much smaller than the elastic collision frequency.

The dynamics of the hot electron dynamics and gas flow are detailed in Sec. II which also includes back-of-the-envelope calculations of the power deposition and ablation rate. In Sec. III, we formulate the kinetic equation for the hot electron distribution function in a homogeneous magnetic field and solve it for the case that the distribution function is nearly isotropic in velocity-space. The distribution function is then used for a more rigorous calculation of the power deposition. In Sec. IV, this power deposition is input to fluid simulations, and we calculate ablation rates as a function of the pellet radius. Although the power deposition model is general to any pellet consisting of high-Z, the ablation model that we use is from Ref. [2] and is limited to cryogenic pellets (i.e. those with very low sublimation energies). In addition, the ablation model does not account for radiative losses (Ref. [8, 9]). The final section discusses the results and summarizes our conclusions. In the Appendix, we calculate the sheath potential that forms between the hot plasma and pellet material.

II. PHYSICS MODEL

Our work models the ablation cloud as a neutral gas. Almost immediately after a pellet is immersed in the plasma, ambient electrons heat the pellet surface and cause ablation. The amount of material heated by the fast electrons at the surface of the pellet depends on the penetration depth of the electrons. This depth depends on whether or not the pellet is of high-Z material. For low-Z pellets, the penetration depth is roughly the stopping length associated with the slowing-down force. Electrons with thermal velocity $v_{th} = \sqrt{2T_\infty/m}$ have a collision frequency (see Ref. [10]) of

$$\nu = \frac{8\pi Z N e^4 \ln\Lambda_{in}}{m^2 v_{th}^3} \tag{1}$$

in a material with atomic density N, so the stopping length is

$$\lambda = \frac{v_{th}}{\nu} = \frac{T_\infty^2}{2\pi Z N e^4 \ln\Lambda_{in}} \tag{2}$$

The inelastic Coulomb logarithm, $\ln\Lambda_{in}$, contains the ratio of the minimum and maximum impact parameters for collisions between the hot plasma electrons and the bound electrons of the pellet material. The minimum impact parameter is the deBroglie wavelength, $\hbar/mv$, while the maximum impact parameter is $v \times \hbar/2I$ since the ionizing collision should occur on a timescale shorter than the bound electron orbital period, $\hbar/2I$, where I is the mean excitation potential of the bound electrons. Consequently, $\ln\Lambda_{in} = \ln(E/I)$ (see also Ref. [4]).

For high-Z pellets (which is the focus of the present work), incident electrons perform a random walk through the material due to the prevalence of elastic scattering. In this case, the penetration depth δ_p is the net displacement achieved during the slowing-down time, ν^{-1}, i.e. $\delta_p \sim \sqrt{D\,\nu^{-1}} = \sqrt{(\lambda/Z)\,v_{th}\nu^{-1}}$, where $D \sim (\lambda/Z)v_{th}$ is the diffusion coefficient, and (λ/Z) is the mean-free-path associated with 90-degree scattering. Consequently, the penetration depth through high-Z material is $\delta_p \sim \lambda/\sqrt{Z} = \frac{T_\infty^2}{2\pi Z^{3/2} N e^4 \ln\Lambda_{in}}$. For keV ambient electrons, the surface layer thickness of an ablating solid-state pellet of density $10^{21}\,cm^{-3}$ is on the order of $10^{-1}/Z^{3/2}\,cm$, and so for $Z \gg 1$, the surface layer is much thinner than the radius of a typical pellet which is $R_p \sim 0.1 - 1\,cm$. This layer forms a cold cloud of neutral atoms surrounding the pellet which throttles the heat flux reaching the pellet surface. This cloud heats up, expands, and it becomes semi-transparent when the layer thickness is comparable to the pellet radius. Hot electrons can then reach the pellet surface and heat the next layer, which leads to continuous ablation. At around ten times R_p the shielding becomes negligible, and the ambient electron distribution function remains unperturbed by the impurity cloud at this distance.

There is an additional shielding mechanism due to an electrostatic sheath at the interface between the cloud and the ambient plasma. This sheath maintains ambipolarity, but its role is of secondary importance in the high-Z limit. This is because the net particle flux is relatively small due to backscatter in the high-Z case. The diffusion equation, Eq. (14), indicates that the incident electron flux scales as $n_\infty v_{th}/Z^{1/2}$, which is a factor $Z^{1/2}$ lower as compared to the case when there is no scattering. This particle flux is used to calculate the sheath potential in the Appendix, and we show that the sheath potential required to maintain ambipolarity scales as $Z^{-1/3}$.

The description of pellet ablation in a tokamak should generally take into account the role of the magnetic field. For a magnetic field strength of $10\,kG$, the magnetic pressure is typically much smaller than the gas pressure within the narrow layer at the pellet surface. Also, the gas is essentially neutral in this area, and therefore, its expansion should not be affected by the magnetic field unlike at further distances where the gas is ionized. What is affected by the magnetic field is the motion of hot electrons in the ablation cloud, which varies between longitudinal (along the field lines) or radial with respect to the pellet center. The direction depends on the ratio of the electron gyro-frequency to the elastic collision frequency inside the cloud. The gyro-frequency is $\omega_c = eB/mc$. The elastic collision frequency (see Ref. [11]) is $\nu_s = Z\nu \ln\Lambda_{el}/\ln\Lambda_{in}$, where $\ln\Lambda_{el}$ is the elastic scattering logarithm. It is equal to

$$\ln\Lambda_{el} \approx \ln\left(\frac{0.591}{b\,Z^{1/3}}\frac{a_0}{\hbar/mv}\right), \tag{3}$$

where a_0 is the Bohr radius and $b \approx 0.5-0.6$ but depends on the atomic species (see Ref. [12]). Taking reactor-grade parameters, as an example, the gyro-frequency is $\omega_c \approx 2\times10^{11}\,s^{-1}$ for a $10\,kG$ field. The elastic collision frequency of $2\,keV$ electrons is comparable to this in cloud densities of $N \approx 10^{19}\,cm^{-3}$, which suggests that we must be cognizant of the magnetic field's impact on pellet heating. Thus, the kinetic theory developed in Sec. III treats collisions and the Lorentz force on equal footing, but before we proceed, we present a rudimentary discussion of the ablation process.

A. Simplified Ablation Model

Ultimately, the most relevant conclusion from an analysis involving pellets is the ablation rate. The ambient plasma electrons of density n_∞ have a mean-free-path of $\lambda_\infty = T_\infty^2/2\pi n_\infty e^4 \ln\Lambda_{in}$. For typical plasma parameters, the mean-free-path is much longer than the scale of the machine, and therefore, they travel freely until they encounter the impurity pellet which has density $N \gg n_\infty$. The mean-free-path of the streaming electrons drastically reduces to Eq. (2) upon incidence. As plasma electrons stream through the cold impurities, they lose energy mostly due to collisions with bound electrons. The power density transferred to the pellet material is estimated by

$$Q \sim n_\infty m v_{th}^2 \times \nu = \frac{2^{5/2}\pi e^4}{m^{1/2}} \frac{Z N n_\infty \ln\Lambda_{in}}{T_\infty^{1/2}} \tag{4}$$

where in what follows, the similarity symbol indicates that the relation holds within an undetermined constant of order unity. Eventually, atoms are ablated from the surface of the pellet which expands with a velocity that is roughly sonic. When the flow velocity becomes sonic, i.e. $\gamma T_*/M = V_*^2$, the ablation cloud has been heated to

$$T_* \sim A_* \times (R_*/V_*) \Longrightarrow V_*^3 \sim \frac{\gamma R_* A_*}{M} \sim 2^{5/2}\pi\,\gamma \frac{e^4}{m^{1/2}M} \times R_* \times \frac{Z n_\infty \ln\Lambda_{in}}{T_\infty^{1/2}} \tag{5}$$

where γ is the specific heat ratio, M is the atomic mass of the ablated particles, R_* is the sonic radius, and $A_* = Q_*/N$ is the heating rate per atom at the sonic radius. (We use starred notations to indicate sonic quantities.) We have taken Q_* to be equal to Eq. (4) to within a factor of unity. The ablated particle flux is constant, and hence, $R_p^2 N_p \dot{R}_p = R_*^2 N_* V_*$, where R_p is the pellet radius and $\dot{R}_p$ is the pellet regression speed. Roughly half of the heat flux is absorbed in the gas shield, which has optical thickness $N_* R_*$, while the other half is absorbed in the pellet, which has optical thickness $N_p \delta_p$, where $\delta_p \sim Z^{-1/2}$ is the penetration depth in the pellet material. Thus, $N_* R_* \sim N_p \delta_p$ which we plug into the ablated particle flux to obtain $\dot{R}_p/\delta_p = V_*/R_*$. Then

$$\dot{R}_p \sim \frac{1}{\pi^{2/3}(e^4)^{2/3}} \left(\frac{\gamma}{m^{1/2}M}\right)^{1/3} \times R_*^{-2/3} N_p^{-1} \times \frac{n_\infty^{1/3} T_\infty^{11/6}}{Z^{7/6}(\ln\Lambda_{in})^{2/3}} \tag{6}$$

We then obtain the following scaling law for the ablation rate:

$$G = 4\pi M R_p^2 N_p \dot{R}_p \sim \frac{4\pi M}{(\pi e^4)^{2/3}} \left(\frac{\gamma}{m^{1/2} M}\right)^{1/3} \times R_p^{4/3} \times \frac{n_\infty^{1/3} T_\infty^{11/6}}{Z^{7/6} (\ln \Lambda_{in})^{2/3}} \tag{7}$$

since $R_* \sim R_p$. Eq. (7) contains a $-7/6$ power of Z as opposed to the $-2/3$ that appears in Ref. [1]. This difference results from the emphasis on scattering; i.e. using the penetration depth of hot electrons δ_p in the estimate for the optical thickness of the pellet versus using their mean-free-path. More rigorous calculations in Sec. IV determine the coefficient to the scaling law of Eq. (7).

III. KINETIC THEORY

Although the previous section introduces some convenient scalings, the rest of this paper will treat the problem of pellet ablation more rigorously, and we begin with the power deposited by the hot electrons to the cloud. In actuality, the power varies as the hot electrons slow down. For fast electrons, i.e. those with energy greater than 100 eV, the stopping power is $P_s = 8\pi Z N e^4 \ln \Lambda_{in} / mv$ (see Ref. [4]). Therefore, the energy deposited per unit volume per unit time by the background plasma in this case is

$$Q = n_\infty \int P_s f \, \mathrm{d}^3 v = \frac{16\pi^2 \times Z N n_\infty e^4 \ln \Lambda_{in}}{m} \int f \, \mathrm{d}v^2 \tag{8}$$

where f is the distribution function of the hot electrons within the cloud which is normalized such that $n_\infty \int f \, \mathrm{d}^3 v = 1$. The problem of cloud heating thus reduces to calculating the integral $\int f \, \mathrm{d}v^2$. Eq. (8) is consistent with the estimate Eq. (4) since $\int f \, \mathrm{d}v^2 \sim \sqrt{m/T_\infty}$.

The kinetic equation for the hot electron distribution function within a neutral cloud of high-Z impurities includes the streaming term and the effects of slowing down due to inelastic collisions with cold electrons, as well as elastic scattering due to collisions with atomic nuclei of density N. Although the ambient plasma cools down, the reservoir of hot electrons is much larger than the number of electrons inside the cloud. As a result, the ambient cooling rate is much slower than the collisional time scales within the cloud, and we therefore, treat the distribution function within the cloud as quasi-stationary. The kinetic equation for the hot electron distribution function is

$$\frac{\partial}{\partial \vec{r}} \cdot \vec{v}\, f - \frac{1}{v^2}\frac{\partial}{\partial v} v^2 \nu(v) v\, f + \omega_c \frac{\partial f}{\partial \psi} = \frac{\nu_s(v)}{2\sin\theta}\frac{\partial}{\partial \theta}\sin\theta \frac{\partial f}{\partial \theta} + \frac{\nu_s(v)}{2\sin^2\theta}\frac{\partial^2 f}{\partial \psi^2} \tag{9}$$

where θ and ψ are the polar and azimuthal angles in velocity-space, respectively. The incident plasma electrons are considered much hotter than the cloud electrons, and so the electron-electron collision frequency, ν, is given by Eq. (1) with $v_{th} \to v$.

In what follows, we use cylindrical geometry (ρ, φ, z) in coordinate-space, and θ measures from the z-axis. In the limit of large Z, the right-hand-side (RHS) of Eq. (9) dominates, and hence, the distribution function is isotropic in velocity-space to lowest order. To that effect, we let $f = F(\vec{r}, v) + \mathcal{O}(Z^{-1})$, where the correction is the anisotropic part of the distribution function. Let $\langle g \rangle \equiv (1/4\pi) \int_0^{2\pi} \int_0^{\pi} g \sin\theta \, \mathrm{d}\theta \, \mathrm{d}\psi$ represent the angular average in velocity-space, and apply it to Eq. (9). Terms involving angular derivatives in velocity-space are annihilated, and we are left with a statement that the slowing-down term is balanced by the angular average of the streaming terms, i.e.

$$\begin{aligned} &\frac{\partial}{\partial z} v \langle \cos\theta\, f \rangle + \frac{1}{\rho}\frac{\partial}{\partial \rho}\rho \left[v\cos\varphi \langle \sin\theta\cos\psi\, f\rangle + v \sin\varphi \langle \sin\theta \sin\psi\, f \rangle \right] \ldots \\ &\qquad + \frac{1}{\rho}\frac{\partial}{\partial \varphi}\left[v\sin\varphi \langle \sin\theta\cos\psi\, f\rangle - v\cos\varphi \langle \sin\theta\sin\psi\, f\rangle\right] - \frac{1}{v^2}\frac{\partial}{\partial v} v^3 \nu \,\langle f \rangle = 0 \end{aligned} \tag{10}$$

A cursory calculation of the moments is performed in the Appendix. The results are obtained by convolving Eq. (9) with $\cos\theta$, $\sin\theta\cos\psi$, and $\sin\theta\sin\psi$ assuming f is the first term in a Chapman-Enskog expansion (see Ref. [13]), i.e. $f \to F$ in terms proportional to ω_c and ν_s. The results are reproduced below:

$$\langle \cos\theta\, f \rangle = -\frac{1/3}{\nu_s} v \frac{\partial F}{\partial z} \tag{11}$$

$$\langle \sin\theta\cos\psi\, f\rangle = +\frac{1/3}{\omega_c^2 + \nu_s^2}\left[\omega_c \left(v\sin\varphi \frac{\partial F}{\partial \rho} + \frac{v\cos\varphi}{\rho}\frac{\partial F}{\partial \varphi}\right) - \nu_s \left(v\cos\varphi\frac{\partial F}{\partial \rho} - \frac{v\sin\varphi}{\rho}\frac{\partial F}{\partial \varphi}\right)\right] \tag{12}$$

$$\langle \sin\theta\sin\psi\, f\rangle = -\frac{1/3}{\omega_c^2 + \nu_s^2}\left[\omega_c \left(v\cos\varphi \frac{\partial F}{\partial \rho} - \frac{v\sin\varphi}{\rho}\frac{\partial F}{\partial \varphi}\right) + \nu_s \left(v\sin\varphi\frac{\partial F}{\partial \rho} + \frac{v\cos\varphi}{\rho}\frac{\partial F}{\partial \varphi}\right)\right] \tag{13}$$

To proceed, we consider axial symmetry and plug these moments into Eq. (10) to obtain

$$-\frac{1}{3}\frac{\partial}{\partial z}\frac{1}{\nu_s} v^2 \frac{\partial F}{\partial z} - \frac{1}{3}\frac{1}{\rho}\frac{\partial}{\partial \rho}\rho \,\frac{\nu_s}{\omega_c^2 + \nu_s^2} v^2 \frac{\partial F}{\partial \rho} - \frac{1}{v^2}\frac{\partial}{\partial v} v^3 \nu \, F = 0 \tag{14}$$

The relative strength of the magnetic field determines whether or not Eq. (14) describes diffusion longitudinally (i.e. along z) or radially (i.e. along $r = \sqrt{z^2 + \rho^2}$). To wit, when

$\omega_c^2 \gg \nu_s^2 \gg 1$ we obtain

$$-\frac{1}{3}\frac{\partial}{\partial z}\frac{1}{\nu_s}v^2\frac{\partial F}{\partial z} - \frac{1}{v^2}\frac{\partial}{\partial v}v^3\nu\, F = 0 \tag{15}$$

while in the limit $\nu_s^2 \gg \omega_c^2 \gg 1$,

$$-\frac{1}{3}\frac{1}{r^2}\frac{\partial}{\partial r}\frac{r^2}{\nu_s}v^2\frac{\partial F}{\partial r} - \frac{1}{v^2}\frac{\partial}{\partial v}v^3\nu\, F = 0 \tag{16}$$

In this last equation, r is the radial coordinate in spherical geometry that measures from the pellet center. In either case, a convenient change-of-variables is given by:

$$\xi \equiv \frac{8\pi Z e^4}{m^2 v_{th}^4} \times \left(3Z \ln\Lambda_{in} \ln\Lambda_{el}\right)^{1/2} \int_z^\infty N(z')\,\mathrm{d}z'\,, \quad \tau \equiv \frac{1}{8}\left(\frac{v}{v_{th}}\right)^8 \tag{17}$$

where $z \to r$ in the spherical case. The former variable is space-like; it is the line-integrated density which is essentially normalized by the scattering cross-section since the cross-section goes as $(e^2/mv_{th}^2)^2$. The latter variable is time-like and has a power-law relation that is a consequence of using the Bethe-Bloch approximation for the slowing-down force. Applying these change-of-variables yields a universal description of the distribution function irrespective of the density profile in a thin ablation cloud as seen from the resulting anti-diffusion equations below

$$\frac{\partial F}{\partial \tau} + \frac{\partial^2 F}{\partial \xi^2} = 0 \qquad (\omega_c^2 \gg \nu_s^2) \tag{18}$$

$$\frac{\partial F}{\partial \tau} + \frac{1}{r^2}\frac{\partial}{\partial \xi}r^2\frac{\partial F}{\partial \xi} = 0 \qquad (\omega_c^2 \ll \nu_s^2) \tag{19}$$

While the space-like variable affords us universality, the time-like variable makes the kinetic equation amenable to Fourier decomposition. The diffusive nature of Eq. (18) and Eq. (19) distinguishes these equations from the models in which elastic scattering is neglected.

We note that the structure of Eq. (19) is identical to Eq. (18) in a thin layer close to the pellet surface where r can be considered nearly constant. Despite these mathematical similarities, the physical picture is quite different. In the former case, the hot electrons follow the field lines closely en-route to the pellet surface; that is, the gyro-radius is small compared to the pellet radius. Electrons on different field lines encounter different cloud thicknesses and hence heat the pellet surface asymmetrically. As a result, a two-dimensional description of the ablation cloud is required to resolve the flow. In the latter case, the electron heating is spherically-symmetric and a one-dimensional fluid model is sufficient to describe the ablation flow. We first look at the one-dimensional (i.e. slab) reduction of Eq. (19) which is identical in structure to Eq. (18), and then we discuss how to generalize to spherical geometry.

A. Strong Magnetic Field/Thin Layer at the Pellet Surface

As previously noted, r can be treated as a constant within a thin layer near the pellet surface, which simplifies Eq. (19) to Eq. (18) and allows us to consider the two cases simultaneously. The simplification $r = constant$ implies that the layer thickness is much smaller than the pellet size. This is valid in the earliest stages of ablation when a surface layer is continuously heated, and the line-integrated density is thus conserved. However, the line-integrated density is no longer conserved when the ablated material propagates from the surface, in which case the geometry becomes spherical. At this stage, the ablation cloud becomes less opaque, but as a result allows fast electrons to heat the next surface layer.

In-line with τ being a time-like variable, we solve Eq. (18) by performing a Fourier transform from τ-space to the frequency-like ω-space. The Fourier image of the distribution function within the layer is

$$\tilde{F}(\xi,\omega) = \tilde{f}_i(\omega)e^{-\xi\sqrt{i\omega}} \tag{20}$$

where the tilde denotes Fourier transform and $\tilde{f}_i(\omega) \equiv \int_0^\infty \mathrm{d}\tau\, f_i(\tau)e^{i\omega\tau}$ is the Fourier image of the distribution function incident on the cloud. The choice of the square root branch in the exponential argument in Eq. (20) must ensure that the solution of Eq. (18) vanishes at large values of the line-integrated density ξ.

To obtain the power density Q for the strong magnetic field/slab model, we insert the inverse Fourier transform of Eq. (20) into the integral of Eq. (8)

$$\begin{aligned}\int f\,\mathrm{d}v^2 &= 2\,\mathrm{Re}\left\{\int_0^\infty \mathrm{d}v^2 \int_0^\infty \frac{\mathrm{d}\omega}{2\pi}e^{-i\omega\tau}\,e^{-\xi\sqrt{i\omega}}\int_0^\infty \mathrm{d}\tau'\,e^{i\omega\tau'}f_i(\tau')\right\} &(21)\\ &= 2\,\mathrm{Re}\left\{\int_0^\infty \mathrm{d}y\,e^{-iy^4}\int_0^\infty \frac{\mathrm{d}\omega}{2\pi}\frac{8^{1/4}}{\omega^{1/4}}e^{-\xi\sqrt{i\omega}}\int_0^\infty \mathrm{d}\tau'\,e^{i\omega\tau'}f_i(\tau')\right\} &(22)\end{aligned}$$

where $y \equiv (\omega/8)^{1/4} v^2 = (\omega/\tau)^{1/4}$. Here and in what follows, f is normalized by $(\sqrt{\pi} v_{th})^{-3}$ and v by v_{th}. The outer-most integral evaluates to $\int_0^\infty e^{-iy^4}\,\mathrm{d}y = e^{-\pi i/8}\Gamma(5/4)$. Continuing with the evaluation of the integrals, we have

$$\int f\,\mathrm{d}v^2 = 2\,\mathrm{Re}\left\{\frac{8^{1/4}\Gamma(5/4)}{2\pi} e^{-\pi i/8} \int_0^\infty \frac{\mathrm{d}\omega\, e^{-\xi\sqrt{i\omega}}}{\omega^{1/4}} \int_0^\infty \mathrm{d}\tau\, e^{i\omega\tau} f_i(\tau)\right\} \tag{23}$$

$$= 2\,\mathrm{Re}\left\{\frac{4\cdot 8^{1/4}\Gamma(5/4)}{2\pi} e^{-\pi i/8} \int_0^\infty \mathrm{d}\tau\, f_i(\tau) \int_0^\infty \mathrm{d}z\, z^2 \exp\Big(-\xi\sqrt{i} z^2 + i z^4 \tau\Big)\right\} \tag{24}$$

$$= 2\,\mathrm{Re}\left\{-\frac{4\cdot 8^{1/4}\Gamma(5/4)}{2\pi} \frac{e^{-\pi i/8}}{e^{\pi i/4}} \frac{\partial}{\partial\xi} \int_0^\infty \mathrm{d}\tau\, f_i(\tau) \int_0^\infty \mathrm{d}z \exp\Big(-\xi\sqrt{i} z^2 + i z^4 \tau\Big)\right\} \tag{25}$$

where $z^4 \equiv \omega$. The inner integral is

$$\int_0^\infty \mathrm{d}z \exp\Big(-\sqrt{i}\xi z^2 + i z^4 \tau\Big) = \frac{e^{3\pi i/8}}{4}\sqrt{\frac{\xi}{\tau}} e^{-\xi^2/8\tau} K_{1/4}\left(-\frac{\xi^2}{8\tau}\right) = \frac{e^{5\pi i/8}}{4}\sqrt{\frac{\xi}{\tau}} e^{-\xi^2/8\tau} K_{1/4}\left(\frac{\xi^2}{8\tau}\right) \tag{26}$$

where we use the analytic continuation of the Bessel function, $K_\nu(e^{m\pi i}x) = e^{m\nu\pi i} K_\nu(x)$ to express K_ν with positive argument. The final result is expressed as

$$\int f\,\mathrm{d}v^2 = -\frac{\Gamma(1/4)}{2^{1/4}\pi} \frac{\partial}{\partial\xi} \frac{1}{\xi^{1/2}} \int_0^\infty \mathrm{d}\tau \sqrt{\frac{\xi^2}{8\tau}} \exp\left(-\frac{\xi^2}{8\tau}\right) K_{1/4}\left(\frac{\xi^2}{8\tau}\right) f_i(\tau) \tag{27}$$

B. Radially-Extended Spherical Cloud

We seek a semi-analytic solution to Eq. (19) by approximating the line-integrated density profile in the following way. Crude estimates (as well as more detailed calculations contained in Ref. [14]) give a simple radial profile of the cloud density in the case when the heating rate per cloud particle is constant. In fact, it is nearly so in the outer regions of the cloud where the cloud is not very dense. The cloud temperature increases linearly with time t in this situation. The cloud velocity is $V \approx \dot{r}$, and moreover, $V \sim \sqrt{t}$ when the flow is sonic. Integrating $\dot{r} \sim \sqrt{t}$ yields the self-similarity $r \sim t^{3/2}$, and from this, we obtain the velocity profile $V \sim r^{1/3}$. A power-law for the density is obtained by plugging in $V \propto r^{1/3}$ into the ablation rate, $G \sim r^2 NV = \mathit{constant}$, and the result is $N \sim r^{-7/3}$. It follows from the integration of N that the line-integrated density is

$$\int_r^\infty N\,\mathrm{d}r' \propto r^{-4/3} \Longrightarrow r^2 \propto \xi^{-3/2} \tag{28}$$

We use this result in Eq. (19) to obtain

$$\frac{\partial F}{\partial\tau} + \frac{\partial^2 F}{\partial\xi^2} - \frac{3}{2\xi}\frac{\partial F}{\partial\xi} = 0 \tag{29}$$

The ODE describing the Fourier projection of F is given by

$$-i\omega\tilde{F} + \frac{\partial^2 \tilde{F}}{\partial \xi^2} - \frac{3}{2\xi}\frac{\partial \tilde{F}}{\partial \xi} = 0 \tag{30}$$

The solution to this ODE is composed of Bessel functions which satisfy the following boundary conditions: $F(0,\tau) = f_i(\tau)$ and $F(\xi \to \infty, \tau) = 0$. The proper combination of Bessel functions are Hankel functions of the first and second kind, $H^{(1,2)}_{5/4}$, and the exact solution to Eq. (29) is

$$\tilde{F}(\xi,\omega) = \frac{2^{3/4}\pi\exp(-13\pi i/16)}{\Gamma(1/4)}\begin{cases} +(\xi\sqrt{\omega})^{5/4}H^{(2)}_{5/4}(e^{7\pi i/4}\xi\sqrt{\omega})\tilde{f}_i^*(\omega), & \omega \geq 0 \\ -(\xi\sqrt{\omega})^{5/4}H^{(1)}_{5/4}(e^{7\pi i/4}\xi\sqrt{\omega})\tilde{f}_i(-\omega), & \omega < 0 \end{cases} \tag{31}$$

where Γ is the gamma function. The pre-factor appearing above is obtained from the evaluation of $[(\xi\sqrt{\omega})^{5/4}H^{(1,2)}_{5/4}(e^{7\pi i/4}\xi\sqrt{\omega})]^{-1}$ at $\xi = 0$, and it ensures that the boundary condition at $\xi = 0$ is satisfied. We note that for small arguments of the Hankel functions,

$$H^{(1,2)}_{5/4}(x) \approx \mp\frac{i\,\Gamma(1/4)}{2^{3/4}\pi}\left(\frac{1}{x^{5/4}} + x^{3/4}\right) \tag{32}$$

Integrations in ω-space are ultimately reduced by half because the distribution function is real. Thus, we only consider $\omega \geq 0$ and avoid branch cuts in ω-space. One can confirm that $F^*(\xi,\omega) = F(\xi,-\omega)$ by using the identity $H^{(1)}_\nu(x^*) = [H^{(2)}_\nu(x)]^*$ in Eq. (31).

In the spherical case, where f is given by the inverse Fourier transform of Eq. (31),

$$\int f\,\mathrm{d}v^2 = 2\,\mathrm{Re}\left\{2^{1/2}e^{-15\pi i/16}\int_0^\infty \mathrm{d}z\, z^2(\xi z^2)^{5/4}H^{(2)}_{5/4}(e^{7\pi i/4}\xi z^2)\int_0^\infty \mathrm{d}\tau\, e^{iz^4\tau}f_i(\tau)\right\} \tag{33}$$

The power density in the one-dimensional (strong magnetic field/slab) and three-dimensional (spherical) cases are plotted in Fig. 1 in the case that f_i is Maxwellian.

C. Perturbative method

In general, the spatial description of the distribution function within the cloud requires a coupling of the kinetic equation to a fluid model describing the impurity cloud since Eq. (19) contains the impurity density profile, $N(r)$, implicitly through the variable r. The solutions given by Eq.(20) and Eq. (31) circumvent this difficulty. In the former case, N does not appear in the kinetic equation when the line-integrated density is used as a variable and the geometry is one-dimensional. In the latter, there is a fortuitous power-law for the density that allowed the substitution of r^2 with a term proportional to $\xi^{-3/2}$.

A complete kinetic description should, however, include the cloud density dependence. The following strategy does so, while preserving the qualitative features of Sec. III A and Sec. III B. In order to blend the qualities of our previous findings, we subtract the term $(3/2\xi)\partial F/\partial\xi$ from both sides of Eq. (19) then re-arrange to obtain

$$\frac{\partial F}{\partial \tau} + \frac{\partial^2 F}{\partial \xi^2} - \frac{3}{2\xi}\frac{\partial F}{\partial \xi} = -\left(\frac{2}{r}\frac{\partial r}{\partial \xi} + \frac{3}{2\xi}\right)\frac{\partial F}{\partial \xi} \tag{34}$$

The line-integrated density increases exponentially as it approaches very close to the pellet surface, and hence, $\partial\xi/\partial r$ is very large. In this limit, Eq. (34) reduces to Eq. (18). Far away from the surface, $(2/r)\partial r/\partial\xi \to -(3/2\xi)$, and we regain Eq. (29). In the intermediate region of the cloud, the RHS of Eq. (34) can be included via Green's function techniques. Although we do not carry out the exercise here, the proposed strategy produces a distribution function that retains the features of F from the previous sub-sections at asymptotic limits of the line-integrated density.

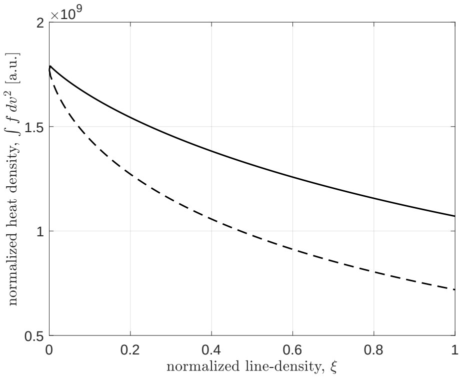

FIG. 1. Normalized heat rate density as a function of normalized line-density where the strong magnetic field/slab model using Eq. (27) is shown as a dashed black line, and the spherical model using Eq. (33) is shown in solid. Since the shape of the curves are universal, the plot is a comparison of $\int f\,\mathrm{d}v^2$ in the two models.

IV. ABLATION RATE

The ablation rate is calculated below in the case that the electron heating is spherically-symmetric, but we comment on the case of axisymmetric heating after. The steady-state fluid equations (see also Ref. [2]) describing the radial profile of the ablation cloud are

$$G = 4\pi M R^2 N V = \text{constant} \tag{35}$$

$$M N V \frac{\mathrm{d}V}{\mathrm{d}R} + \frac{\mathrm{d}}{\mathrm{d}R} N T = 0 \tag{36}$$

$$\frac{G}{4\pi R^2} \frac{\mathrm{d}}{\mathrm{d}R} \left(\frac{\gamma T/M}{\gamma - 1} + \frac{V^2}{2} \right) = N A, \tag{37}$$

where N, V, and T are the density, velocity, and temperature, respectively. The flow is adiabatic, i.e. no radiation, and the boundary conditions that we use at the pellet surface imply that the pellet is cryogenic. We make the change of variables to $W = V^2$ and Mach number, $\mu \equiv \gamma T / M V^2$, to obtain

$$N = \frac{G/M}{4\pi R^2 \sqrt{W}} \tag{38}$$

$$(\mu^2 - 1) \frac{\mathrm{d}W}{\mathrm{d}R} = \frac{4W}{R} \left[1 - \frac{(\gamma - 1) R \mu^2 A}{2 M W^{3/2}} \right] \tag{39}$$

$$(\mu^2 - 1) \frac{\mathrm{d}\mu}{\mathrm{d}R} = \frac{\mu(\gamma\mu^2 + 1)}{R} \left[1 - \frac{(\gamma - 1) R \mu^2 A}{2 M W^{3/2}} \right] - \frac{\mu(\mu^2 - 1)}{R} \tag{40}$$

Apparently, W and μ suffer the same type of singularity when the Mach number is equal to unity. However, the profiles must remain continuous throughout the sonic transition. To avoid the singularity, we require that

$$W_* = \left(\frac{\gamma - 1}{2} \frac{R_* A_*}{M} \right)^{2/3} \tag{41}$$

We obtain the derivatives at $R = R_*$ by applying l'Hospital's rule to Eq. (39)-(40), viz.

$$W_*' = \frac{2W_*}{R_*} \frac{3 - \gamma}{1 + \gamma} \left[1 + \sqrt{1 + \frac{2(1 + \gamma)}{(3 - \gamma)^2} \left(1 - \frac{R_* A_*'}{A_*} \right)} \right] \tag{42}$$

$$\mu_*' = \frac{1 - \gamma}{2R_*} \left[1 + \sqrt{1 - \frac{2(1 + \gamma)}{(1 - \gamma)^2} \left(\frac{\gamma - 5}{\gamma + 1} + \frac{R_* A_*'}{A_*} \right)} \right] \tag{43}$$

where primes denote differentiation with respect to R, and starred quantities denote values at the sonic point. The ODEs are integrated from the sonic point. For a fixed value of R_*, the profiles are uniquely determined by two parameters: G, A_*. Profiles are sought out for which the following boundary conditions are satisfied:

$$\xi(R \to \infty) = 0, \tag{44}$$

$$W(R_p) = \mu(R_p) = 0 \tag{45}$$

The point at which W and μ simultaneously vanish is the pellet surface, and thus, R_p is the pellet radius.

The kinetic heating models of Sec. III were plugged into Eq. (38)-(40) and solved via the shooting method outlined above. As a result, we obtain the function $G(R_p)$. These results are plotted in Fig. 2 then fitted to a function of the form $G \propto R_p^{4/3}$, where G has units of g/s and R_p has units of cm. The ablation rate therein is in good agreement with the scaling law Eq. (7). For the numerical results presented, the pellet material is neon ($Z = 10$), and hence, the cloud particles are monatomic ($\gamma = 5/3$); the background plasma has density $n_\infty = 10^{14}\,cm^{-3}$ and temperature $T_\infty = 2\,keV$. When A is given by the slab model, $G = 358.1\,R_p^{4/3}$, while the spherical model yields $G = 339.6\,R_p^{4/3}$ which amounts to about 5 percent difference in the coefficient; either result is consistent with Eq. (7) to within a factor of order unity. The comparison between the results using the slab and spherical heat models suggests that the perturbative procedure discussed in Sec. III C may be unnecessary for calculating the ablation rate.

Scaling laws of the form Eq. (7) are commonly used in fluid models because their "universality" allows investigation of pellets of varying composition and sizes without expensive kinetic calculations. For impurity pellets, the power-law scaling of Ref. [1] [see Eq. (20) of the reference but also reproduced below with cgs units],

$$G = 4.26 \times 10^7\,(\gamma - 1)^{0.28} M^{0.72} \times \varepsilon^{-0.16} \times R_p^{1.44} \times \frac{n_\infty^{0.45} T_\infty^{1.72}}{Z^{0.56}} \tag{46}$$

is commonly employed. This power-law scaling (which also features a relatively small dependence on the heat of evaporation, ε in eV) minimizes the deviation of the ablation rate obtained by the scaling versus those obtained by gas-dynamic simulations performed by the authors of Ref. [1]. The powers appearing in Eq. (20) of Ref. [1], in addition to the coefficient, are determined by this fitting procedure. For neon in a plasma with $n_\infty = 10^{14}\,cm^{-3}$

and $T_\infty = 2\,keV$, their model yields an ablation rate $G = 1205.5 R_p^{1.44}$ which is significantly higher than ours. Although the gas-dynamic model of Ref. [1] (see also Ref. [15]) accounts for electrostatic shielding and non-uniformity in the ablation flow, which are missing in this paper's model, these mechanisms actually reduce the ablation rate. This suggests that impurity pellets may penetrate deeper into the tokamak than implied by the ablation rate model of Ref. [1]. Independent analysis from Ref. [16] (shown in Fig. 2) is in general agreement with our results. The analysis of Ref. [16] differs from our own in that the investigators use the kinetic heating model of Ref. [7] which excludes elastic scattering of hot electrons. The most obvious reason for the disagreement with Eq. (20) of Ref. [1] is the reduction in the ablation rate caused by the diffusive nature of the electron heating. The authors of Ref. [1] include ion heating of the pellet, but this effect is small. Another possible reason for the disagreement is that among the pellet materials used for their statistical fittings, neon was not among them. A reason for this exclusion may be because ablation data for neon did not exist at the time. In fact, at the time of this writing, experimental measurements of neon ablation is still lacking.

V. SUMMARY

A kinetic approach has been developed to describe the electron heating of high-Z impurity material in a magnetic field. We include the effect of elastic scattering, and as a result, hot electrons diffuse through the ablation cloud. When we account for the fact that hot electrons penetrate a distance $\delta_p \sim \lambda/\sqrt{Z}$ (where λ is the mean-free-path of the hot electrons), then we obtain the scaling law Eq. (7) which has $G \sim Z^{-7/6}$ as opposed to $Z^{-2/3}$ which appears in Ref. [1]. When the gyro-frequency is much larger than the elastic scattering frequency, the hot electrons diffuse along the field lines, but in the opposite regime, the diffusion occurs radially with respect to the pellet center. In the latter case, the ablation is uniform across the pellet surface, and we have calculated the ablation rate and have shown that they are in good agreement with the $R_p^{4/3}$ scaling of Eq. (7). We have also compared against Eq. (20) of Ref. [1] but have found that their model predicts a much higher ablation rate. The authors of Ref. [1] include electrostatic shielding and non-uniform heating of the pellet surface, but these mechanisms reduce the ablation rate. This suggests that the random-walk nature of the

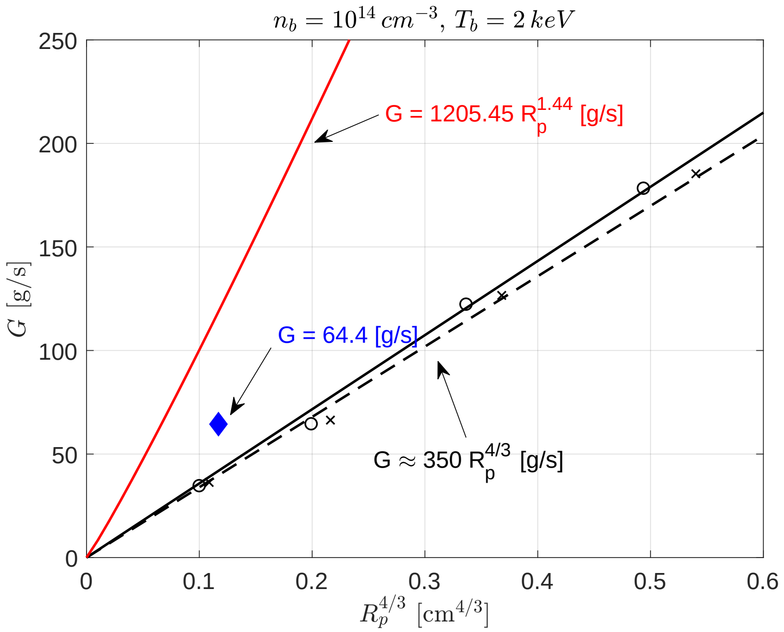

FIG. 2. Neon ablation rate versus pellet radius to the four-thirds power. The ablation model of Ref. [2] is implemented with heat deposition described by Eq. (27) [shown in x's and dashed] and Eq. (33) [shown in o's and solid]. These results are in good agreement with the pellet radius scaling of Eq. (7) and the slope indicates the undetermined constant of proportionality in the scaling law. Independent analysis from Ref. [16] using the heat deposition of Ref. [7] yields $G = 64.4\,g/s$ for a $2\,mm$ Neon pellet and is indicated by the blue $\diamond$ marker. The ablation rate calculated from the model of Ref. [1] is shown in red. The background plasma density and temperature are $n_\infty = 10^{14}\,cm^{-3}$ and $T_\infty = 2\,keV$, respectively.

hot electrons imposed by elastic scattering may play a significant role in reducing the heating afforded to the pellet surface, and consequently, the ablation rate. This is also reflected in larger power of Z that appears in Eq. (7). It is important to note that our fluid model assumes the sublimation energy of the impurity material is low and ignores radiative losses. The kinetic heat deposition model is general to all impurity materials of high-Z, but the ablation model that we use only pertains to cryogenic pellets. A future work which combines the heating model of this paper with a more robust gas-dynamic model (à la Ref. [8, 9]) should be carried out to address the impact of the missing physics. In addition, comparisons should be made to experiment as measurements of more cryogenic pellets become available to test the $Z^{-7/6}$ scaling.

VI. ACKNOWLEDGEMENT

We we would like to thank R. Samulyak and P.B. Parks, as well as, D. Hu for helpful discussion. This work was supported by the U.S. Department of Energy Contract Nos. DEFG02-04ER54742 and DE-SC0016283.

VII. APPENDIX

A. Calculation of moments of distribution function

In this section we perform a cursory calculation of the moments, $\langle\cos\theta\, f\rangle$, $\langle\sin\theta\cos\psi\, f\rangle$, and $\langle\sin\theta\sin\psi\, f\rangle$ which appear in Eq. (10). The brackets denote the angular average $\langle g\rangle \equiv (1/4\pi)\int_0^{2\pi}\int_0^{\pi} g\sin\theta\,\mathrm{d}\theta\,\mathrm{d}\psi$. The first moment involving $\cos\theta$ is obtained by multiplying Eq. (9) by $\cos\theta$ and taking the angular average, viz.

$$\begin{aligned}\frac{\partial}{\partial z}v\langle\cos^2\theta\, F\rangle + \frac{1}{\rho}\frac{\partial}{\partial\rho}\rho\left[v\cos\varphi\langle\sin\theta\cos\theta\cos\psi\, F\rangle + v\sin\varphi\langle\sin\theta\cos\theta\sin\psi\, F\rangle\right]\ldots\\ +\frac{1}{\rho}\frac{\partial}{\partial\varphi}\left[v\sin\varphi\langle\sin\theta\cos\theta\cos\psi\, F\rangle - v\cos\varphi\langle\sin\theta\cos\theta\sin\psi\, F\rangle\right] - \frac{1}{v^2}\frac{\partial}{\partial v}v^3\nu\,\langle\cos\theta\, F\rangle\\ = \frac{\nu_s}{2}\langle\frac{\cos\theta}{\sin\theta}\frac{\partial}{\partial\theta}\sin\theta\frac{\partial f}{\partial\theta}\rangle + \frac{\nu_s}{2}\langle\frac{\cos\theta}{\sin^2\theta}\frac{\partial^2 f}{\partial\psi^2}\rangle\end{aligned} \tag{47}$$

For high-Z, the RHS dominates and therefore, f is nearly isotropic. This allows us to approximate f by its isotropic part, F, on the LHS. The LHS is evaluated by taking F outside the brackets and taking advantage of the even-ness (with respect to θ) of the integrands; only the first term on the LHS is even. The RHS is simplified using integration-by-parts. The final result is

$$\frac{\partial}{\partial z}v\langle\cos^2\theta\rangle\, F = -\nu_s\langle\cos\theta\, f\rangle \Longrightarrow \langle\cos\theta\, f\rangle = -\frac{1}{3\nu_s}\, v\frac{\partial F}{\partial z} \tag{48}$$

The other two convolutions proceed in similar fashion, so we simply state the result:

$$\frac{1}{3}\left[\frac{1}{r}\frac{\partial}{\partial r}r\, v\cos\varphi\, F - \frac{1}{r}\frac{\partial}{\partial\varphi}v\sin\varphi\, F\right] = -\omega_c\langle\sin\theta\sin\psi\, f\rangle - \nu_s\langle\sin\theta\cos\psi\, f\rangle \tag{49}$$

$$\frac{1}{3}\left[\frac{1}{r}\frac{\partial}{\partial r}r\, v\sin\varphi\, F + \frac{1}{r}\frac{\partial}{\partial\varphi}v\cos\varphi\, F\right] = +\omega_c\langle\sin\theta\cos\psi\, f\rangle - \nu_s\langle\sin\theta\sin\psi\, f\rangle \tag{50}$$

We add/subtract these two last results to/from each other to obtain

$$\langle\sin\theta\cos\psi\, f\rangle = +\frac{1/3}{\omega_c^2+\nu_s^2}\left[\omega_c\left(v\sin\varphi\frac{\partial F}{\partial\rho} + \frac{v\cos\varphi}{\rho}\frac{\partial F}{\partial\varphi}\right) - \nu_s\left(v\cos\varphi\frac{\partial F}{\partial\rho} - \frac{v\sin\varphi}{\rho}\frac{\partial F}{\partial\varphi}\right)\right] \tag{51}$$

$$\langle\sin\theta\sin\psi\, f\rangle = -\frac{1/3}{\omega_c^2+\nu_s^2}\left[\omega_c\left(v\cos\varphi\frac{\partial F}{\partial\rho} - \frac{v\sin\varphi}{\rho}\frac{\partial F}{\partial\varphi}\right) + \nu_s\left(v\sin\varphi\frac{\partial F}{\partial\rho} + \frac{v\cos\varphi}{\rho}\frac{\partial F}{\partial\varphi}\right)\right] \tag{52}$$

B. Estimate of electrostatic sheath potential

We consider the scenario where a surface of pellet material is in contact with a hot background plasma. Although the background plasma consists of both electrons and ions, it is primarily the electrons that heat the pellet surface. The electron particle flux to the pellet surface precipitates the formation of an electrostatic potential that tries to re-establish ambipolarity, i.e. zero net current, and quasi-neutrality, i.e. zero net charge. In contrast to the sheath model of Ref. [17] which balances the electron current with an ion current, we consider a return current of cold electrons pulled from the surface of the pellet by the electrostatic potential, which implies that the surface is emissive. Another distinction (which is due to our emphasis on high-Z) is a backscattered component of the backwards flux in addition to the component reflected back by the electrostatic barrier. The backscattered component ultimately lowers the electrostatic barrier, as we will see.

For simplicity, we consider one dimension. The equation describing the potential Φ is

$$\Phi'' = -4\pi|e|\left(n_0 - \frac{n_0^+}{2}e^{|e|\Phi/T_0} - \frac{n_0^-}{2}e^{|e|\Phi/T_0} - \frac{|j|}{\sqrt{2|e|(\Phi-\Phi_s)/m}}\right) \tag{53}$$

where n_0 is the background density, T_0 is the background temperature, $\Phi_s < 0$ is the potential at the pellet surface, j is the back-current of cold electrons, and the " $+$ " superscript denotes the density of hot electrons incident on the surface, while " $-$ " denotes the density of hot electrons which are turned away (due to either reflection by the electrostatic potential barrier or backscattering). The primes denote differentiation with respect to position. In the absence of backscattering, the back-current must balance nearly the entirety of the forward-going incident electron flux; thus, $|j| \sim nev_{th}$ and $|e|\Phi \sim T_0$ in the scatter-less case. Conversely, in the strong-scattering regime (i.e. high-Z), the particle flux indicated in Eq. (14) would require a reduced back-current of $|j| \sim nev_{th}/\sqrt{Z}$, and the corresponding potential is $|e|\Phi \ll T_0$.

Accordingly, we expand Eq. (53) in the limit $|e|\Phi/T_0 \ll 1$ to obtain

$$\Psi'' = -\left[1 - \left(\frac{n_0^+ + n_0^-}{2n_0}\right)(1+\Psi) - \frac{|\alpha|}{\sqrt{\Psi-\Psi_s}}\right] \approx \Psi - \epsilon + \frac{|\alpha|}{\sqrt{\Psi-\Psi_s}} \tag{54}$$

which consists of the non-dimensional quantities,

$$\Psi \equiv \frac{|e|\Phi}{T_0}, \quad |\alpha| \equiv \frac{|j|/n_0}{\sqrt{2T_0/m}} \tag{55}$$

and units of length normalized by the Debye length, $(4\pi e^2 n_0/T_0)^{-1/2}$. The approximation in Eq. (54) comes about since $\epsilon \equiv 1-(n_0^+ + n_0^-)/2n_0 \ll 1$. The quantity ϵ represents the small imbalance between the forward and backward incident particle fluxes and is determined by the condition that $\Psi'' = 0$ when $\Psi = 0$; hence, $\epsilon = |\alpha|/\sqrt{|\Psi_s|}$.

We integrate Eq. (54) with the condition that the electric field is zero far away, i.e. $\Psi' = 0$ when $\Psi = |\Psi_s|$:

$$\frac{(\Psi')^2}{2} = \frac{\Psi^2}{2} - \frac{\Psi_s^2}{2} - \frac{|\alpha|}{\sqrt{|\Psi_s|}}(\Psi - \Psi_s) + 2|\alpha|\sqrt{\Psi - \Psi_s} \tag{56}$$

The condition that the electric field is zero far away tells us that

$$\frac{\Psi_s^2}{2} = |\alpha|\sqrt{|\Psi_s|} \Longrightarrow \Psi_s \propto \alpha^{2/3} \tag{57}$$

Recall that that the cold electron current scales as $|j| \sim n_0 e v_{th}/\sqrt{Z}$ in the high-Z case, which tells us that the sheath potential scales as

$$\Psi_s \sim Z^{-1/3} \tag{58}$$

---

[1] Sergeev, V. Yu. *et al* 2006 *Plasma Phys. Reports* **32** 5

[2] Parks, P. B. and Turnbull, R. J. (1978) *Phys. Fluids* **21** 1735

[3] Shiraki, D. *et al* 2016 *PoP* **23** 062516

[4] Bethe, H. 1932 *Zeitschrift f'ur Physik* **76** 293

[5] MacAulay, A. K. 1994 *Nucl. Fusion* **34** 43

[6] Kuteev, B. V. *et al* 1984 *Sov. J. Plasma Phys.* **10** 675

[7] Ishizaki, R. *et al* 2004 *Phys. Plasmas* **11** 8

[8] Lengyel, L.L. *et al* 1999 *Nucl. Fusion* **39** 791

[9] Morozov, D.Kh. *et al* 2004 *Nucl. Fusion* **44** 252

[10] Trubnikov, B. A. 1965 *Reviews of Plasma Physics* **1** 105

[11] Parks, P. B. *et al* 1988 *Nucl. Fusion* **28** 477

[12] Mott, N. F. and Massey, H. S. W. 1965 *Theory of Atomic Collisions, 3rd Ed.* , Oxford Univ. Press

[13] Chapman, S. and Cowling, T. G. 1952 *The Mathematical Theory of Non-Uniform Gases, 2nd Ed.* , Cambridge, London

[14] Kuteev, B. V. and Tsendin, L. D. 2001 *Res. Report No. NIFS-717*, National Inst. for Fusion Science, Nagoya

[15] Kuteev, B. V. and Sergeev, V. Yu. 1995 *Nucl. Fusion* **35** 10

[16] Samulyak, R. , Parks, P. B. Private correspondence.

[17] Lengyel, L.L. *et al* 1996 *Nucl. Fusion* **36** 1679

Bibliography

[1] BP. Bp statistical review of world energy. Technical report, BP, 2018.

[2] N.A. Krall and A.W. Trivelpiece. *Principles of plasma physics.* McGraw-Hill, New York, 1932.

[3] M.N. Rosenbluth and S.V. Putvinski. Theory for avalanche of runaway electrons in tokamaks. *Nucl. Fusion*, 37(1355), 1997.

[4] P.C. de Vries, M.F. Johnson, B. Alper, P. Buratti, T.C. Hender, H.R. Koslowski, V. Riccardo, and JET-EFDA Contributors. Survey of disruption causes at jet. *Nucl. Fusion*, 51(5), 2011.

[5] R.S. Cohen, L. Spitzer Jr., and P. McR. Routly. The electrical conductivity of an ionized gas. *Phys. Rev.*, 80(2):230–238, 1950.

[6] A.H. Boozer. Theory of tokamak disruptions. *Phys. Plasmas*, 19(058101), 2012.

[7] C. Rea and R.S. Granetz. Exploratory machine learning studies for disruption prediction using large databases on diii-d. *Fusion Sci. and Tech*, 74:89–100, 2018.

[8] A.H. Boozer. Runaway electrons and iter. *Nucl. Fusion*, 57(056018), 2017.

[9] D. Shiraki, N. Commaux, L.R. Baylor, N.W. Eidietis, E.M. Hollmann, C.J. Lasnier, and R.A. Moyer. Thermal quench mitigation and current quench control by injection of mixed species shattered pellets in diii-d. *Phys. Plasmas*, 23(062516), 2016.

[10] M. Lehnen, K. Aleynikova, P.B. Aleynikov, D.J. Campbell, P. Drewelow, N.W. Eidietis, Yu. Gasparyan, R.S. Granetz, Y.Gribov, N.Hartmann, E.M. Hollmann, V.A.Izzo, S.Jachmich, S.-H.Kim, M. Kocan, H.R. Koslowski, D. Kovalenko, U. Kruezi, and P.C. de Vries. Disruptions in iter and strategies for their control and mitigation. *J. Nucl. Mater.*, 463:39–48, 2015.

[11] A. Gurevich, G. Milikh, and R. Roussel-Dupre. Nonuniform runaway air-breakdown. *Phys. Letters A*, 187(197), 1994.

[12] G.D. Holman. Acceleration of runaway electron and joule heating in solar flares. *Astrophysical J.*, 293(584), 1985.

[13] C.T.R. Wilson. The acceleration of β-particles in strong electric fields such as those of thunderclouds. *Math. Proceedings of the Cambridge Society*, 22(04):534, 1925.

[14] P. Helander and D.J. Sigmar. *Collisional transport in magnetized plasmas.* Cambridge University Press, 2002.

[15] B.N. Breizman, P. Aleynikov, E.M. Hollmann, and M. Lehnen. Physics of runaway electrons in tokamaks. Accepted to Nucl. Fusion, 2019.

[16] B.A. Trubnikov. Particle interactions in fully ionized plasma. *Rev. of Plasma Phys.*, 1:105, 1965.

[17] J. Connor and R. Hastie. Relativistic limitations on runaway electrons. *Nucl. Fusion*, 15(415), 1975.

[18] H. Dreicer. Electron and ion runaway in a full ionized gas. *Phys. Rev.*, 115(2):238, 1959.

[19] G.A. Schott. *Electromagnetic radiation.* Cambridge University Press, 1912.

[20] J. Schwinger. On the classical radiation of accelerated electrons. *Phys. Rev*, 75(1912), 1949.

[21] J.H. Yu, E.M. Hollmann, N. Commaux, N.W. Eidietis, D.A. Humphreys, A.N. James, T.C. Jernigan, and R.A. Moyer. Visible imaging and spectroscopy of disruption runaway electrons in diii-d. *Phys. Plasmas*, 20(20):042113, 2013.

[22] G. Bekefi. *Radiation processes in plasmas.* Wiley and Sons, 1966.

[23] I.M. Pankratov. Analysis of the synchrotron radiation spectra of runaway electrons. *Plasma Phys. Reports*, 25(145), 1999.

[24] A.V. Gurevich. On the theory of runaway electrons. *Sov. Phys. JETP*, 12(5), 1961.

[25] M.D. Kruskal and I.B. Bernstein. Runaway electrons in an ideal lorentz plasma. *Phys. of Fluids*, 7(3):407, 1964.

[26] R.H. Cohen. Runaway electrons in an impure plasma. *Phys. of Fluids*, 19(2):239, 1976.

[27] P. Helander, H. Smith, T. Fulop, and L.-G. Eriksson. Electron kinetics in a cooling plasma. *Phys. Plasms*, 11(12):5704, 2004.

[28] P. Aleynikov and B.N. Breizman. Generation of runaway electrons during the thermal quench in tokamaks. *Nucl. Fusion*, 57(4):046009, 2017.

[29] J.R. Martin-Solis, A. Loarte, and M. Lehnen. Formation and termination of runaway beams in iter disruptions. *Nucl. Fusion*, 57(6):066025, 2017.

[30] J.R. Martin-Solis, A. Loarte, and M. Lehnen. On the avalanche generation of runaway electrons during tokamak disruptions. *Phys. Plasmas*, 22(8):082503, 2015.

[31] B.N. Breizman. Marginal stability model for the decay of runaway electron current. *Nucl. Fusion*, 54(7):072002, 2014.

[32] J.R. Martin-Solis, R. Sanchez, and B. Esposito. Experimental observation of increased threshold electric field for runaway generation due to synchrotron radiation losses in the ftu tokamak. *Phys. Rev. Lett.*, 105(185002), 2010.

[33] P. Aleynikkov and B.N. Breizman. Theory of two threshold fields for relativistic runaway electrons. *Phys. Rev. Lett.*, 114(155001), 2015.

[34] J.R. Martin-Solis, J.D. Alvarez, R. Sanchez, and B. Esposito. Momentum-space structure of relativistic runaway electrons. *Phys. Plasmas*, 5(6):2370, 1998.

[35] A.K. Fontanilla and B.N. Breizman. Lifetime and universal distribution of seed runaway electrons. *Phys. Plasmas*, 24(112509), 2017.

[36] Z. Guo, X.-Z. Tang, and C.J. McDevitt. Models of primary runaway electron distribution in the runaway vortex regime. *Phys. Plasmas*, 24(11):112508, 2017.

[37] F. Andersson, P. Helander, and L.-G. Eriksson. Damping of relativistic electron beams by synchrotron radiation. *Phys. Plasmas*, 8(12):5221, 2001.

[38] L. Spitzer Jr., D.J. Grove, W.E. Johnson, L. Tonks, and W.R. Westendorp. Problems of the stellerator as a useful power source. Technical report, USAEC, 1954.

[39] J.L. Terry, E.S. Marmar, J.A. Snipes, D. Garnier, TFTR Group, and V.Yu. Sergeev. Imaging of lithium pellet ablation trails and measurement of q profiles in tftr. *Rev. Scientific Instruments*, 63(5191), 1992.

[40] L.R. Baylor, P.B. Parks, T.C. Jernigan, J.B. Caughman, S.K. Combs, C.R. Foust, W.A. Houlberg, S. Maruyama, and D.A. Rasmussen. Pellet

fuelling and control of burning plasmas in iter. *Nucl. Fusion*, 47(5):443, 2007.

[41] L.L. Lengyel, K. Buchla, G. Pautasso, L. Ledl, A.A. Ushakov, S. Kalvin, and G. Veres. Modelling of impurity pellet ablation in asdex upgrade (neon) and wendelstein w7-as (carbon) by means of a radiative (killer) pellet code. *Nucl. Fusion*, 39(6):791, 1999.

[42] L.R. Baylor, S.J. Meitner, T.E. Gebhart, J.B.O. Caughman, J.L. Herfindal, D. Shiraki, and D.L. Youchison. Shattered pellet injection technology design and characterization for disruption mitigation experiments. *Nucl. Fusion*, 59:066008, 2019.

[43] P.B. Parks, J.S. Leffler, and R.K. Fisher. Analysis of low z impurity pellet ablation for fusion diagnostic studies. *Nucl. Fusion*, 28(3), 1988.

[44] N.F. Mott and H.S.V. Massey. *Theory of atomic collisions.* Oxford University, 1965.

[45] B.V. Kuteev and L.D. Tsendin. Analytical model of neutral gas shielding for hydrogen pellet ablation. Technical report, NIFS, 2001.

[46] A.K. MacAulay. Geometrical, kinetic and atomic physics effects in a two dimensional time dependent fluid simulation of ablating fuel pellets. *Nucl. Fusion*, 34(1):43, 1994.

[47] A.K. Fontanilla and B.N. Breizman. Heating and ablation of high-z pellets in high-temperature plasmas. In submission to Nucl. Fusion, 2019.

[48] S.L. Milora and C.A. Foster. A revised neutral gas shielding model for pellet-plasma interactions. *IEEE Transactions on Plasma Science*, PS-6(4), 1978.

[49] R. Ishizaki, P.B. Parks, N. Nakajima, and M. Okamoto. Two-dimensional simulation of pellet ablation with atomic processes. *Phys. Plasmas*, 11(8):4064, 2004.

[50] V.Yu. Sergeev, O.A. Bakhareva, B.V. Kuteev, and M. Tendler. Studies of the impurity pellet ablation in the high-temperature plasma of magnetic confinement devices. *Plasma Phys. Reports*, 32(5), 2006.

[51] H. Bethe. Bremsformel fur elektronen relativistischer geschwindigkeit. *Zeitschrift fur Physik*, 76(5-6):293–299, 1932.

[52] H. Smith, P. Helander, L.-G. Eriksson, and T. Fulop. Runaway electron generation in a cooling plasma. *Phys. Plasmas*, 12(122505), 2005.

[53] P.B. Parks and R.J. Turnbull. Effect of transonic flow in the ablation cloud on the lifetime of a solid pellet in a plasma. *Phys. Fluids*, 21(10):1735, 1978.

[54] O. Embreus, A. Stahl, and T. Fulop. On the relativistic large-angle electron collision operator for runaway avalanches in plasmas. *J. Plasma Phys.*, 84(1), 2018.

[55] H. Bethe. Zur theorie des durchgangs schneller korpuskularstrahlen durch materie. *Annalen der Physik*, 397(3):325–400, 1930.

[56] Chr. Moller. Zur theorie des durchgangs schneller elektronen durch materie. *Annalen der Physik*, 406(5):531–585, 1932.

[57] B. Pegourie. Pellet injection experiments and modelling. *Plasma Phys. Control. Fusion*, 49:R87–R160, 2007.

[58] B.V. Kuteev, V.Yu. Sergeev, and S. Sudo. Emergency discharge quench or rampdown by a noble gas pellet. *Nucl. Fusion*, 35(10):1167, 1995.

[59] B.V. Kuteev, V.Yu. Sergeev, and L.D. Tsendin. Interaction of carbon pellets with a hot plasma. *Sov. J. Plasma Phys*, 10(6):675, 1984.

[60] H.J.C Oliver, S.E. Sharapov, B.N. Breizman, A.K. Fontanilla, D.A. Spong, D. Terranova, and JET contributors. Modification of the alfven wave spectrum by pellet injection. In submission to Nucl. Fusion, 2019.

[61] L.D. Landau and E.M. Lifshitz. *Course of Theoretical Physics, Volume 6, Second Edition: Fluid Mechanics*. Butterworth-Heinemann, 1987.

Vita

Adrian Kristopher Fontanilla was born in Hayward, CA as the son of Luis D. Fontanilla and Nenita Fontanilla. He received his Bachelor's of Science degree in physics with a specialization in materials from UC San Diego in 2008. He immediately began work as an analyst with Applied Operations Research, Inc. in Solana Beach and specialized in underwater acoustic models. This is where he encountered the mantis shrimp and became interested in fusion. He applied for graduate school and entered studies at the University of Texas at Austin in 2012.

Permanent address: fontanilla.adrian@gmail.com

This dissertation was typeset with LaTeX[†] by the author.

[†] LaTeX is a document preparation system developed by Leslie Lamport as a special version of Donald Knuth's TeX Program.